NASA TECHNICAL MEMORANDUM

NASA TM X-62,122

NASA TM X-62,122

PITOT–PRESSURE DISTRIBUTIONS OF THE FLOW FIELD OF A DELTA–WING ORBITER

Joseph W. Cleary

Ames Research Center
Moffett Field, Ca. 94035

May 1972

15 p8

PITOT-PRESSURE DISTRIBUTIONS OF THE FLOW FIELD OF A DELTA-WING ORBITER

by

Joseph W. Cleary

ABSTRACT

Pitot-pressure distributions of the flow field of a 0.0075-scale model of a typical delta-wing shuttle orbiter are presented. Results are given for the windward and leeward sides on centerline in the angle-of-attack plane from wind-tunnel tests conducted in air. Distributions are shown for three axial stations X/L = .35, .60, and .98 and for angles of attack from 0° to 60°. The tests were made at a Mach number of 7.4 and for Reynolds numbers based on body length from 1.5×10^6 to 9.0×10^6. The windward distributions at the two survey stations forward of the body boattail demonstrate the essentially compressive aspects of the flow from the shock wave to the body. Conversely, the distributions at the aft station display an expansion of the flow that is attributed to body boattail. On the lee side, results are given at low angles of attack that illustrate the complicating aspects of the canopy on the flow field while at high angles of attack, results are given to show the effects of flow separation.

PITOT-PRESSURE DISTRIBUTIONS OF THE FLOW FIELD OF A DELTA-WING ORBITER

by

Joseph W. Cleary

INTRODUCTION

Reusable space-shuttle vehicles that can terminate an earth orbital mission with a conventional airplane-type landing are currently evolving as a device for transporting personnel and supplies to and from earth orbit. The performance of these vehicles is dependent in part on reliable estimates of heating during the high angle-of-attack entry phase of the trajectory. An analysis of heating for the entry mode requires information on the shock-wave shape and shock-layer structure in order that an accurate estimate of flow conditions at the edge of the boundary layer can be made. Moreover, information on the flow field can be helpful as a guide in the selection of the size and disposition of the various components of the vehicle such as the canopy, wing, tail, and control surfaces.

Considerable information on the flow field can be gained from shadowgraphs and visualization of the surface flow and these results are presented in references 1 and 2 respectively. In addition, pitot-pressure surveys of the flow field can give useful information on flow-field processes and the complexities that arise; e.g., from imbedded waves, vortices and flow separation. The present experimental effort endeavors, by means of pitot-pressure surveys, to investigate the more significant aspects of the windward and leeward flow fields in the angle of attack plane of a typical delta-wing orbiter. An investigation was conducted of the effects of varying three fundamental parameters: (1) flow-field axial position, (2) angle of attack, and (3) Reynolds number.

Tests were made of a 0.0075-scale model of a blended delta-wing-body orbiter proposed by North American Rockwell Corporation for the high cross-range mission. This vehicle has a wing with 60° sweepback of the leading edge and 7° dihedral and is designated the 134 full-scale orbiter. The vehicle has a centerline vertical tail but the present tests were conducted without the tail. Stability and control characteristics of this configuration are given in references 3 and 4. Measurements of heating of a similar configuration are presented in reference 5 and summarized in reference 6. The present pitot-pressure data include the preliminary results given in reference 7 and are presented herein in more complete form.

The tests were made in air at a Mach number of 7.4 and for Reynolds numbers based on body length from 1.5×10^6 to 9.0×10^6. Results are given for angles of attack from 0° to 60°.

NOTATION

The symbols and coefficients used in presenting the test results are defined as follows:

B	a parameter (eq. (A2))
C_p	static-pressure coefficient, $\left[\frac{p}{p_\infty} - 1\right] \frac{2}{\gamma M_\infty^2}$
C_{p_p}	pitot-pressure coefficient, $\left[\frac{p_p}{p_\infty} - 1\right] \frac{2}{\gamma M_\infty^2}$
L	body length
M	Mach number
p	pressure
Re	Reynolds number
$\bar{r}$, σ	coordinates of a conical field
V	velocity
X, Z	body rectangular coordinates
$\bar{X}$, $\bar{Z}$	rectangular coordinates of a conical field
α	angle of attack
γ	ratio of specific heats
δ	wedge angle
θ	angular coordinate measured from the free-stream direction
ω	flow angle measured from the free-stream direction

Subscripts

2	value behind an oblique shock wave
3	value behind a second shock wave of the same family
p	pitot
s	surface
∞	free-stream
L	body length

TESTS AND EQUIPMENT

Model

A three-view sketch, photographs of the model, and other information pertinent to the test are presented in figure 1. Dimensional details of the model are given in Table I. The model was fabricated from a brass casting. The mold for the cast was formed from the 0.00763-scale model used in the investigation of reference 3. Because of shrinkage of the cooled casting and finishing and polishing of the model, the final dimensions of the model were about 1.5-percent less than those of the original model and yielded a model scale of 0.0075. The model was supported by a one-inch diameter dummy balance housed within the model with its axis parallel to the reference axis.

Facility and Tests

The investigation was conducted in air in the Ames 3.5-foot hypersonic wind tunnel. The tests were made at a Mach number of 7.38 and for free-stream Reynolds number based on body length from 1.5×10^6 to 9.0×10^6. The total temperature of the reservoir was maintained within the range from about 1200°R to 1300°R.

The model was mounted on the quick-insert support strut which enters the tunnel after flow is established and withdraws at the completion of the data measurements. This strut can pivot through angles of attack from 0° to 20° in the horizontal plane. The angle-of-attack range of the strut was increased to 65° by using brackets between the model and the sting with incidence angles of 15°, 30°, and 45°. The model was mounted with the wing vertical and was pitched in the horizontal plane of the tunnel. The tests were conducted at angles of attack from 0° to 60°.

The model was instrumented with flow-field pitot-pressure rakes mounted on the centerline of the windward and leeward surfaces as depicted in figure 1(b). These rakes were mounted with the probes at X/L = .35, .60, and .98. With the probes at X/L = .98, the rakes were attached to a platform behind the model that was fastened to the model support bracket. With the probes at the two forward stations X/L = .35 and .60, the rakes were attached directly to the model. The innermost probe of both rakes was flush with the model surface except with the lee-side rake at X/L = .98. For this case the innermost probe was in line with an extension of the upper surface of the model as can be seen in figure 1(b).

The axes of the probes were parallel to the model reference axis which is parallel to upper and lower surfaces of the body over about the mid semi-length of the body. A body-axis system of coordinates is used to define the probe positions. The Z coordinate is measured from the model surface normal to the reference axis of the model with the exception that with the lee-side rake at X/L = .98, Z is measured from an extension of the straight lee-side surface of the body.

The probes were formed from stainless steel tubing with an inside diameter of 0.042 inches and an outside diameter of .062 inches. The probes were spaced 4 diameters (0.25 inch) and 2 diameters (.125 inch) apart on the leeward and windward rakes respectively.

Since the tests were conducted for a wide range of angles of attack, the inclination of the local flow to the probes may exceed a practical limit for which pitot probes can give accurate results. Reference 8 asserts that pitot probes of the type used in the present investigation can give accurate results for inclination angles up to about 20°. In the present investigation, the measurements of probes outside the flow field and exposed to the free stream afford an estimate of the effects of flow inclination on accuracy of the probe measurements. This estimate is shown in figure 2 and it can be seen that the probes are in fact accurate (within 4 percent) for flow inclinations up to 20°. Moreover, for $\alpha = 30°$ the measurements are accurate within about 9 percent.

Figure 2 gives a comparison of the experimental calibration with the prediction of swept-cylinder theory. This prediction gives the normalized pressure on the stagnation line of a swept cylinder analogous to successive probes that are adjacent; i.e., the oblique wave is normal to the probe axes. It is apparent from figure 2 that since the experimental values are greater than sweep theory, the probe wave is more normal than that for a swept cylinder and this is evidence that the probe spacing is adequate to give interference-free measurements.

RESULTS AND DISCUSSION

Characteristics of the Bow Shock Wave

Knowledge of the oblique angles of the bow wave and of the shock-wave stand-off distances at the three axial stations of the flow-field surveys can be helpful to an analysis of the pitot-pressure measurements. Although the pitot-pressure probes of the rakes were closely spaced, the separation distance between probes was sufficiently large, particularly for the lee-side rake, to preclude an accurate evaluation of the bow shock-wave position from

the flow-field surveys. Therefore, shock-wave angles and stand-off distances were evaluated in the angle of attack plane from side-view shadowgraphs of the shock-wave patterns that are given in reference 1 for this same model and test conditions. Shock-wave angles of the bow wave in the angle-of-attack plane of the model are presented in figure 3 and stand-off distances from the surface to the wave are presented in figure 4. These results are given for the highest Reynolds number at which the present test results were conducted; i.e., at $Re_{\infty_L} = 9x10^6$ for $0° \leq \alpha < 30°$ and at $Re_{\infty_L} = 6x10^6$ for $30° < \alpha \leq 60°$. Results given in figures 3 and 4 are assumed to apply over the Reynolds number range from $1.5x10^6$ to $9.0x10^6$ of the present test results. The close agreement between shock-wave shapes given in reference 1 for Reynolds numbers of $3.0x10^6$ and $9.0x10^6$ at an angle of attack of 15° attest to this as a reasonably good assumption (see also reference 7).

In addition to bow-wave characteristics, the characteristics of oblique-shock waves, in general, for the test conditions are helpful in analyzing the pitot-pressure measurements. These characteristics are given in figure 5. Since later it will be shown that interference from waves of the same family is encountered on the lee side at low angles of attack, the characteristics of two intersecting oblique waves are presented and shown schematically in figure 5(b) to illustrate salient features of the phenomenon (see reference 9).

Windward Pitot-Pressure Distributions

Pitot-pressure distributions of the windward flow field are presented in figure 6 at $X/L = .35$. In like manner, results are given in figures 7 and 8 at $X/L = .60$ and in figures 9 to 12 at $X/L = .98$. The ordinate Z/L of figures 6 to 12 is measured downward from the surface of the model and normal to the model reference axis. In order to detect the viscous layer, if possible, the innermost probe was placed adjacent to the model surface and data are plotted at the value of Z/L for the probe centerlines. The location of the bow wave is indicated by a hatched line that was estimated from figure 4(b); values of pitot-pressure coefficient at the wave (denoted by solid symbols) were estimated from wave angles given in figure 3(b) utilizing shock-wave characteristics of figure 5(a). In general, the location of the bow wave from shadowgraphs and the predicted value of pitot pressure at the wave from oblique-shock-wave theory agree well with results from the probe measurements. Exceptions occur in the data for $\alpha = 55°$ and 60° at $X/L = .60$ (see figures 7(b) and 8(b)). Here the poor agreement of probe measurements with oblique-wave theory is believed due to interference from the projection of the highly inclined rake strut outside the bow wave. With the strut within the bow wave, as was the case for surveys at $X/L = .98$, the results appear free of interference at these same high angles of attack

(see figures 9(b) and 11(b)). It is believed that at $X/L = .60$ ($\alpha = 55°$ and 60°) the data adjacent to the body $0 < Z/L \lesssim .02$, at least are free of interference. While at high angles of attack the probes were highly inclined to the free-stream flow, the misalinement of the probes to the local flow is not as large because of the flow deflection immediately behind the wave. For example for $\alpha = 60°$, the flow deflection behind the wave for all three survey stations (from figures 3(b) and 5(a)) was about 42° or 43° and therefore, the probe misalinement was about 16° or 17°. The error from this misalinement is believed to be about 4 percent.

At low angles of attack, the defect of pitot pressure measured by the probe adjacent to the surface is attributed to viscous effects of the boundary layer and, in addition perhaps, to the entropy layer due to body bluntness. Relative thicknesses of these two layers were not detected from present test results. Such details require extensive surveys using a larger model with smaller probes. At high angles of attack $\alpha \gtrsim 30°$, it is evident that the viscous and entropy layers were thin relative to even the probe diameter since a substantial defect of pitot pressure was not detected by the surface probe.

In general, the effects of Reynolds number on the pitot-pressure distributions at $X/L = .35$ and .60 are small for the Reynolds number range from 1.5×10^6 to 6.0×10^6. However, at $X/L = .60$ there is a decrease in the level of the distributions for $\alpha > 30°$ for a Reynolds number of 6.0×10^6. Moreover, this decrease is apparent also at $X/L = .98$. Reasons for this decrease in level are not clearly known. However, measurements of heating (reference 6) indicate transition of the boundary layer occurs at $X/L \sim .5$ for the higher Reynolds number; in addition, shadowgraphs of the flow field at this same Reynolds number (references 1 and 2) depict weak waves in the flow field emanating from what appears to be a turbulent boundary layer. These waves, if sufficiently strong could result in a decrease of the pitot pressure.

At $X/L = .98$, pitot-pressure distributions of figure 9(a) indicate that for $\alpha = 0°$ and to a lesser extent for $\alpha = 5°$ there is a thick low energy layer adjacent to the body. While this low energy layer may result from a combination of factors, it is believed to be fundamentally a viscous phenomenon since results given in figures 9(a) to 12(a) show that it is Reynolds number dependent. For $\alpha = 0°$, surface streamlines depicted in reference 2 indicate that for this cambered body configuration the flow over the nose is from the upper surface to the lower surface. Therefore, there is an accumulation and growth of a viscous layer on the lower surface. In addition, the increase of entropy of the flow passing through the steeper part of the bow wave contributes to the observed reduction of pitot pressure adjacent to the body. This low energy layer is significantly thinned by increasing angle of attack and at high angles of attack it essentially vanishes (see figure 11(b)).

At intermediate angles of attack $15° \leq \alpha \leq 35°$, the flow-field distributions of pitot pressure at the aft station (X/L = .98) appear basically different than those at the forward stations. At this station the pitot pressure, in general, decreases from the wave to the body except near the edge of the viscous layer where a reversal is indicated. Reasons for the reversal are not known; it is surmised to be a three-dimensional flow effect. On the other hand, at the forward stations the pitot pressure generally increases as the body is approached from the wave. This type of distribution is believed indicative of a compressive flow process for which the local Mach number decreases at the surface. Conversely, the distributions at X/L = .98 are believed characteristic of an expansion process due to the boattail for which Mach number increases. At high angles of attack, the effects of boattailing are less significant and the distributions display similarities to those at X/L = .6.

Composites of the wave pattern and pitot-pressure distributions.- To more clearly illustrate the significant features of the windward flow field, a superposition of the pitot-pressure distributions on the wave pattern is presented in figure 13. Wave patterns are from shadowgraphs depicted in references 1 and 2. In addition, inviscid streamlines from a conical flow approximation of the flow field given in Appendix A are shown to illustrate the essentially compressive aspect of the flow at the forward and middle survey stations. These streamlines are terminated at about the initial Mach wave from the expansion at the boattail. Results are shown for $0° < \alpha < 60°$ in increments of 15°.

Figure 13(a) displays more clearly the aforementioned thick viscous layer observed at the aft station for $\alpha = 0°$. A straight-line extension of the lower surface of the model to X/L = .98 demonstrates that this viscous layer extends well beyond the shielded region of the boattail. It is apparent that a control or perhaps a ventral fin placed here and adjacent to the surface would have low effectiveness at low angles of attack. However, at higher angles of attack $\alpha > 15°$ the viscous layer is thin and a control should be effective (see figures 13(b) to (e)). For $15° < \alpha < 60°$, the shock layer is comparatively thin on the windward side and moreover, at the forward stations the streamlines approach closely to the body within some fraction of the body length. These streamlines pass through an oblique, essentially straight, segment of the bow wave.

An interesting feature of the flow-field at X/L = .98 is the uninfluential effect of the wing-root wave on the centerline pitot-pressure distributions for $\alpha = 0°$ and 15° (see figure 13(a) and (b)). In the absence of discontinuities in the distributions at where the wave crosses the Z/L axis, the leading-edge waves of the wing panels are not continuous over the body but truncate at an off-center lateral station. This result supports an observation that the leading-edge is discrete as was suggested initially in reference 1 from observations of shadowgraphs.

Comparisons with theory.- Figure 13 depicts that on the windward side for $\alpha \geq 15°$ the shock wave is essentially straight aft of the nose. In a sense the flow approaches being locally conical and surface properties and the distribution of flow-field properties could be estimated by conical flow theory. As an approximation, the virtual apex of the conical flow field is located at the intersection of local tangents to the body and the shock wave. Using this artifice, an estimate can be made of the distributions of pitot pressure at angle of attack by the conical-flow method given in reference 10.

Before comparing this method with the experimental pitot-pressure distributions, it is expedient to compare the static-pressure ratio from the wave to the body with theory in order to differentiate at what axial stations, theory may apply. This comparison is made in figure 14 together with a comparison with swept-cylinder-flow theory. Pressures at the surface given in figure 15 are from faired values of unpublished data by C. Pappas (see reference 6) obtained in the same facility as the present investigation. Static pressures at the wave were estimated by oblique-shock theory from shock angles given in figure 3(b). Figure 14 demonstrates that at $X/L = .35$ and .60 the experimental pressure ratios agree fairly well with predictions of conical- and swept-cylinder-flow theories and the flow is, indeed, compressive from the shock to the body. At $X/L = .98$, the experimental results indicate that the flow expands from the shock to the body and therefore, theory is not shown.

Since the flow is not compressive at $X/L = .98$, a comparison of pitot-pressure distribution with theory is limited to results for $X/L = .35$ and .60. This comparison is given in figure 16 wherein experiment and inviscid conical-flow and swept-cylinder-flow theories are shown normalized by values at the wave. Except for viscous effects adjacent to the surface, good agreement, in general, is indicated between the experimental distributions and inviscid theory. The comparisons of figure 16 indicate that the entropy of the flow at the edge of the viscous layer is effectively that for an oblique wave. While at low angles of attack, better agreement is shown with conical-flow theory, at high angles of attack $\alpha \geq 40°$ there are only small differences between both theories and either appears adequate. At high angles of attack $\alpha \geq 50°$, the comparatively poor agreement between experiment and theories is believed due to the aforementioned interference of the probe strut.

An experimental evaluation of surface Mach number is compared with theory in figure 17. Experemental values were estimated by the Rayleigh pitot equation using measured surface pressures from figure 15 and pito-pressure distributions from figures 6 to 12. At $X/L = .35$ and .60 (figures 17(a) and 17(b) respectively), experiment is compared again with conical-flow and swept-cylinder-flow theories. Also for comparative purposes, an estimate based on normal shock entropy and measured surface pressure is shown. At $X/L = .98$ (figure 17(c)), comparison is made with a Prandtl-Meyer expansion of the flow from the experimental value of surface Mach number estimated at $X/L = .60$. Figures 17(a) and (b)

demonstrate that at the two forward stations, the surface Mach number is predicted reasonably close by either conical-flow or swept-cylinder flow theories. At X/L = .98, figure 17(c) shows that a Prandtl-Meyer expansion underpredicts Mach number although agreement with experiment improves with increasing angle of attack. This underprediction may result from a three-dimensional expansion of the flow that is not accounted for by the two-dimensional theory.

Leeward Pitot-Pressure Distributions

The effects of angle of attack on the lee-side pitot-pressure distributions for X/L = .35, .60, and .98 are presented in figures 18, 19 and 20, and 21 to 24 respectively. Results are given for angles of attack up to 60° even though at large angles of attack the inclination of the local flow to the probes may have been sufficient to incur inaccuracy in the data. For this case, the probes in general, are shielded by the body and submerged within separated flow and even though the results may be inaccurate, they can aid in delineating the extent of the separated flow. In addition to the foregoing pitot-pressure measurements, composites of the shock-wave pattern and the lee-side pitot-pressure distributions are depicted in figure 25 for $0° < \alpha < 60°$ in increments of 15°. Results given in figures 18 to 25 present, in more complete form, the preliminary results presented in reference 7 for the lee-side flow field.

In like manner to results given for the windward side, the position of the bow wave is shown in figures 18 to 24 as a hatched line. The wave position was evaluated from shadowgraphs (reference 1) and values of the wave position are from faired data given in figure 4(a). In addition, values of pitot pressure at the wave were estimated by oblique-shock-wave theory from wave angles given in figure 3(a) and are designated by solid symbols. Although the approximate wave position detected by the probes conformed with shadowgraph measurements of wave position, the values of pitot pressure at the wave (from an extrapolation of experiment) are, in general, overestimated by theory (see figures 18 to 24). Reasons for this overestimate are not clear, but may be due, in part, to inaccuracies in wave angle measurements since the theoretical estimate is sensitive to wave angle because the lee-side wave angles are small (see figure 5(a)).

The extent to which the probes are shielded first by the canopy and then by the body nose with increasing angle of attack are shown by horizontal lines with appropriate symbols to designate angle of attack. It is an interesting feature of the flow that as the probes became shielded by the nose with increasing angle of attack, a reversal develops in the pitot-pressure distribution adjacent to the essentially separated flow (see figure 18).

Moreover, there appears to be correlation between the position of this reversal and the extent of the shielded region. Reasons for this phenomenom are not clearly understood; it may be a manifestation of body vortices that form aft of the nose and in a sense is a three-dimensional flow phenomenom.

Figures 19 and 20 indicate a similar correlation between reversals in the distributions and body-nose shielding at X/L = .60. However, increasing Reynolds number appears to have a more substantial effect on the reversals here than at X/L = .35. In contrast to results given at X/L = .35, figures 19 and 20 indicate the flow is separated at X/L = .60 for an angle of attack of 15°. Likewise at the aft station X/L = .98, the flow separates at a lower angle of attack. Moreover, increasing the Reynolds number from 1.5×10^6 to 9.0×10^6 significantly reduces the thickness of the separated flow at X/L = .98 for $\alpha \lesssim 20°$. Since for these lower angles of attack the vertical tail would be immersed in a highly nonuniform flow that is Reynolds number dependent, the contribution of the tail to directional stability may be affected by Reynolds number.

At the lower angles of attack $\alpha \lesssim 10°$ the canopy wave dominates the lee-side flow and is therefore, considered the outer bound of the flow field at the three survey stations. For this condition the bow wave intersects and merges with the canopy wave. Since these two waves are of the same family, a contact-surface discontinuity is believed to be formed by the intersecting waves in a manner similar to that for plane waves (reference 9). This is shown schematically in figure 5(b). This contact surface is visible as a faint discontinuity in shadowgraphs of references 1 and 2 for an angle of attack of 0° and is depicted in figure 25(a) imbedded within the wave pattern. Furthermore, it is identified in figures 21 to 24 as an abrupt change in pitot pressure in the unseparated flow region of the flow field. For $\alpha = 0°$ the contact surface intersects the vertical tail at about one third of the semispan (see figure 21(a)). With increasing angle of attack, it intersects the vertical tail nearer the tip and for an angle of attack of 10° it is above the tip. At higher angles of attack the canopy wave becomes imbedded beneath the bow wave and the contact surface discontinuity vanishes since the waves no longer intersect.

CONCLUDING REMARKS

Pitot-pressure distributions of the flow field of a 0.0075-scale model of a delta-wing orbiter are presented for a Mach number of 7.4. Results are given for the windward and leeward sides of the flow field in the angle of attack plane of the model for angles of attack from 0° to 60°. Distributions are presented at three axial stations X/L = .35, .60, and .98 for Reynolds numbers based on body length from 1.5×10^6 to 9.0×10^6. At the

stations forward of the body boattail X/L = .35 and .60, the windward distributions demonstrate that the flow is compressive from the shock wave to the body and the flow field is closely approximated by conical-flow theory. Conversely, at the aft station X/L = .98 the distributions display an expansion of the flow from the wave to the body that is attributed to the body boattail. Here a Prandtl-Meyer expansion over the boattail gives a fair estimate of surface properties of the flow. While detailed effects of Reynolds number variation are noted, in general, the effects of varying Reynolds number for the range from 1.5×10^6 to 9.0×10^6 are small.

On the lee side the pitot-pressure distributions display the complicating aspects of the canopy on the flow field when, for low angles of attack, the canopy is unshielded. It is shown that a contact surface discontinuity arises in the flow field from the intersection of the bow and canopy waves. This discontinuity crosses the tail but with increasing angle of attack, vanishes as the canopy wave becomes imbedded in the flow field of the bow wave. For angles of attack up to about 20° the tail is subjected to a highly nonuniform flow that is Reynolds number dependent. At high angles of attack, the tail would be immersed in separated flow.

APPENDIX A

APPROXIMATION FOR FLOW-FIELD STREAMLINES

An equation is derived for flow-field streamlines in the angle-of-attack plane of conical flows. The results can be applied as an approximation to more general compressive-type flows that have an essentially straight shock wave as may be encountered; e.g., on the windward side of orbiter vehicles. For these cases, as illustrated in sketch (a), the flow is assumed to be locally conical and to have a virtual apex at the intersection of tangents to the body surface and to the wave. The method is based on results given in reference 10 which, although approximate, yield accurate estimates of hypersonic flow-field properties for perfect and real gases in thermodynamic equilibrium.

Sketch (a) depicts the pertinent parameters. From reference 10 the local flow angle $\omega_s - \omega$ is given by equation (A1) where $\sigma = \theta - \omega_s$ is a conical angular coordinate measured from the surface

$$\tan(\omega_s - \omega) = \frac{B \sin \sigma}{1 - B \cos \sigma} \tag{A1}$$

$$B = \frac{\sin (\omega_s - \omega_2)}{\sin (\theta_2 - \omega_2)} \tag{A2}$$

Since

$$\frac{d\bar{Z}}{d\bar{X}} = - \tan (\omega_s - \omega) \tag{A3}$$

and

$$\bar{X} = \bar{r} \cos \sigma \tag{A4}$$

$$\bar{Z} = \bar{r} \sin \sigma \tag{A5}$$

it can be shown that

$$\frac{\bar{r} \cos \sigma \dfrac{d\sigma}{d\bar{r}} + \sin \sigma}{\bar{r} \sin \sigma \dfrac{d\sigma}{d\bar{r}} - \cos \sigma} = = \tan (\omega_s - \omega) \tag{A6}$$

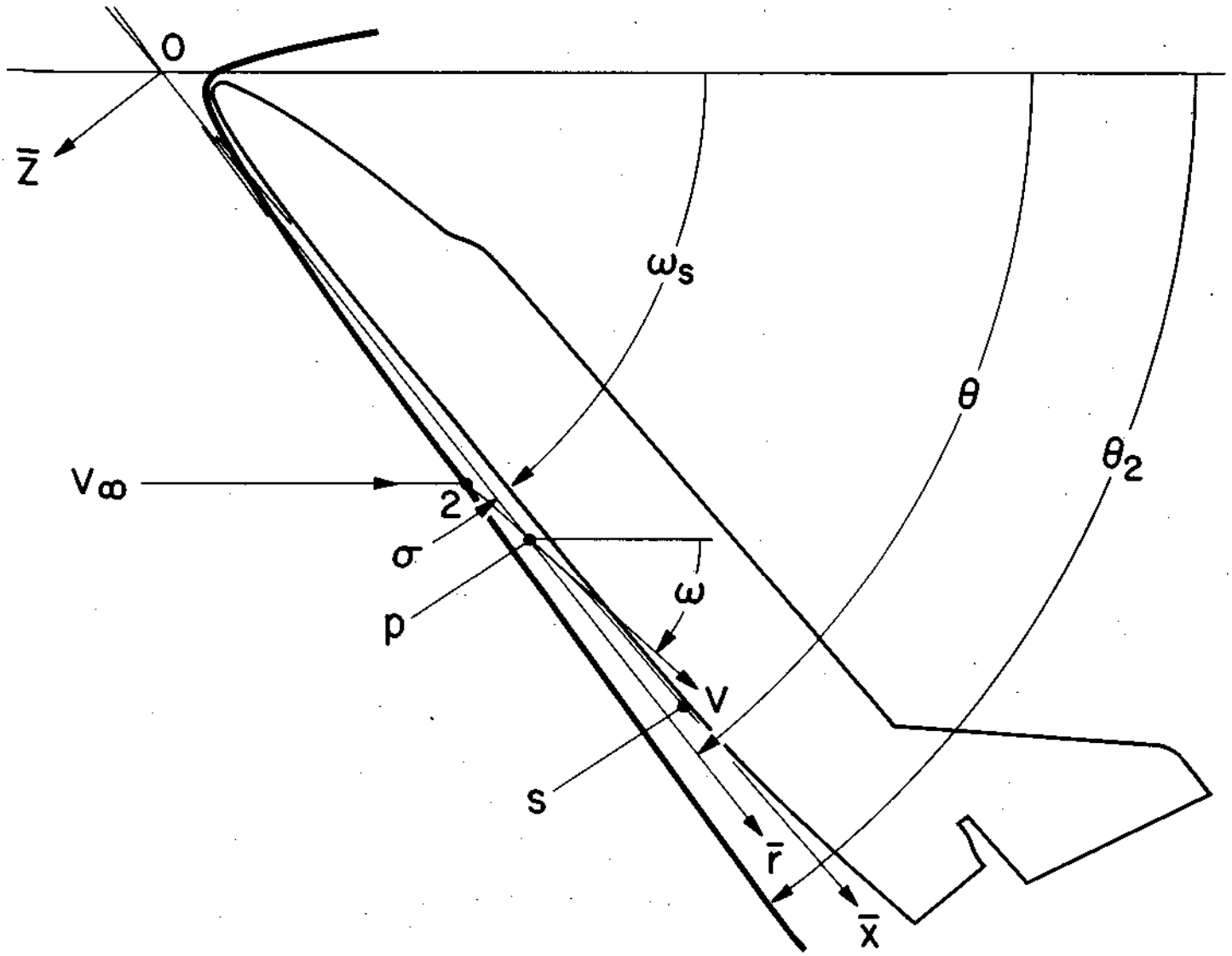
O
$\bar{z}$
ω_s
θ
θ_2
V_∞
2
σ
p
ω
V
s
$\bar{r}$
$\bar{x}$

Sketch (a)

By combining equations (A1) and (A6) and algebraic manipulation, it is apparent that

$$\bar{r}\,[\cos\sigma - B]\,\frac{d\sigma}{d\bar{r}} = -\sin\sigma \tag{A7}$$

Separation of variables yields (A8)

$$\frac{\cos\sigma - B}{\sin\sigma}\,d\sigma = -\frac{d\bar{r}}{\bar{r}} \tag{A8}$$

Integrating (A8) gives (A9)

$$\frac{\bar{r}}{\bar{r}} = \frac{\sin(\theta_2 - \omega_s)}{\sin(\theta - \omega_s)}\left[\frac{1 + \cos(\theta_2 - \omega_s)/1 - \cos(\theta_2 - \omega_s)}{1 + \cos(\theta - \omega_s)/1 - \cos(\theta - \omega_s)}\right]^{B/2} \tag{A9}$$

where the constant of integration was evaluated at the wave $\bar{r} = \bar{r}_2$ and $\sigma = \sigma_2 = \theta_2 - \omega_s$. Equation (A9) gives the radial distance $\bar{r}$ of the streamline from the apex as a function of the conical coordinate $\theta - \omega_s$. Equation (A9) can be simplified to give equation (A10).

$$\frac{\bar{r}}{\bar{r}_2} = \frac{\sin(\theta_2 - \omega_s)}{\sin(\theta - \omega_s)}\left[\frac{\tan\frac{1}{2}(\theta - \omega_s)}{\tan\frac{1}{2}(\theta_2 - \omega_s)}\right]^{B} \tag{A10}$$

REFERENCES

1. Cleary, Joseph W.: Hypersonic Shock-Wave Phenomena of a Delta-Wing Space Shuttle Orbiter. NASA TM X-62,076, October 28, 1971.

2. Cleary, Joseph W.: Experimental Surface Flow Patterns and Flow-Field Phenomena of a Delta-Wing Space-Shuttle Orbiter. NASA TM X-62,113, February 17, 1972.

3. Cleary, Joseph W.: Hypersonic Stability and Control Characteristics of a Delta-Wing Space Shuttle Orbiter. NASA TM X-62,067, December 28, 1970.

4. Malcolm, Gerald N.: Aerodynamic Characteristics of a Space Shuttle Delta-Wing Orbiter at Mach Numbers from 0.25 to 2.0. NASA TM X-62,044, June 1971.

5. Lockman, William K.; and DeRose, Charles E.: Aerodynamic Heating of a Space Shuttle Delta-Wing Orbiter. NASA TM X-62,057, August 11, 1971.

6. Marvin, J. G.; Seegmiller, H. L.; Lockman, W. K.; Mateer, G. G.; Pappas, C. C.; and DeRose, C. E.: Surface Flow Patterns and Aerodynamic Heating on Space Shuttle Vehicles. Paper No. 71-594, AIAA, June 1971.

7. Cleary, Joseph W.: Lee-Side Flow Phenomena on Space Shuttle Configurations at Hypersonic Speeds. Part I: Flow Separation and Flow-Field Viscous Phenomena of a Delta Wing Shuttle Orbiter Configuration. NASA TM X-2507, Vol. 2, February 1972, NASA Aerothermodynamics Technology Conference, Dec. 1971.

8. Liepman, H. W.; and Roshko, A.: Elements of Gasdynamics. GALCIT, Aeronautical Series, John Wiley and Sons, N. Y., 1957.

9. Courant, R.; and Friedrichs, K. O.: Supersonic Flow and Shock Waves. Institute for Mathematics and Mechanics New York University, New York. Interscience Publishers, Inc., New York, 1948.

10. Cleary, Joseph W.: Approximation for Distribution of Flow Properties in the Angle of Attack Plane of Conical Flows. NASA TN D-5951, August 1970.

TABLE I

MODEL DIMENSIONS

Body	
Length, inches	15.9
Maximum width, inches	3.49
Maximum depth, inches	2.04
Fineness ratio	6.18
Maximum cross-sectional area, square inches	5.15
Complete Delta Wing	
Planform area, square inches	49.3
Span, inches	10.7
Aspect ratio	2.31
Rate of taper	1.73
Taper ratio	0.0
Dihedral angle, degrees	7.0
Root incidence angle, degrees	0.0
Aerodynamic twist, degrees	-5.0
Sweep-back angles	
Leading edge, degrees	60.0
Trailing edge, degrees	0.0
0.25 Element line, degrees	52.2
Chords	
Root (wing station 0.0 inches), inches	9.24
Tip, inches	0.0
Mean aerodynamic chord, inches	6.16
Airfoil Section	
Root (wing station 1.80 inches)	NACA 0009-64
Tip (wing station 4.06 inches)	NACA 0012-64
Elevon, One Panel	
Planform area, square inches	4.00
Span, inches	4.07
Inboard chord, inches	1.00
Outboard chord, inches	1.00

TABLE I con't

Sweepback angles	
Leading edge, degrees	0.0
Trailing edge, degrees	0.0
Hingeline, degrees	0.0

Centerline Vertical Tail

Planform area, square inches	5.60
Span, inches	2.90
Aspect ratio	1.48
Rate of taper	0.72
Taper ratio	.31
Sweep-back angles	
Leading edge, degrees	45.0
Trailing edge, degrees	15.8
0.25 Element line, degrees	39.4
Chords	
Root, inches	2.98
Tip, inches	0.91
Mean aerodynamic chord, inches	2.13

Airfoil section: Root and tip sections are 5° semi-vertex blunted wedges with 20° flared edges aft of 0.6 chord.

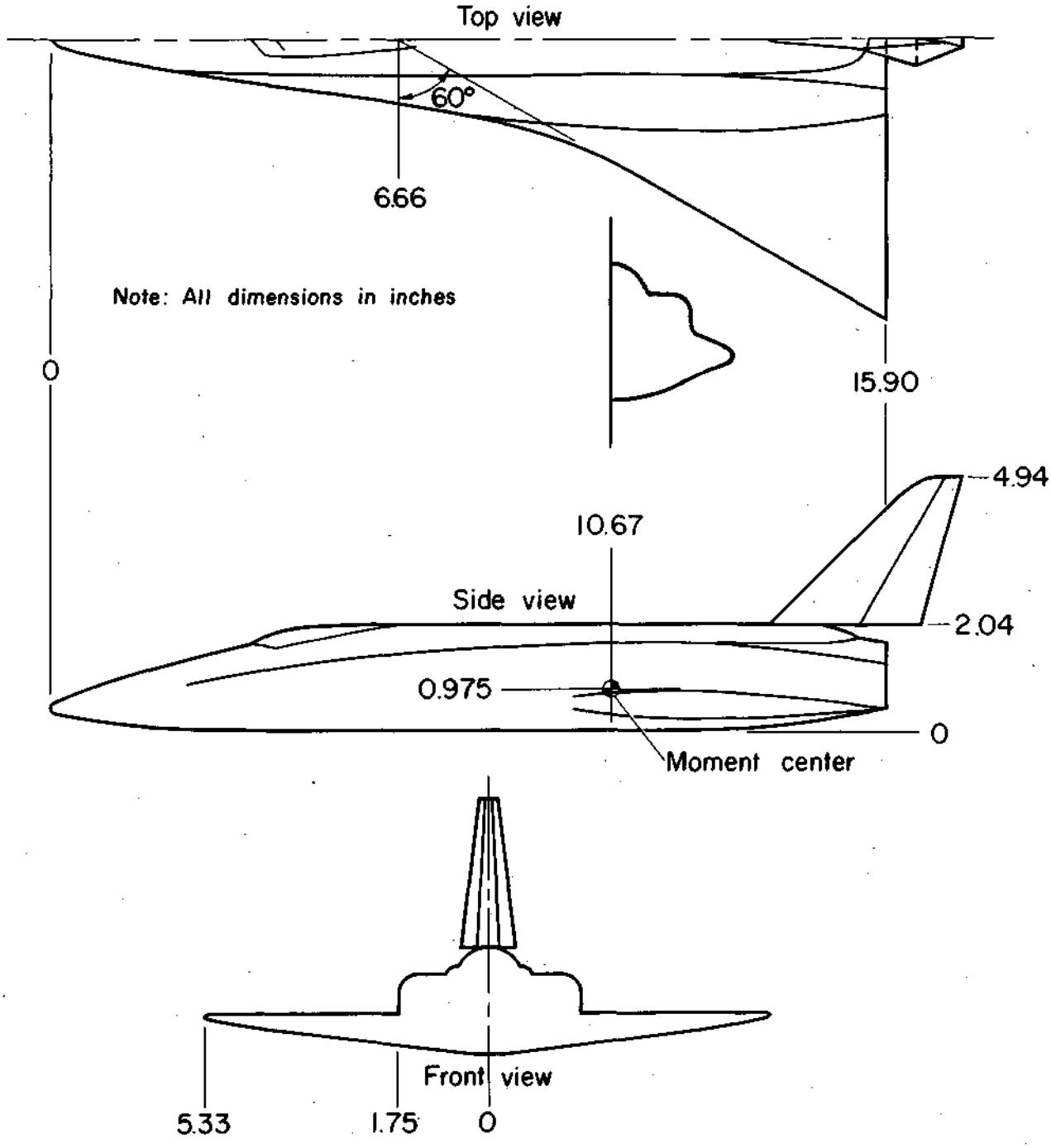

(a) Sketch of the model.

Figure 1.- Model dimensions, photographs and definitions.

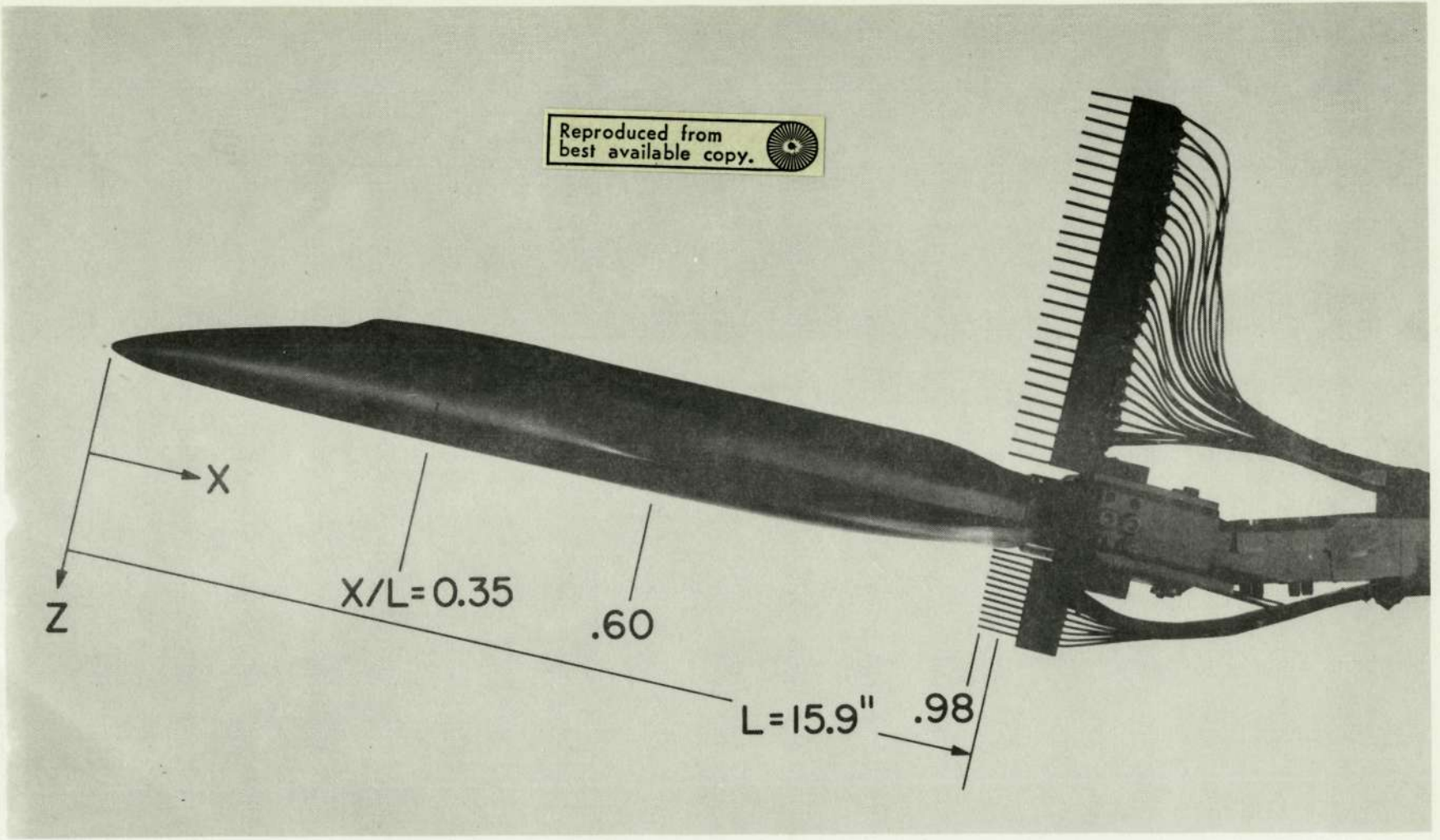

(b) Model instrumented with flow-field rakes.

Figure 1.- Continued.

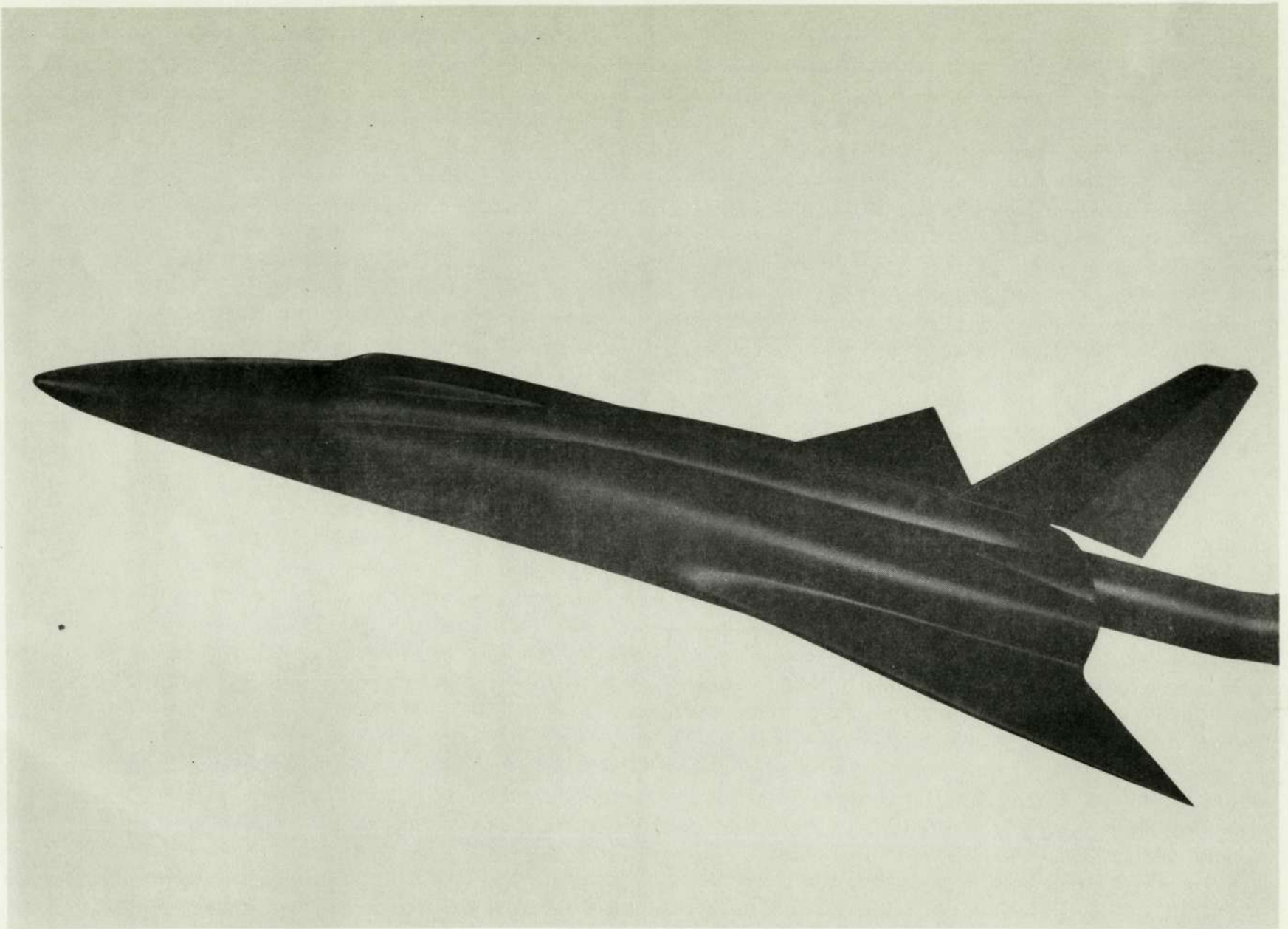

(c) Three-quarter front view of the model.

Figure 1.- Continued.

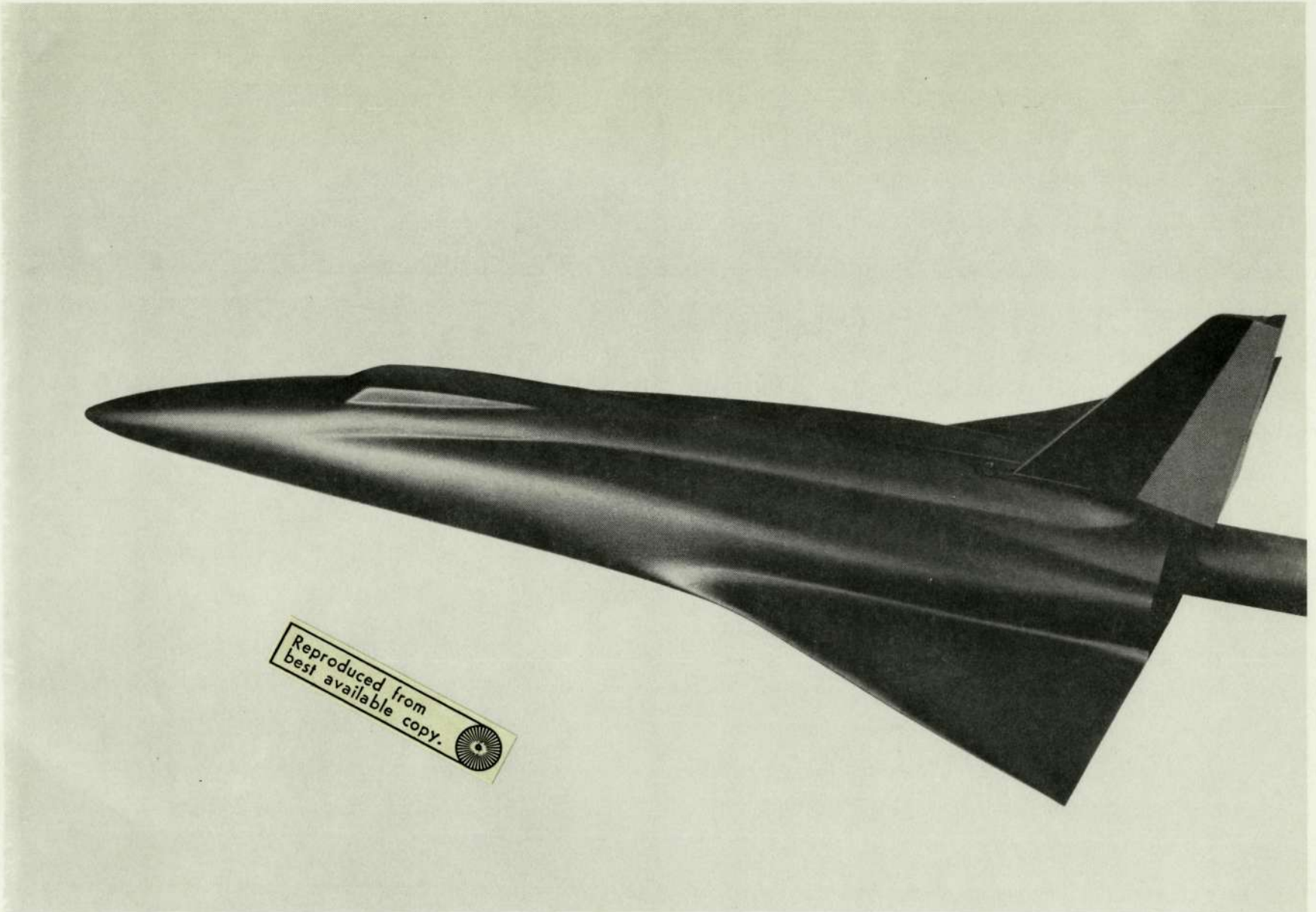

(d) Three-quarter rear view of the model.

Figure 1.- Concluded.

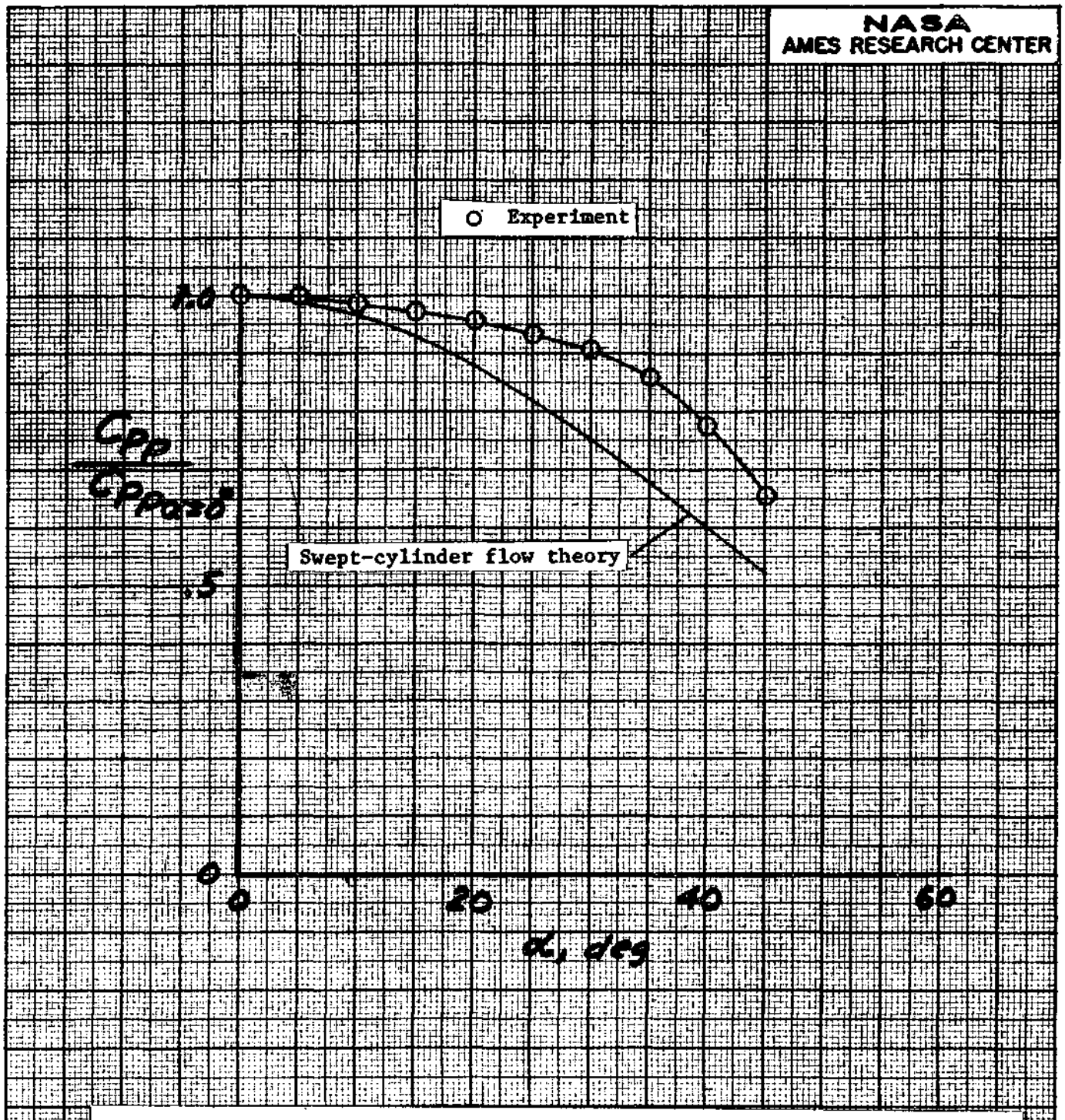

Figure 2.- Calibration of the pitot-pressure probes. $M_\infty = 7.4$.

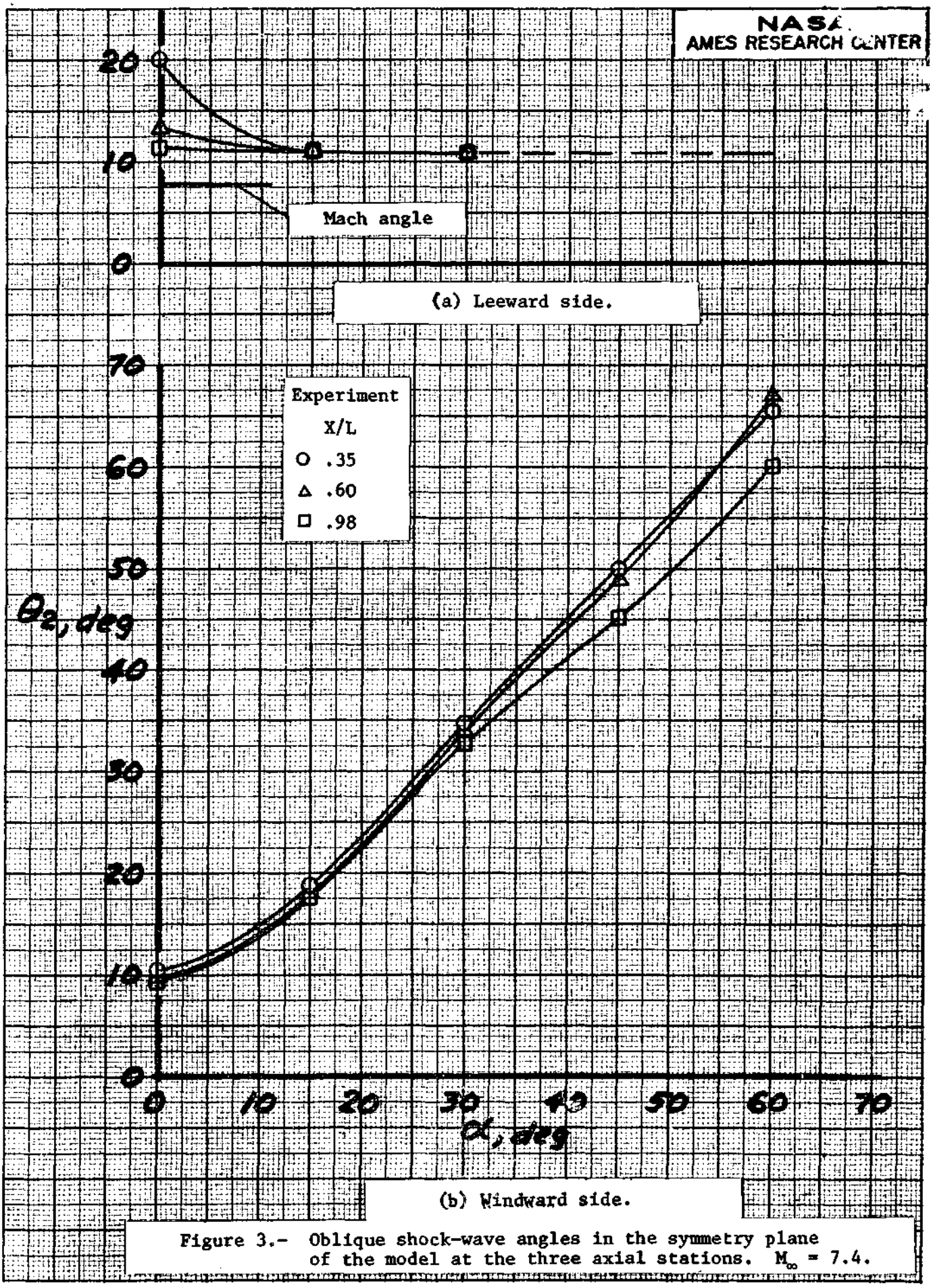

Figure 3.- Oblique shock-wave angles in the symmetry plane of the model at the three axial stations. $M_\infty = 7.4$.

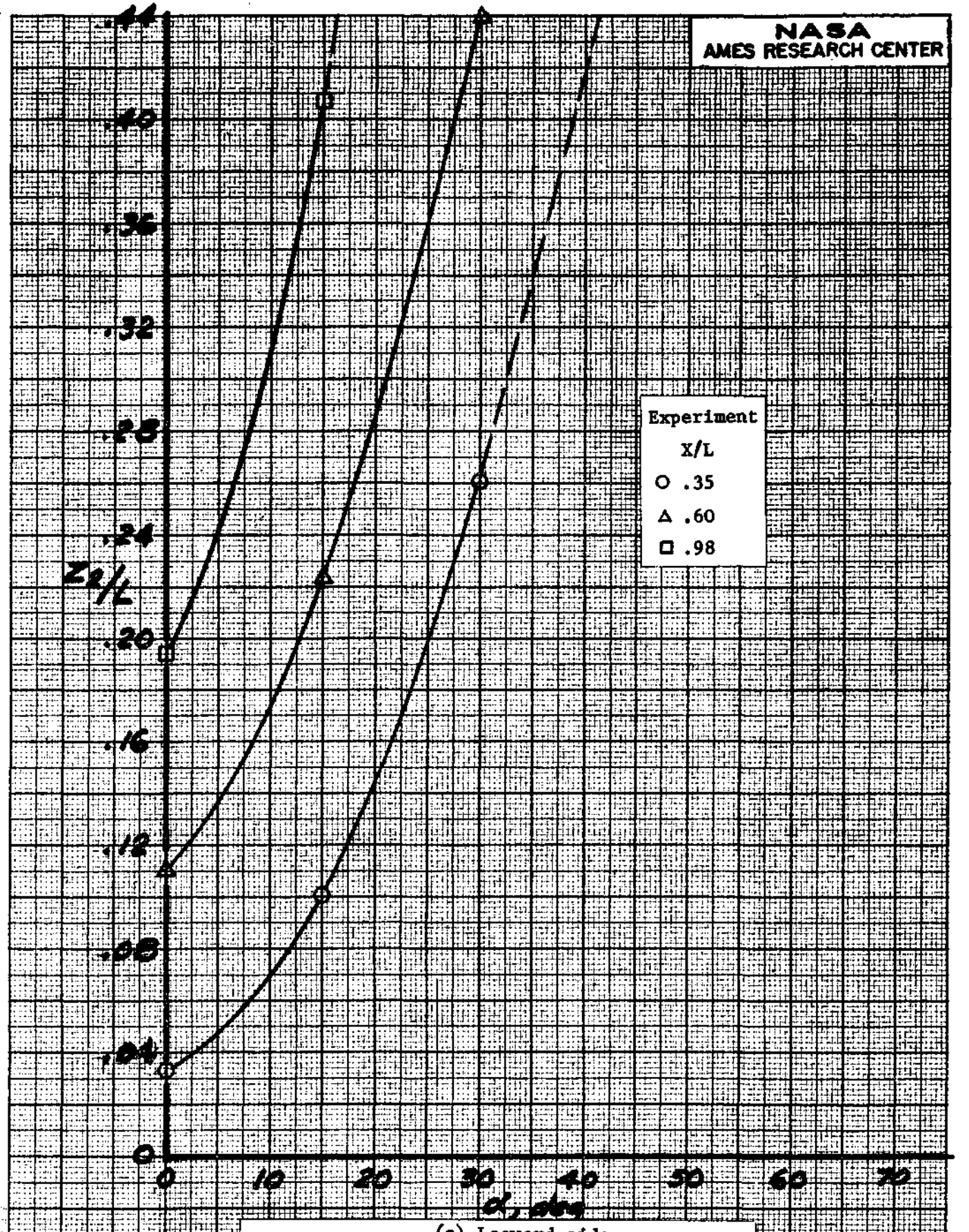

(a) Leeward side.

Figure 4.- Shock-wave stand-off distance in the symmetry plane of the model at the three axial stations. $M_\infty = 7.4$.

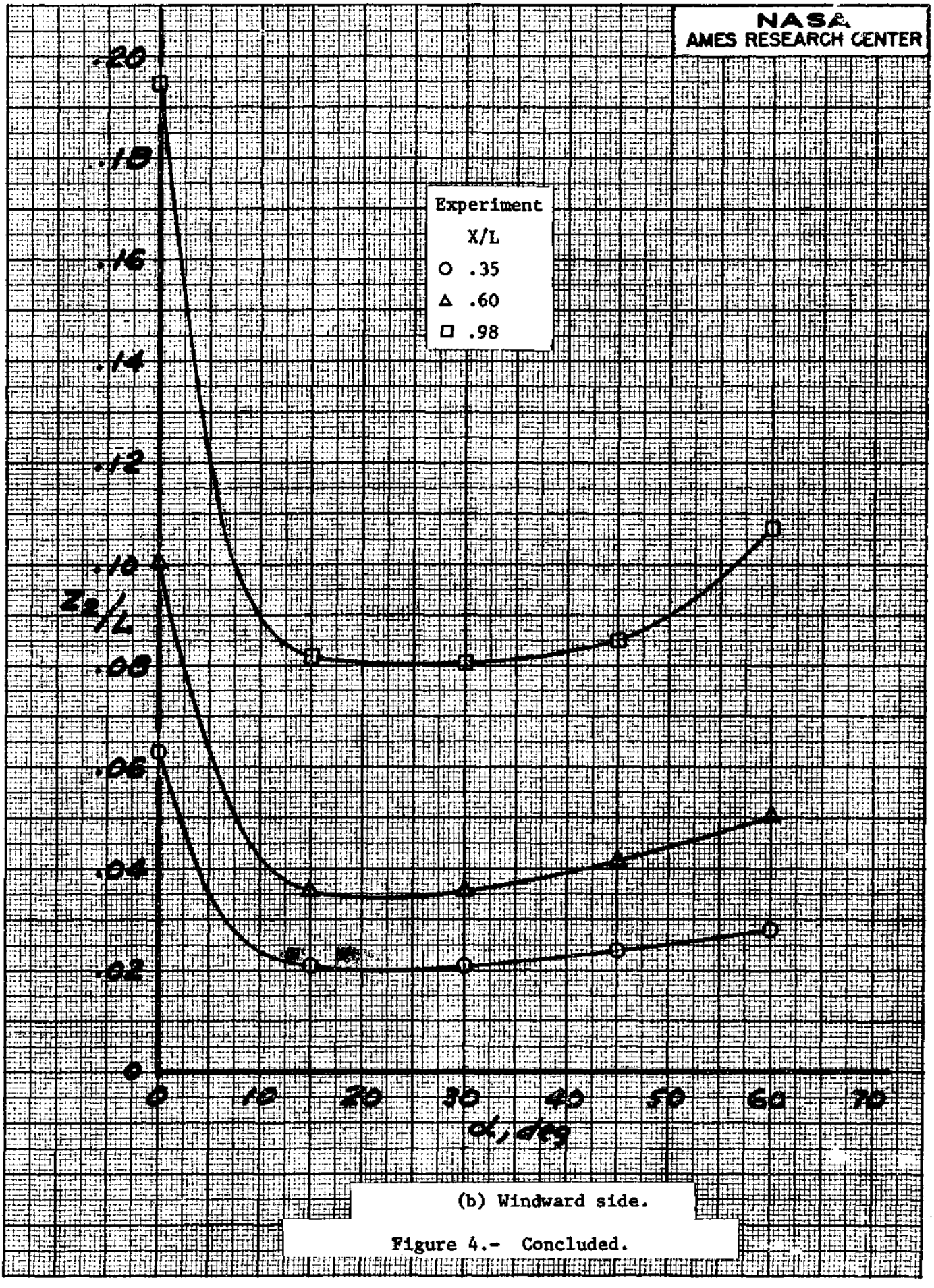

(b) Windward side.

Figure 4.- Concluded.

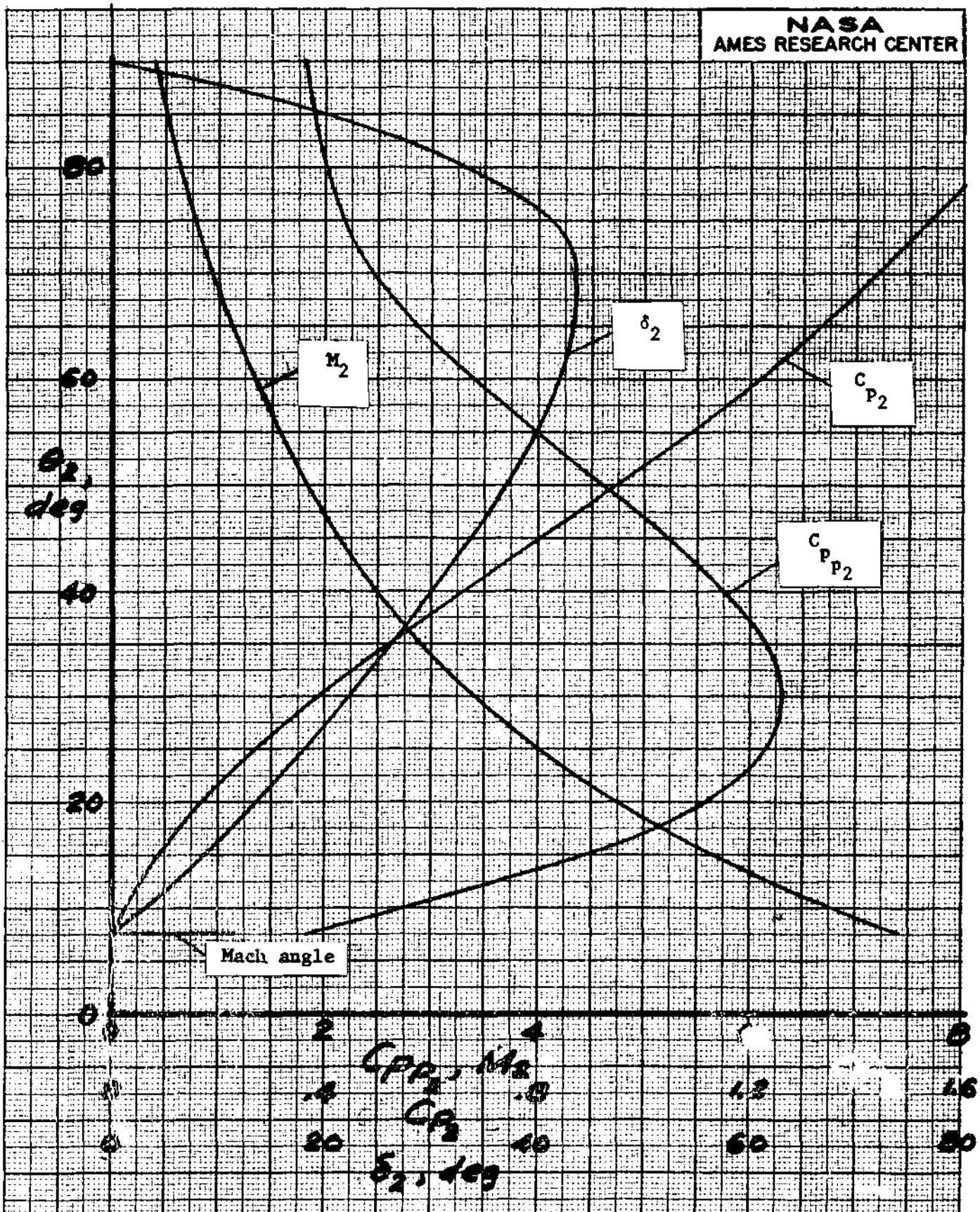

(a) Single oblique wave

Figure 5.- Oblique-shock wave characteristics, $M_\infty = 7.4$.

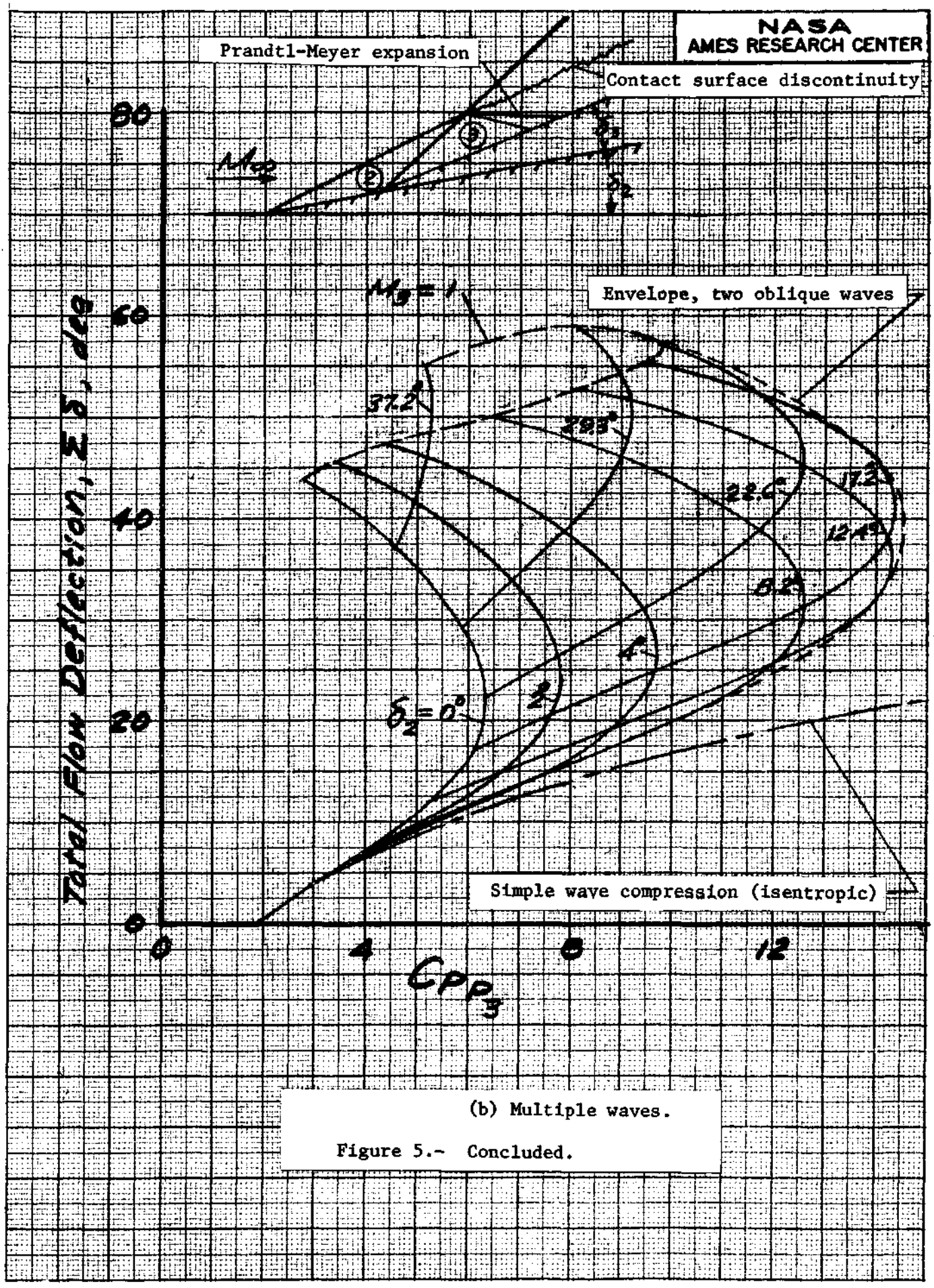

(b) Multiple waves.

Figure 5.- Concluded.

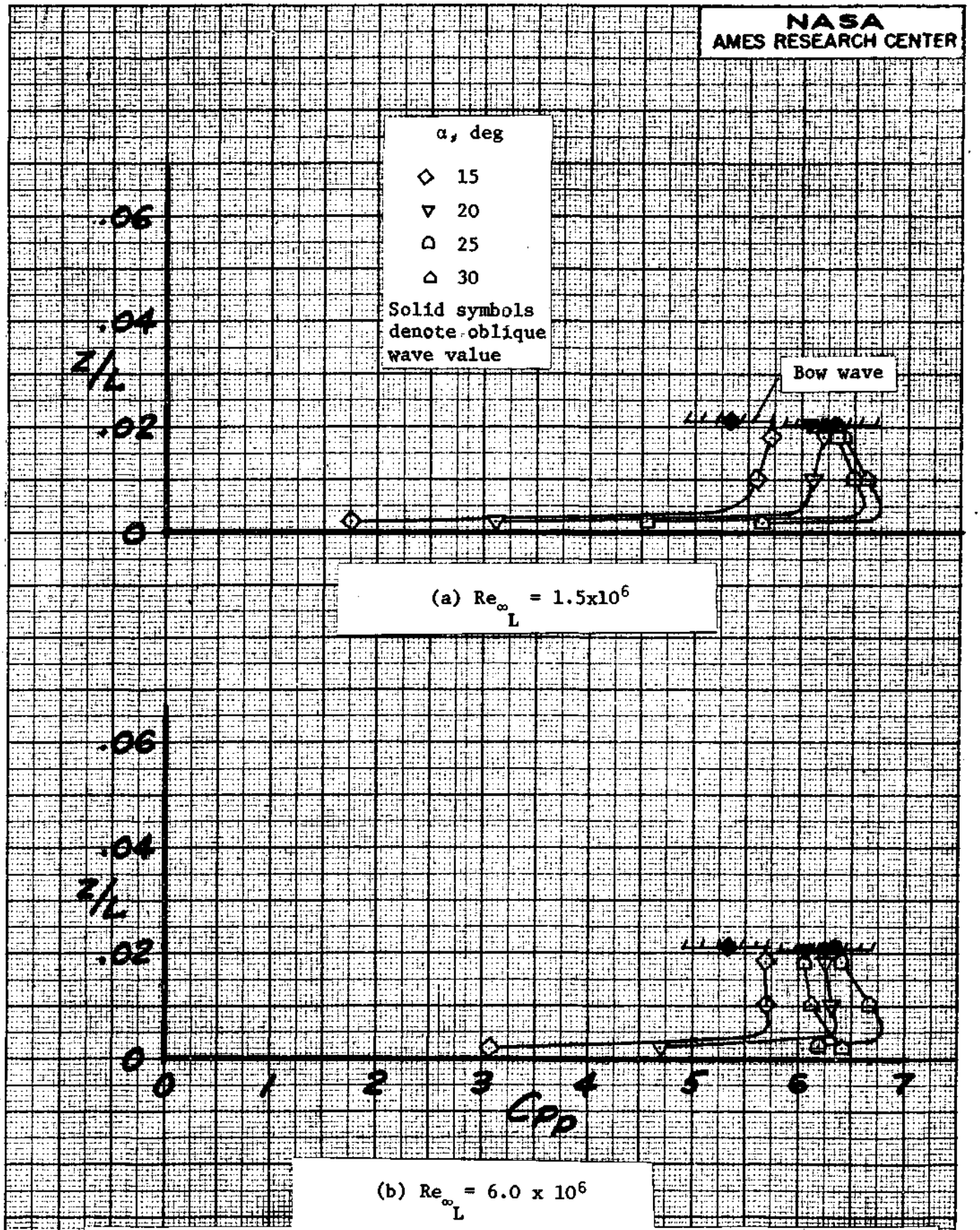

Figure 6.- Pitot-pressure distributions of the flow field on the windward side at X/L = 0.35. M_∞ = 7.4.

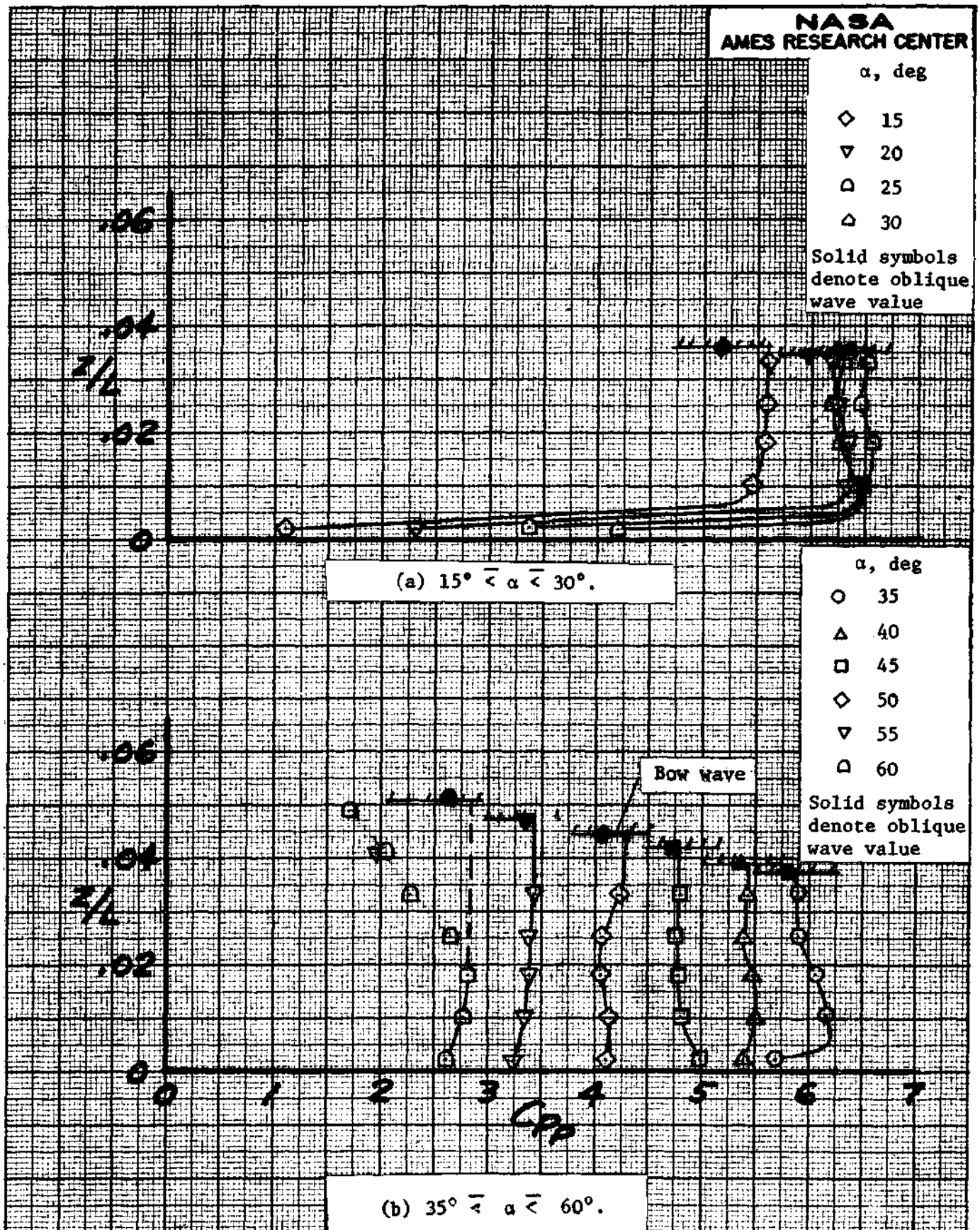

Figure 7.- Pitot-pressure distributions of the flow field on the windward side at X/L = 0.60. M_∞ = 7.4, Re_{∞_L} = 1.5x10^6.

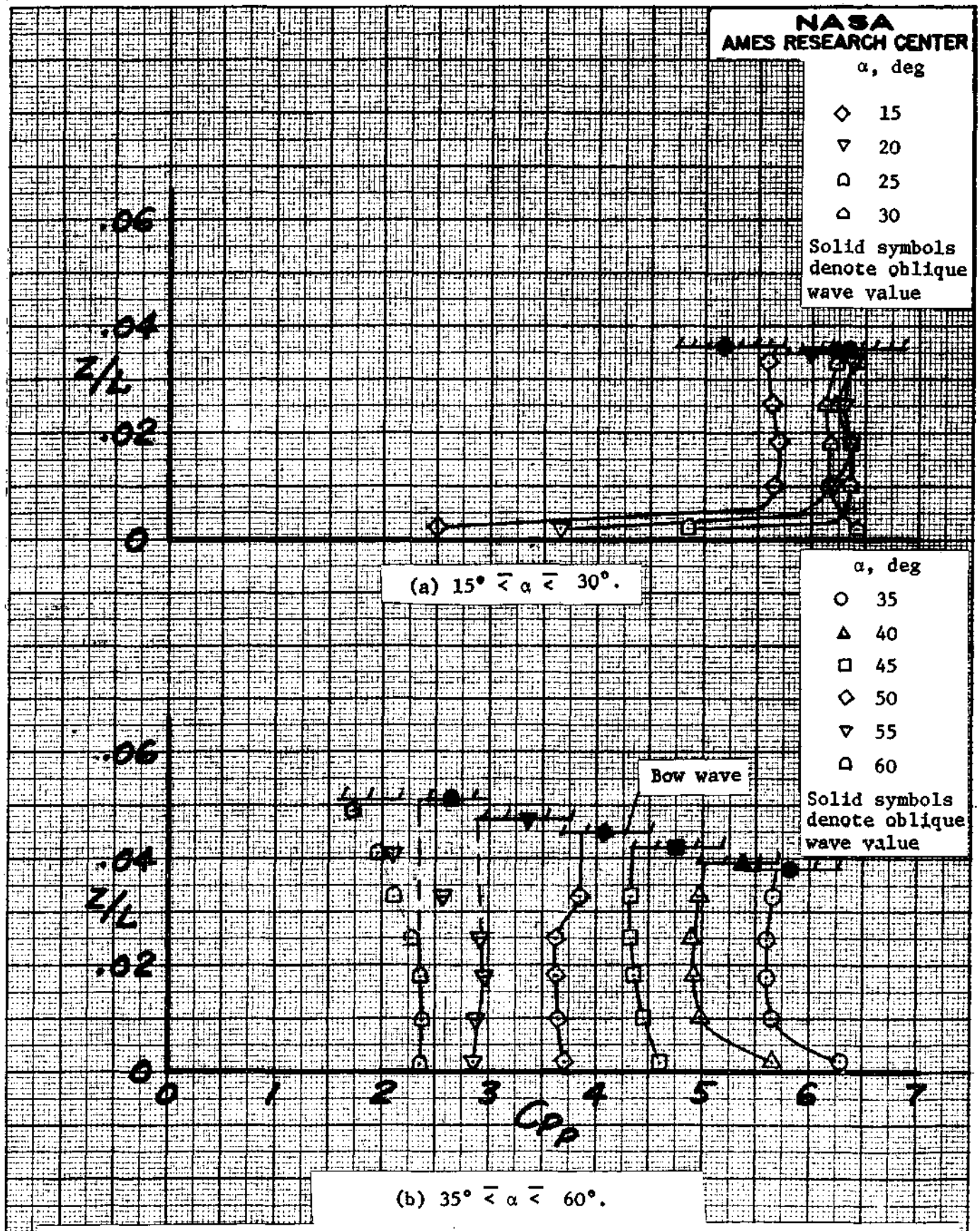

(a) $15° \leq \alpha \leq 30°$.

(b) $35° \leq \alpha \leq 60°$.

Figure 8.- Pitot-pressure distributions of the flow field on the windward side at $X/L = 0.60$. $M_\infty = 7.4$, $Re_{\infty_L} = 6.0 \times 10^6$.

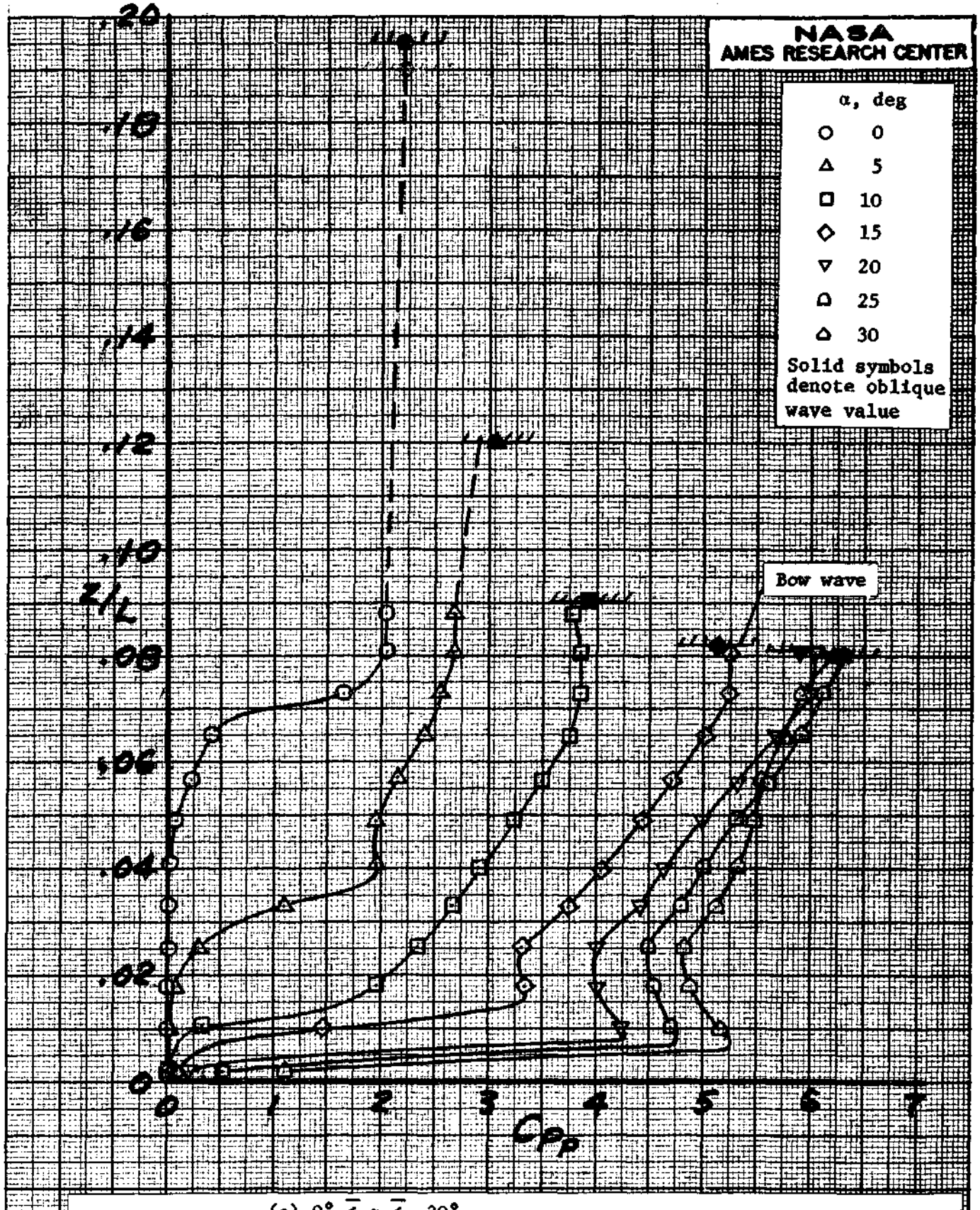

(a) $0° \leq \alpha \leq 30°$.

Figure 9.- Pitot-pressure distributions of the flow field on the windward side at $X/L = 0.98$. $M_\infty = 7.4$, $Re_{\infty_L} = 1.5 \times 10^6$.

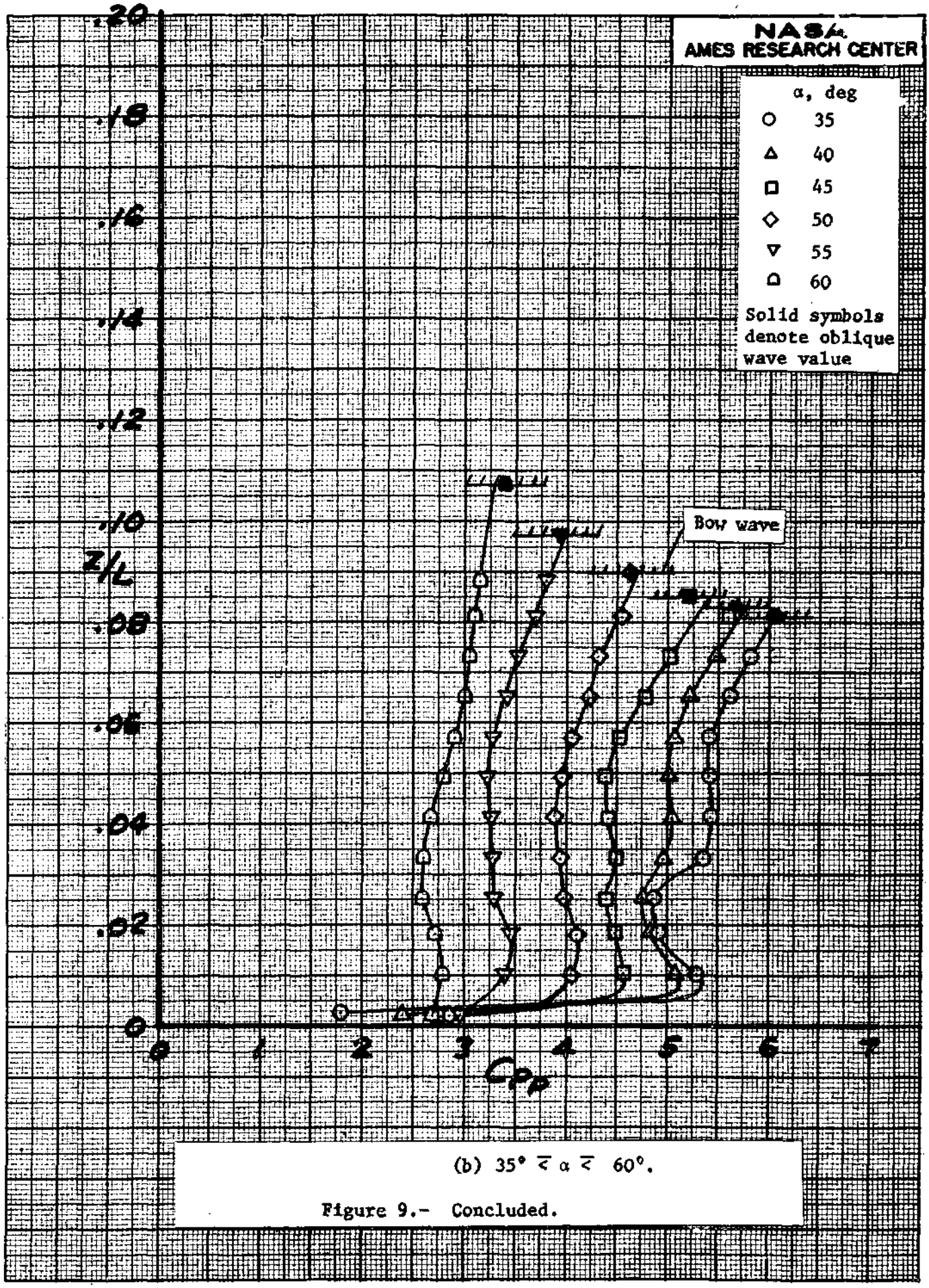

(b) $35° \leq \alpha \leq 60°$.

Figure 9.- Concluded.

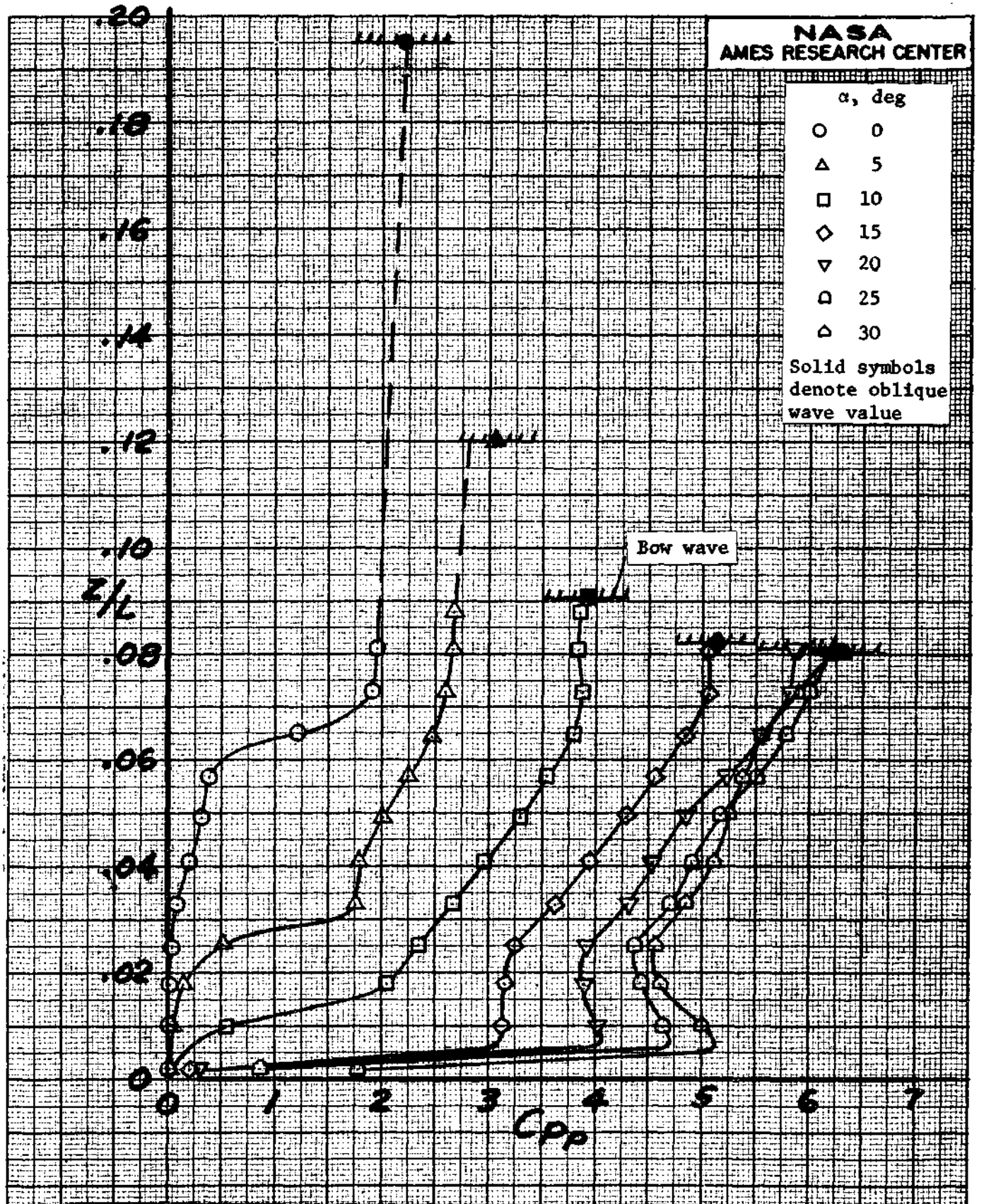

Figure 10.- Pitot-pressure distributions of the flow field on the windward side at X/L = 0.98. Re_{∞_L} = 3.0×10^6.

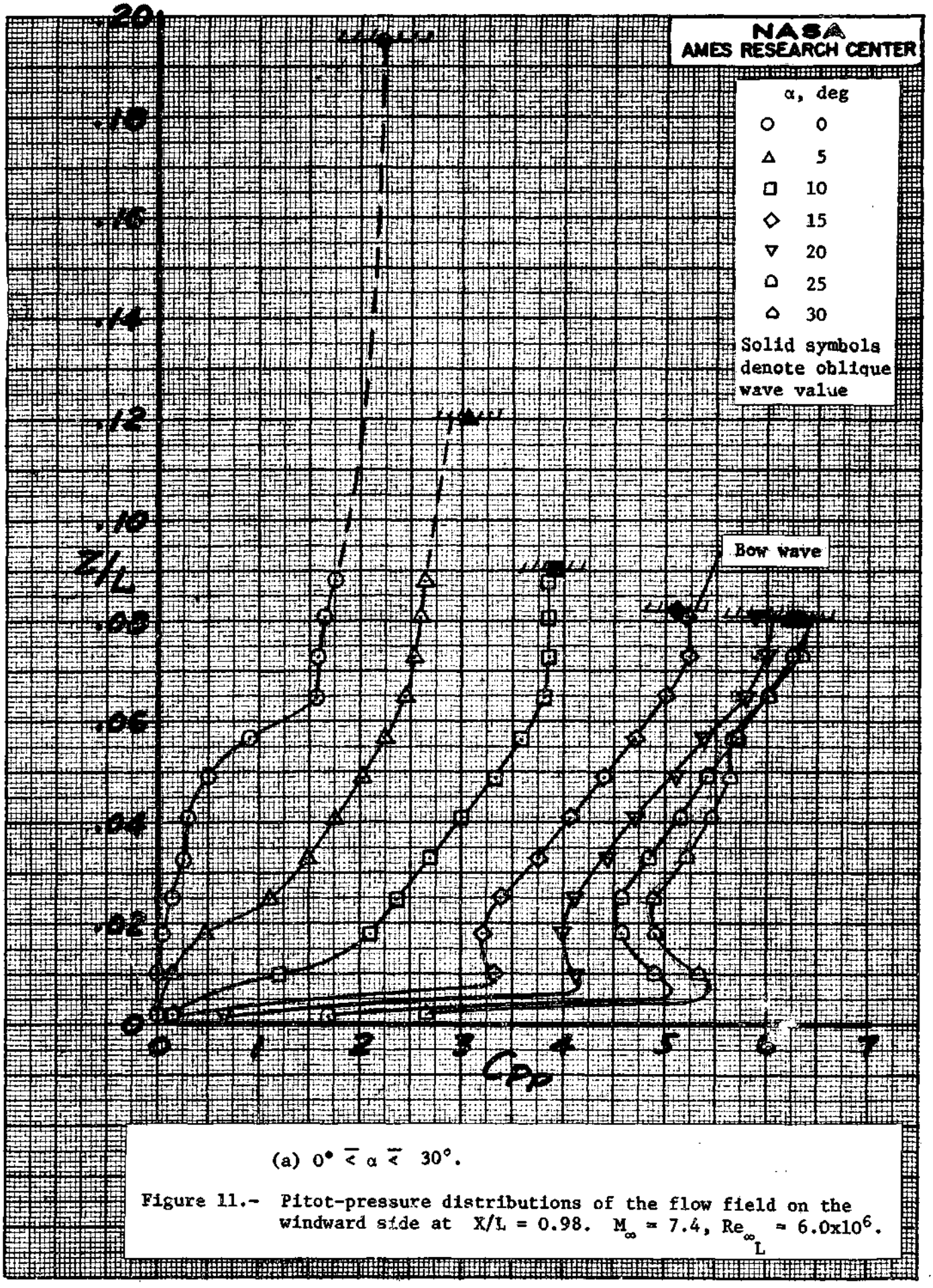

(a) $0° \leq \alpha \leq 30°$.

Figure 11.- Pitot-pressure distributions of the flow field on the windward side at $X/L = 0.98$. $M_\infty = 7.4$, $Re_{\infty_L} = 6.0 \times 10^6$.

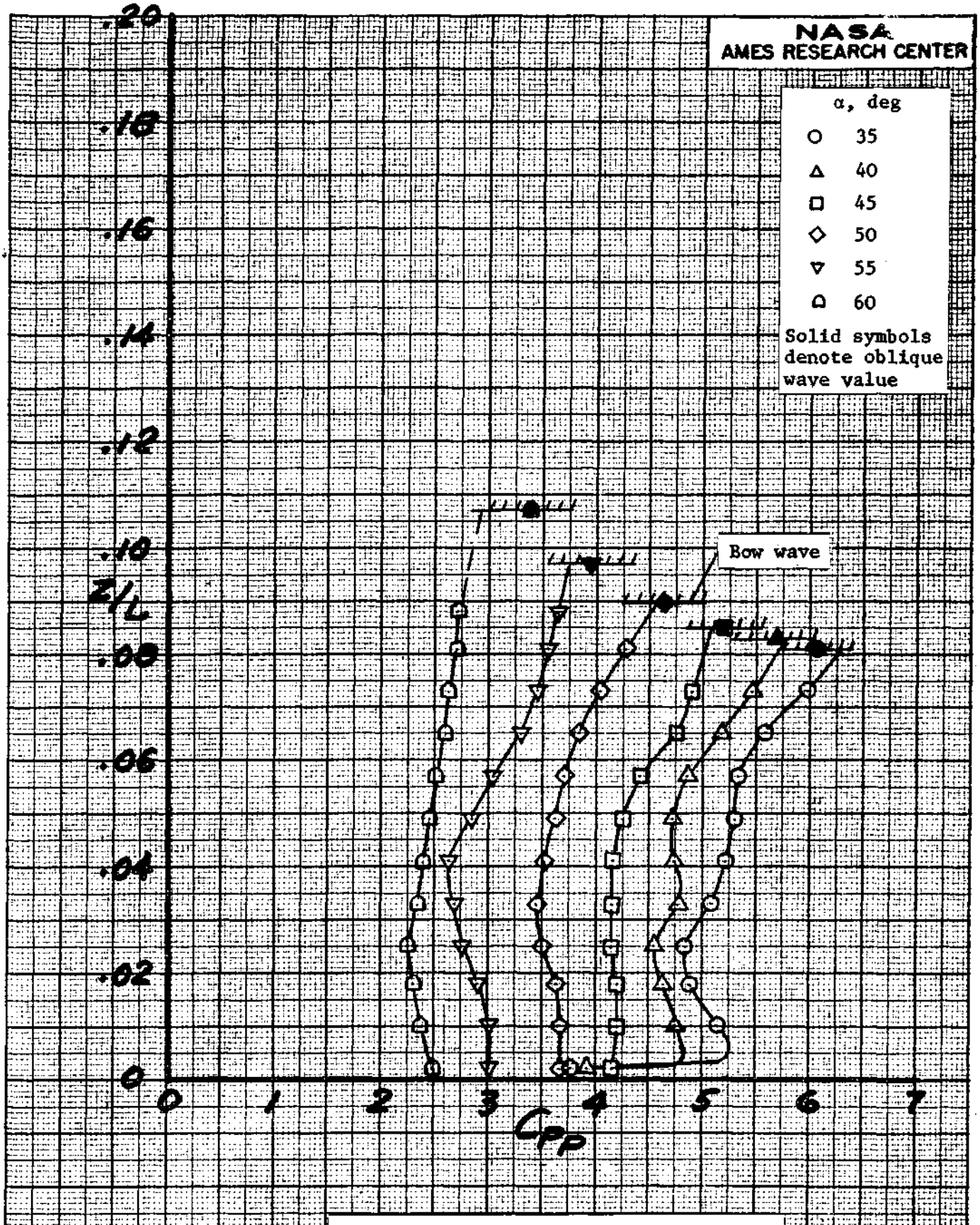

(b) $35° \leq \alpha \leq 60°$.

Figure 11.- Concluded.

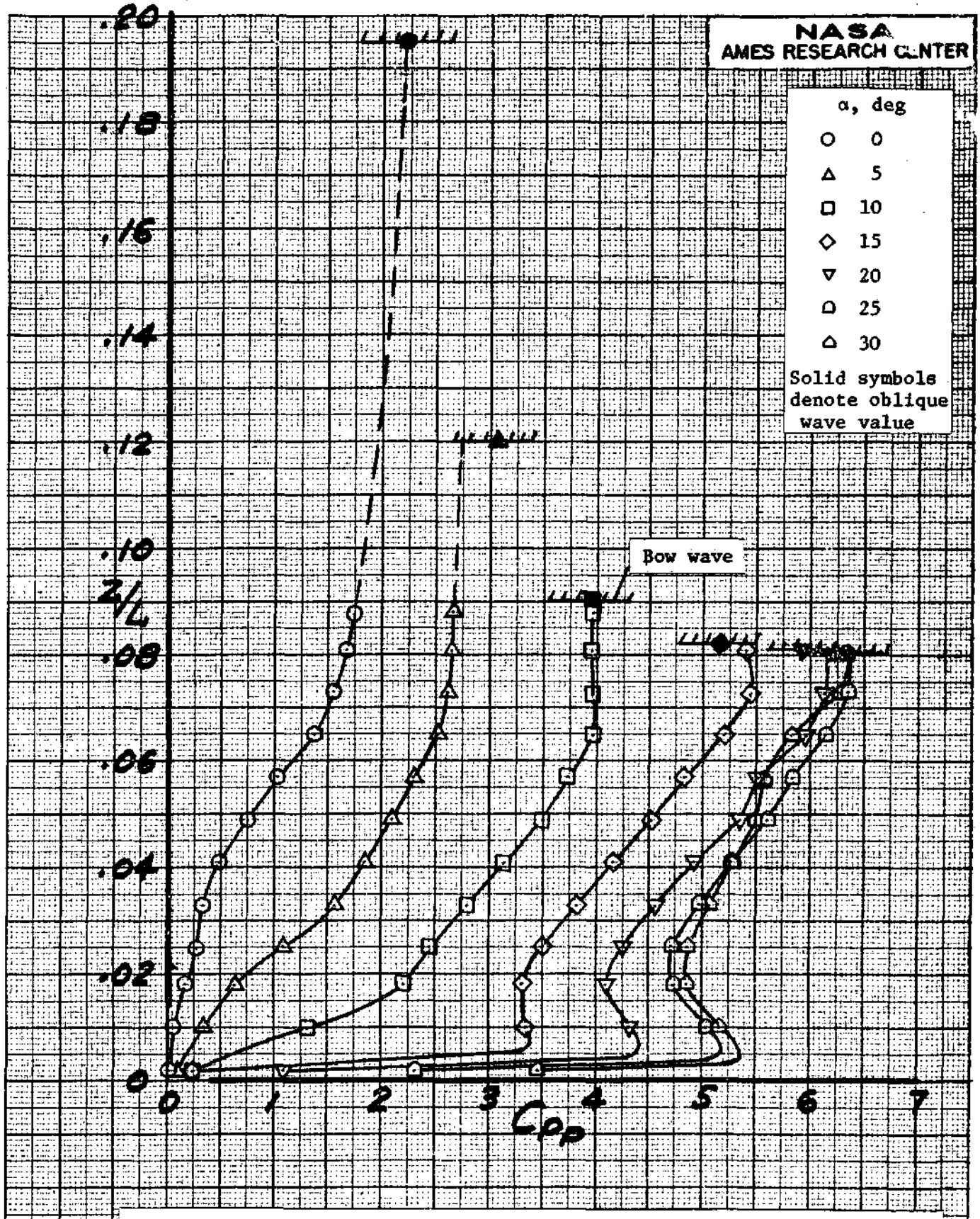

Figure 12.- Pitot-pressure distributions of the flow field on the windward side at X/L = 0.98. M_∞ = 7.4, Re_{∞_L} = 9.0x10^6.

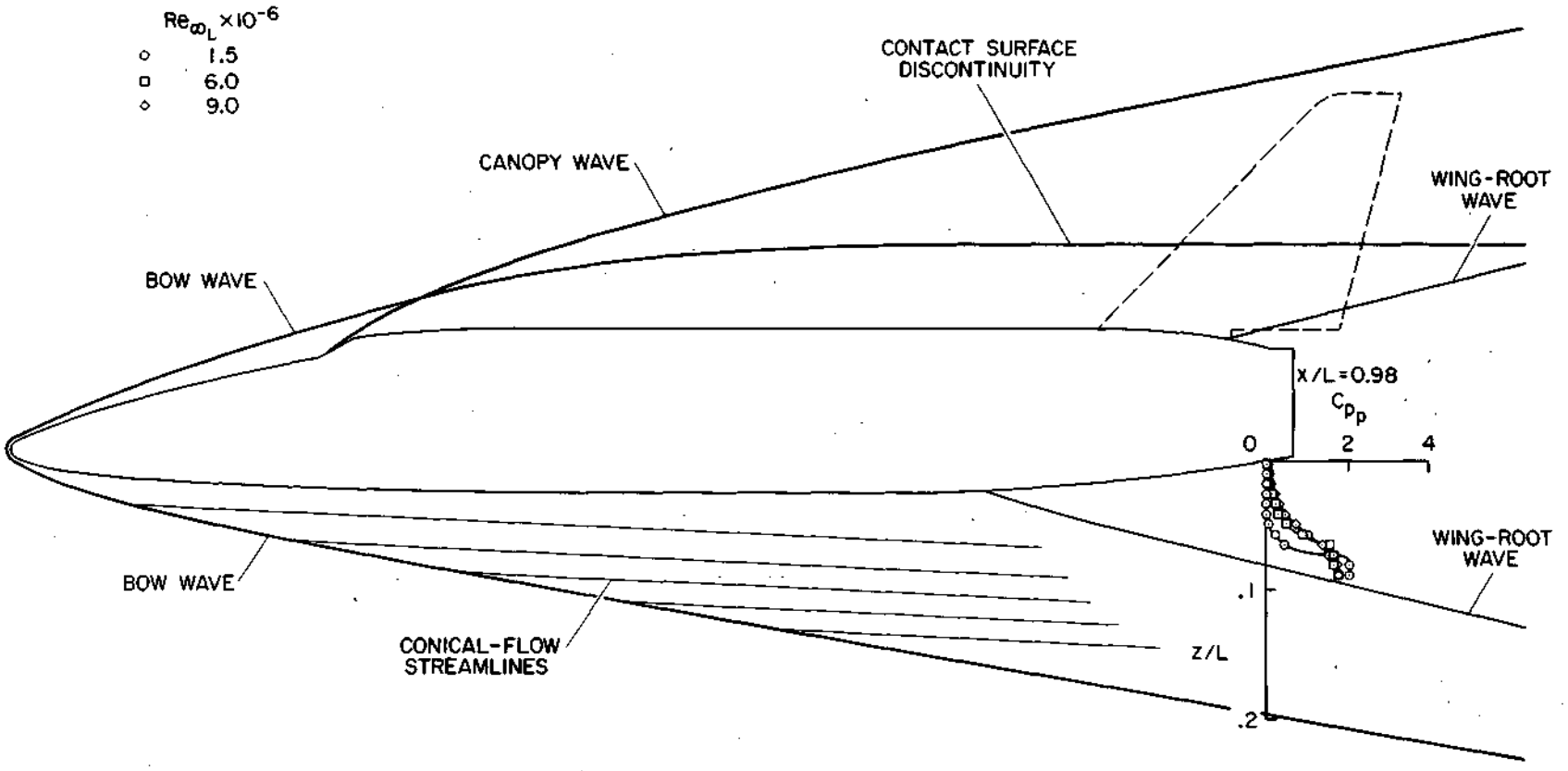

(a) $\alpha = 0°$.

Figure 13.- Composite of the shock-wave pattern and pitot-pressure distribution of the windward flow field. $M_\infty = 7.4$.

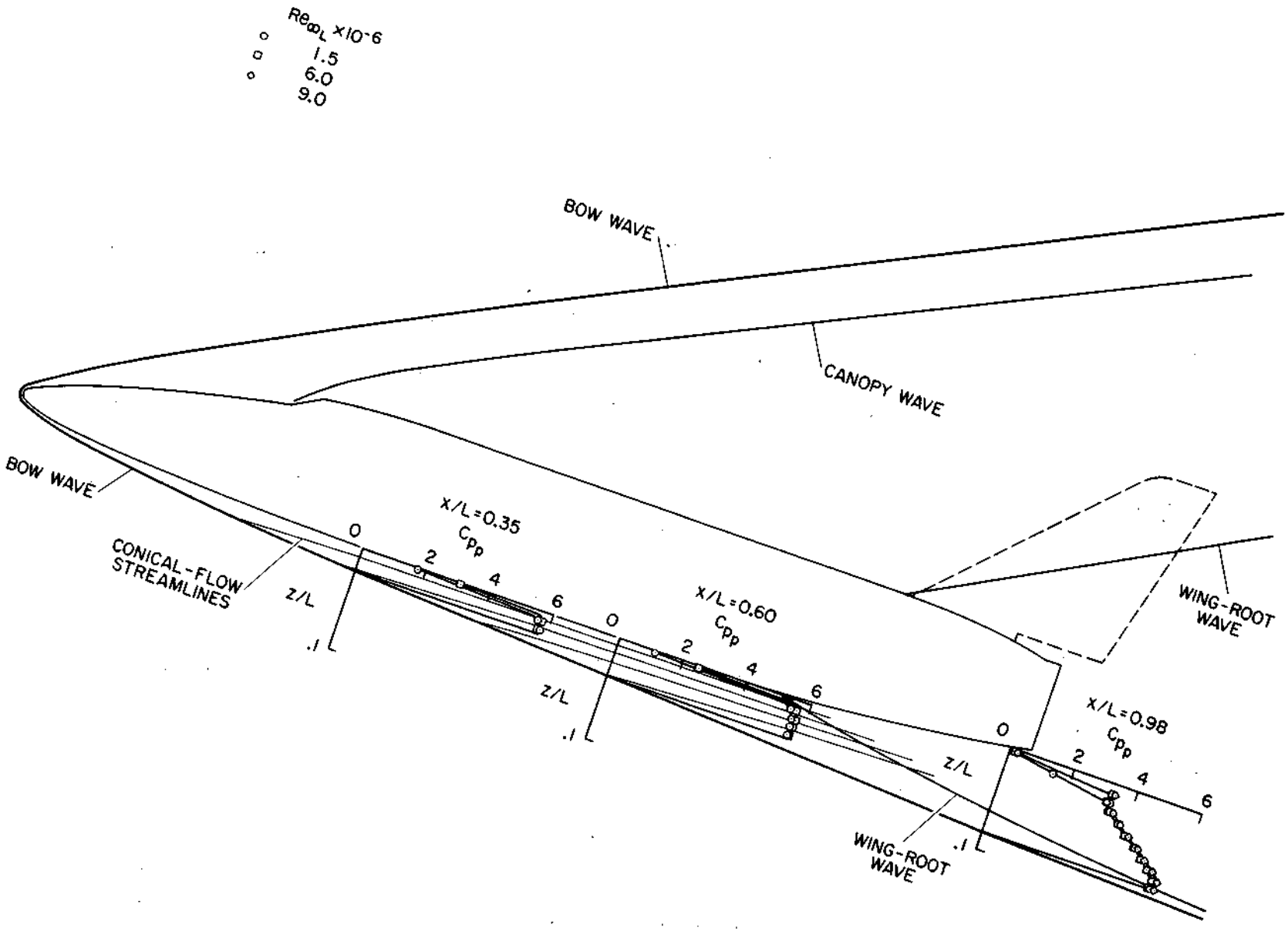

(b) $\alpha = 15°$.

Figure 13.- Continued.

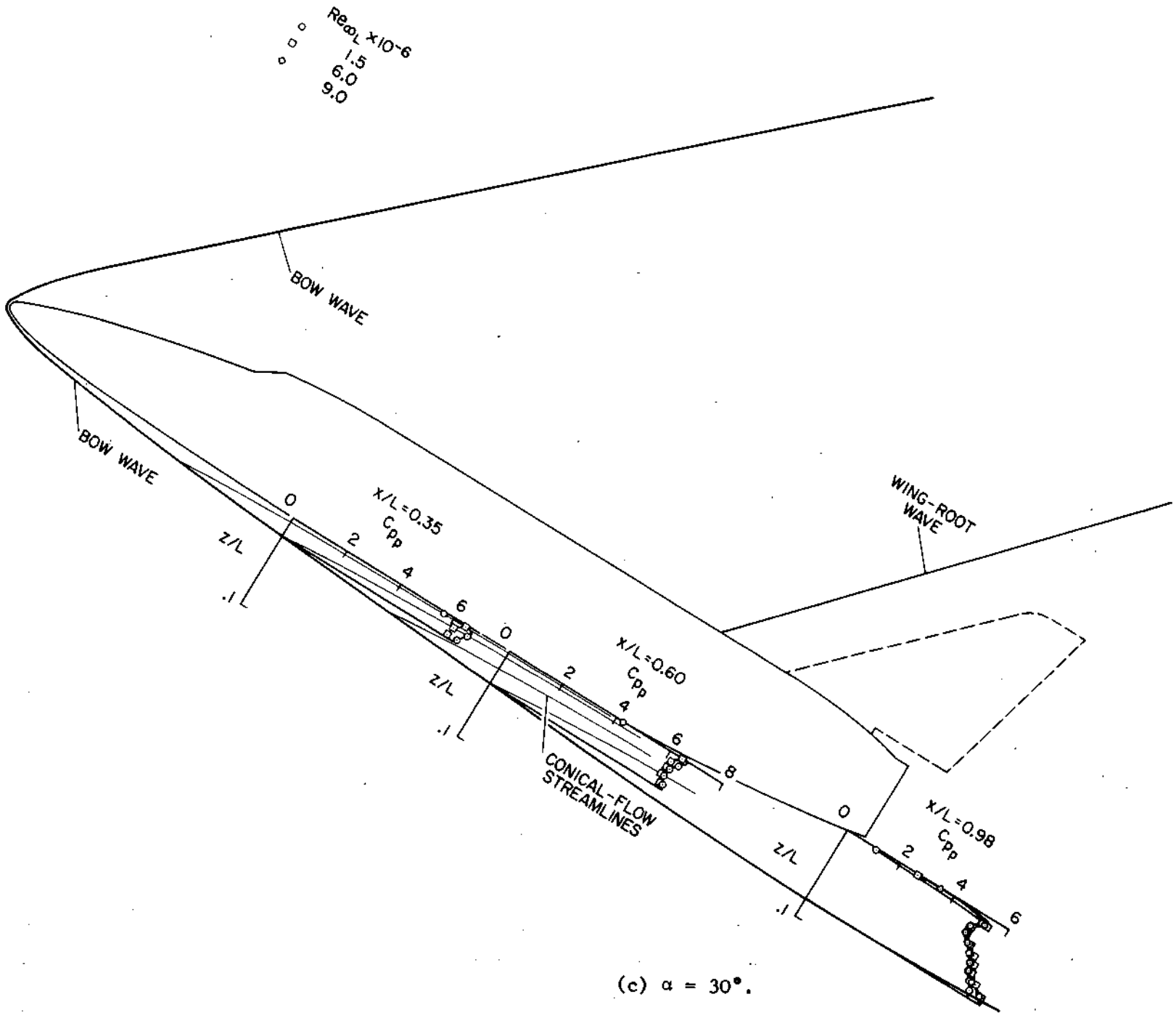

(c) $\alpha = 30°$.

Figure 13.- Continued.

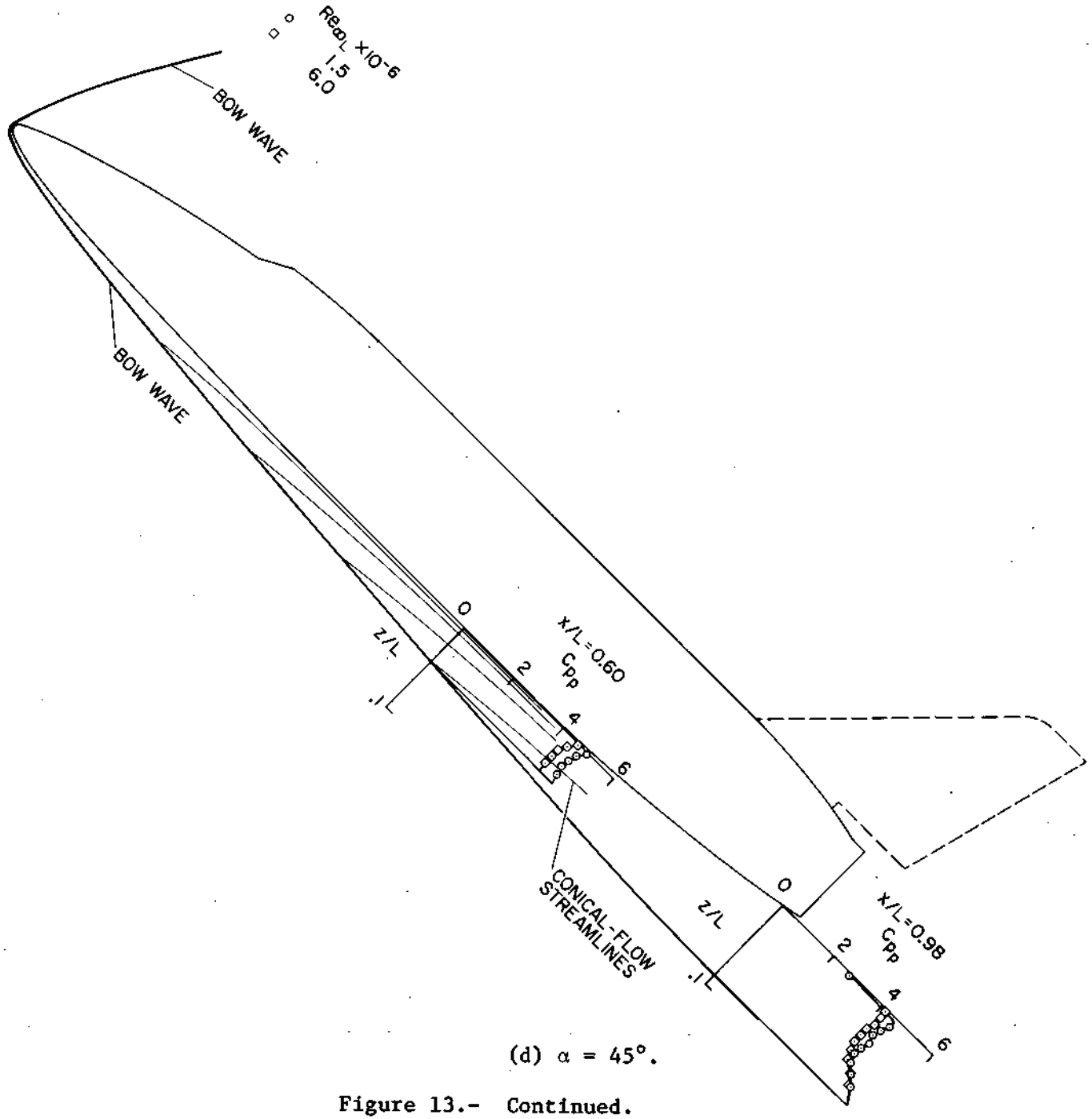

(d) α = 45°.

Figure 13.- Continued.

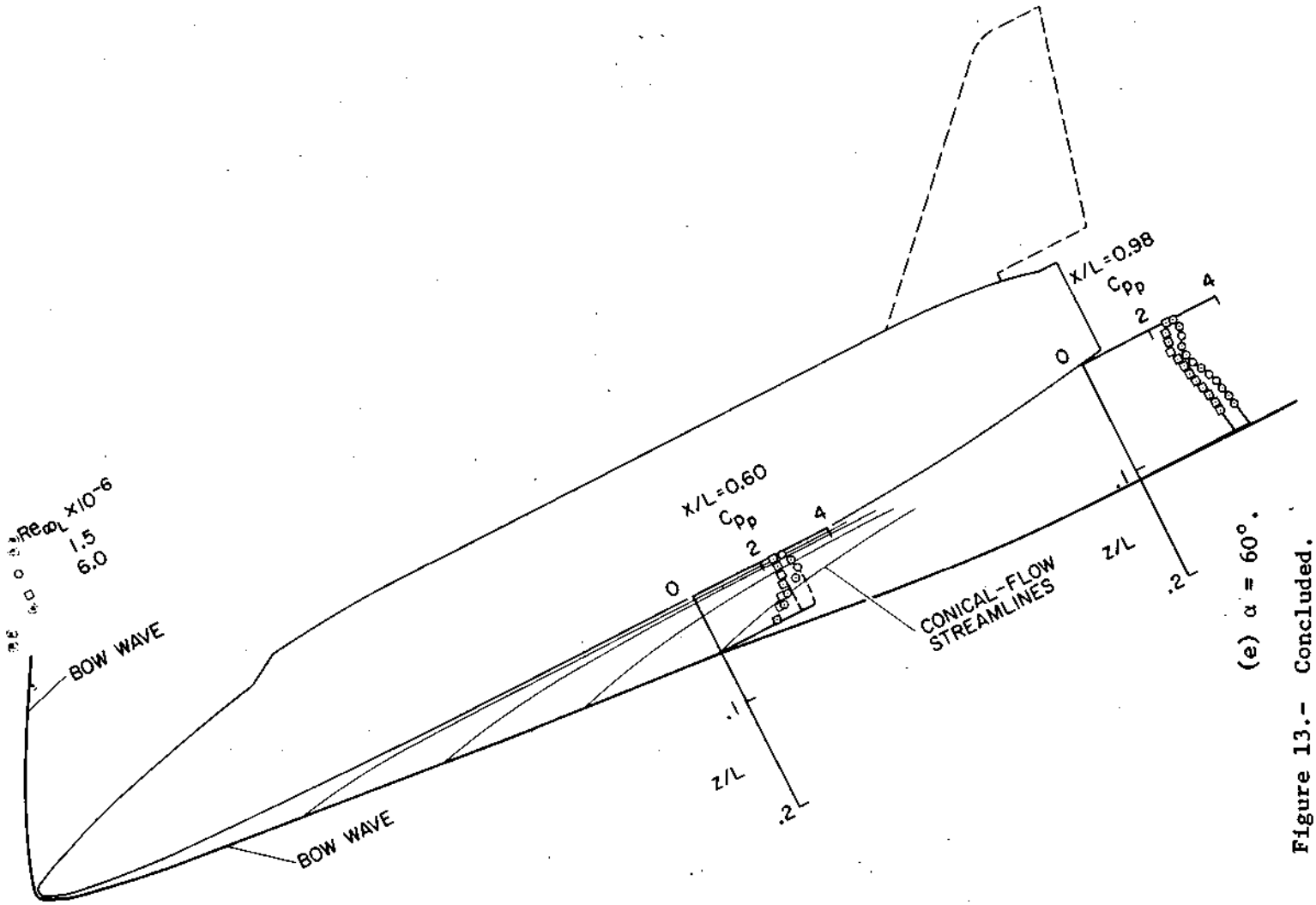

(e) $\alpha = 60°$.

Figure 13.- Concluded.

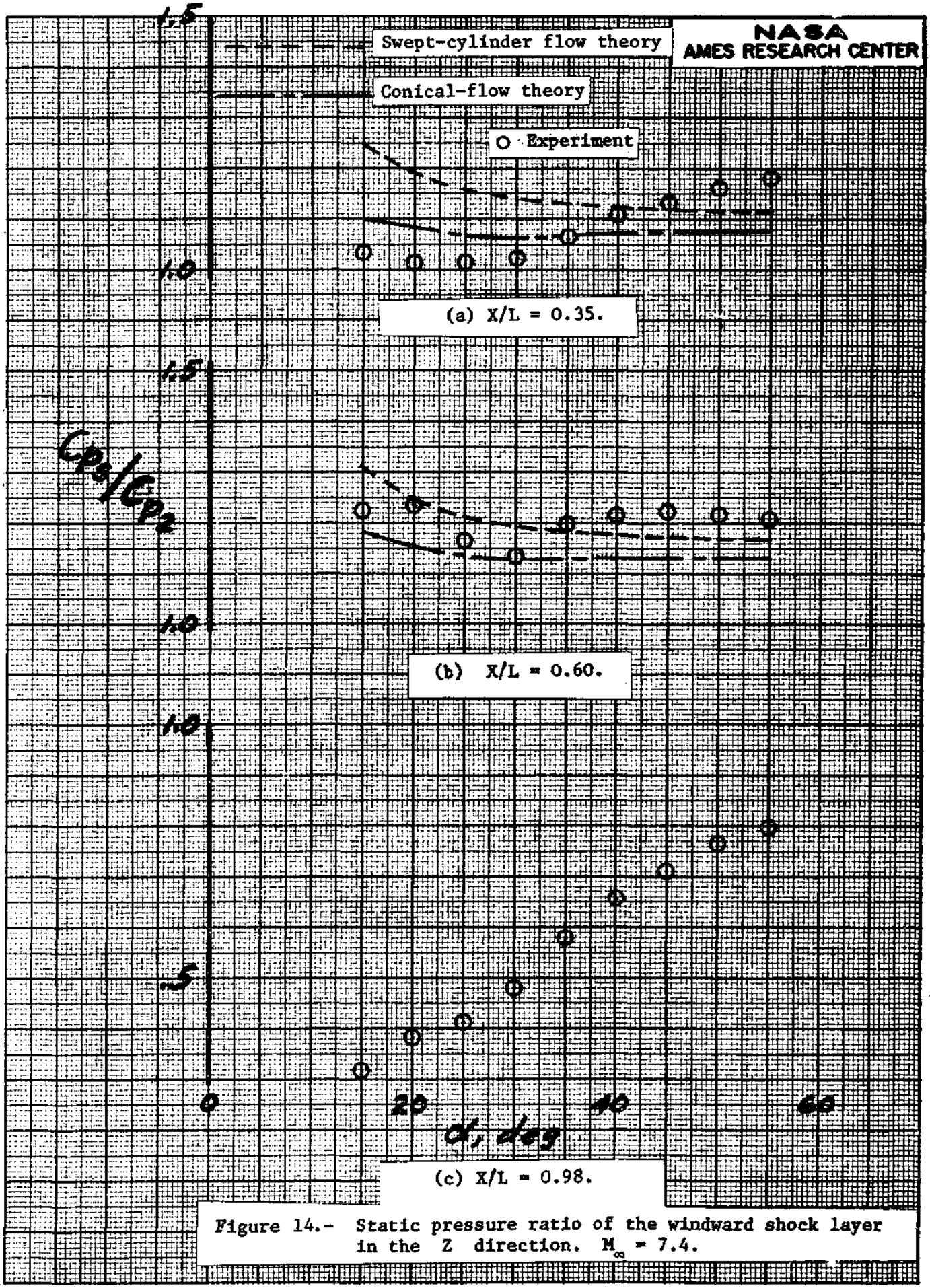

Figure 14.- Static pressure ratio of the windward shock layer in the Z direction. $M_\infty = 7.4$.

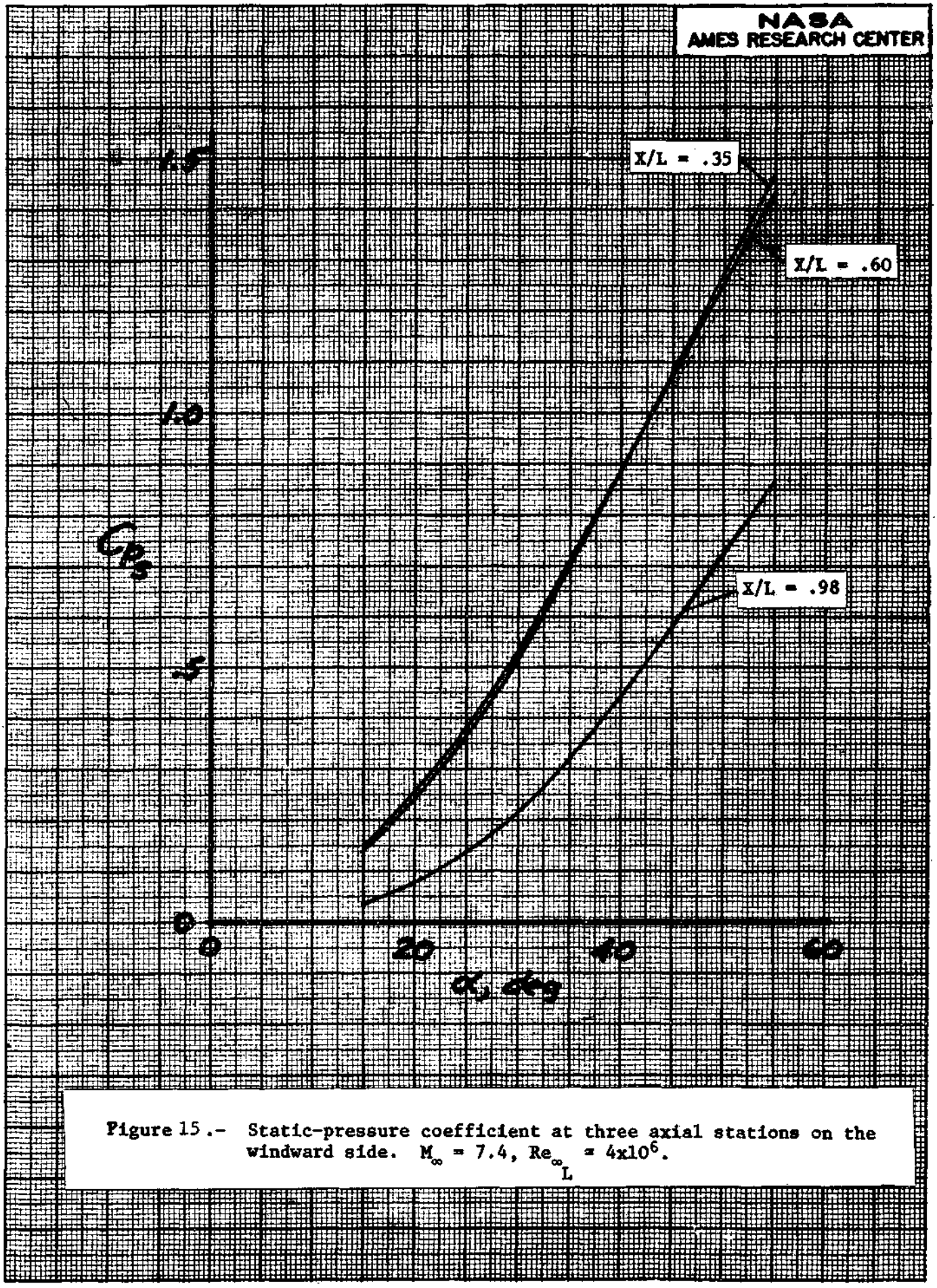

Figure 15.- Static-pressure coefficient at three axial stations on the windward side. $M_\infty = 7.4$, $Re_{\infty_L} = 4 \times 10^6$.

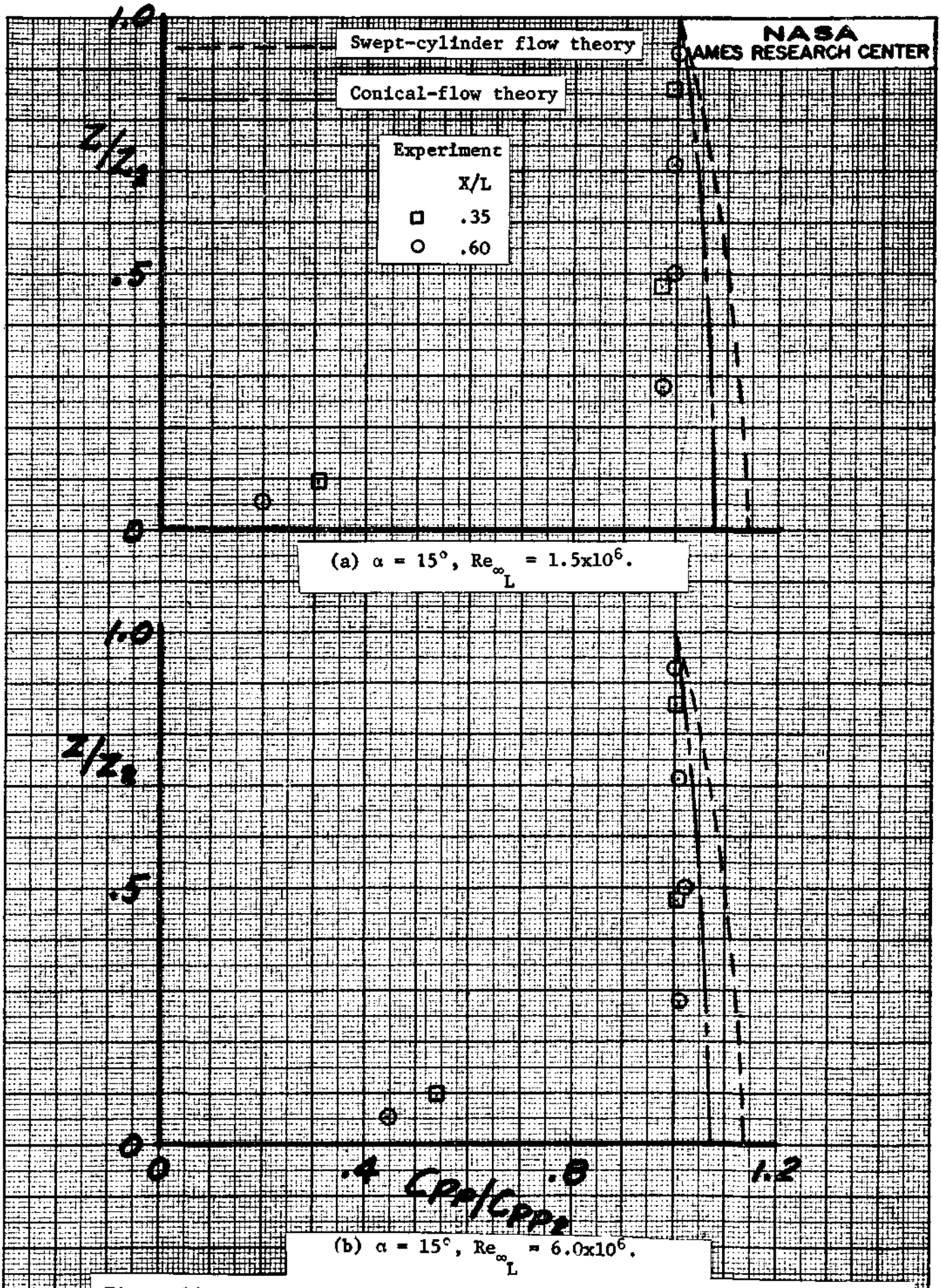

Figure 16.- Comparison of pitot-pressure distributions with theory.

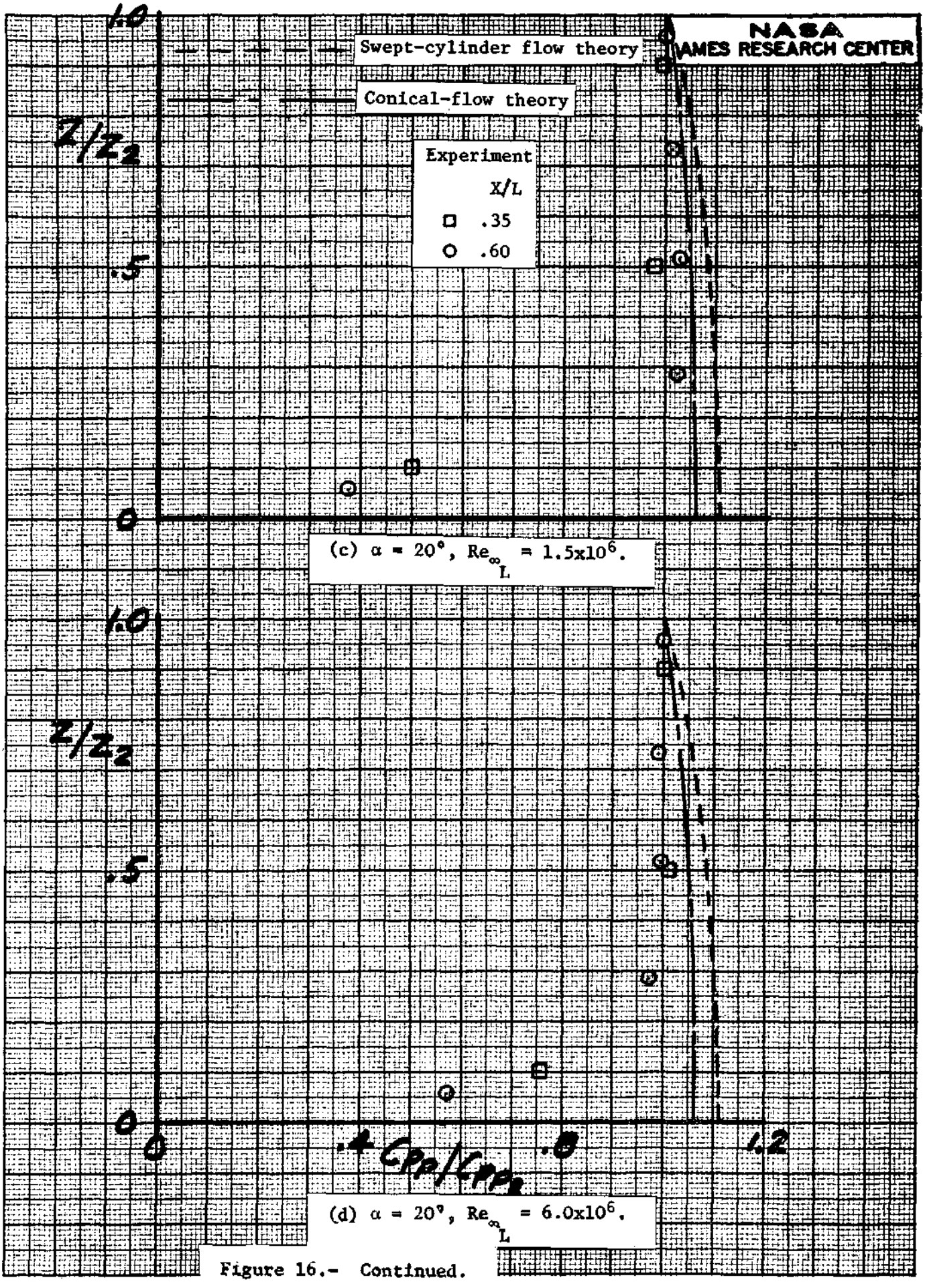

Figure 16.- Continued.

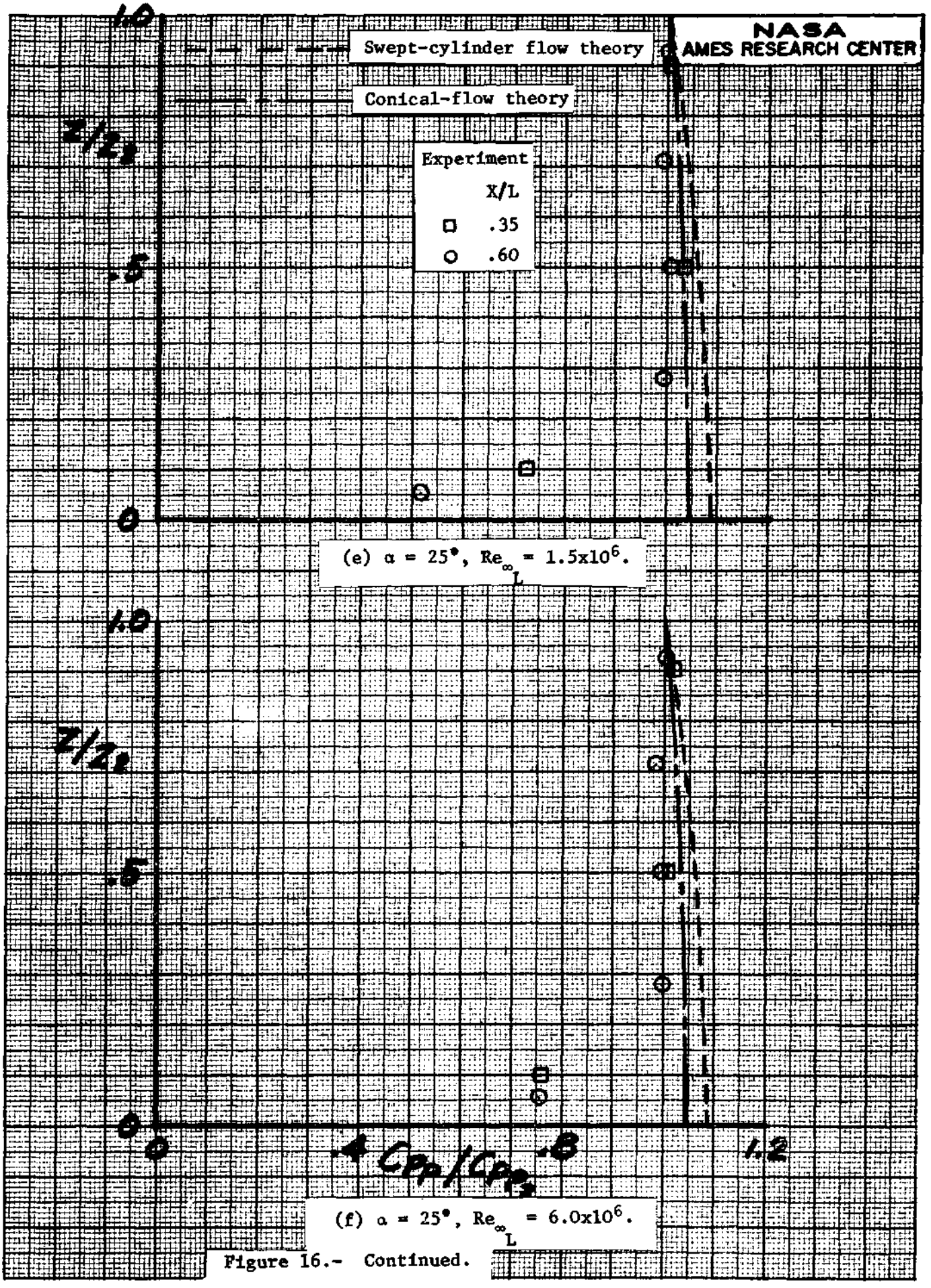

Figure 16.- Continued.

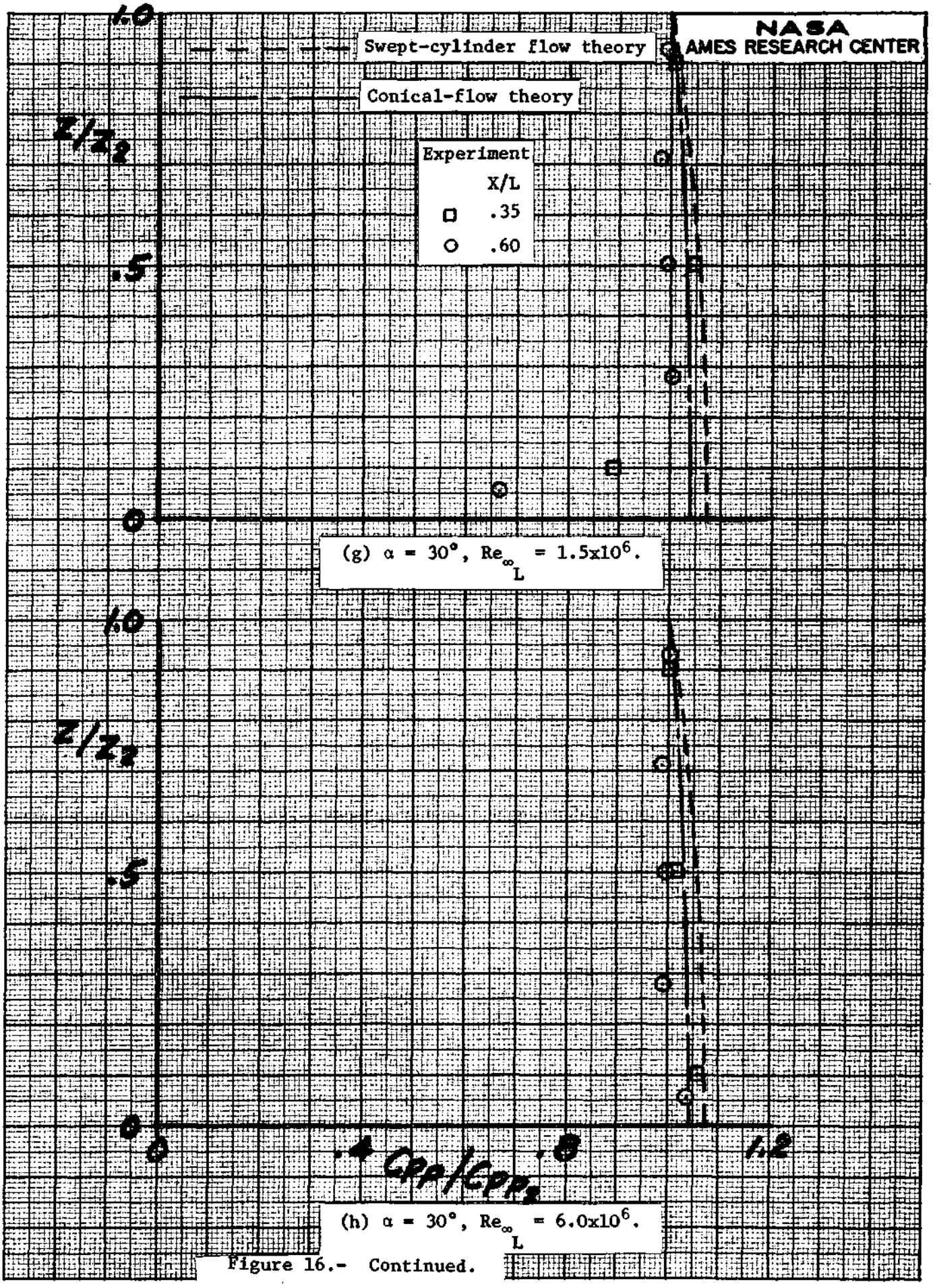

Figure 16.- Continued.

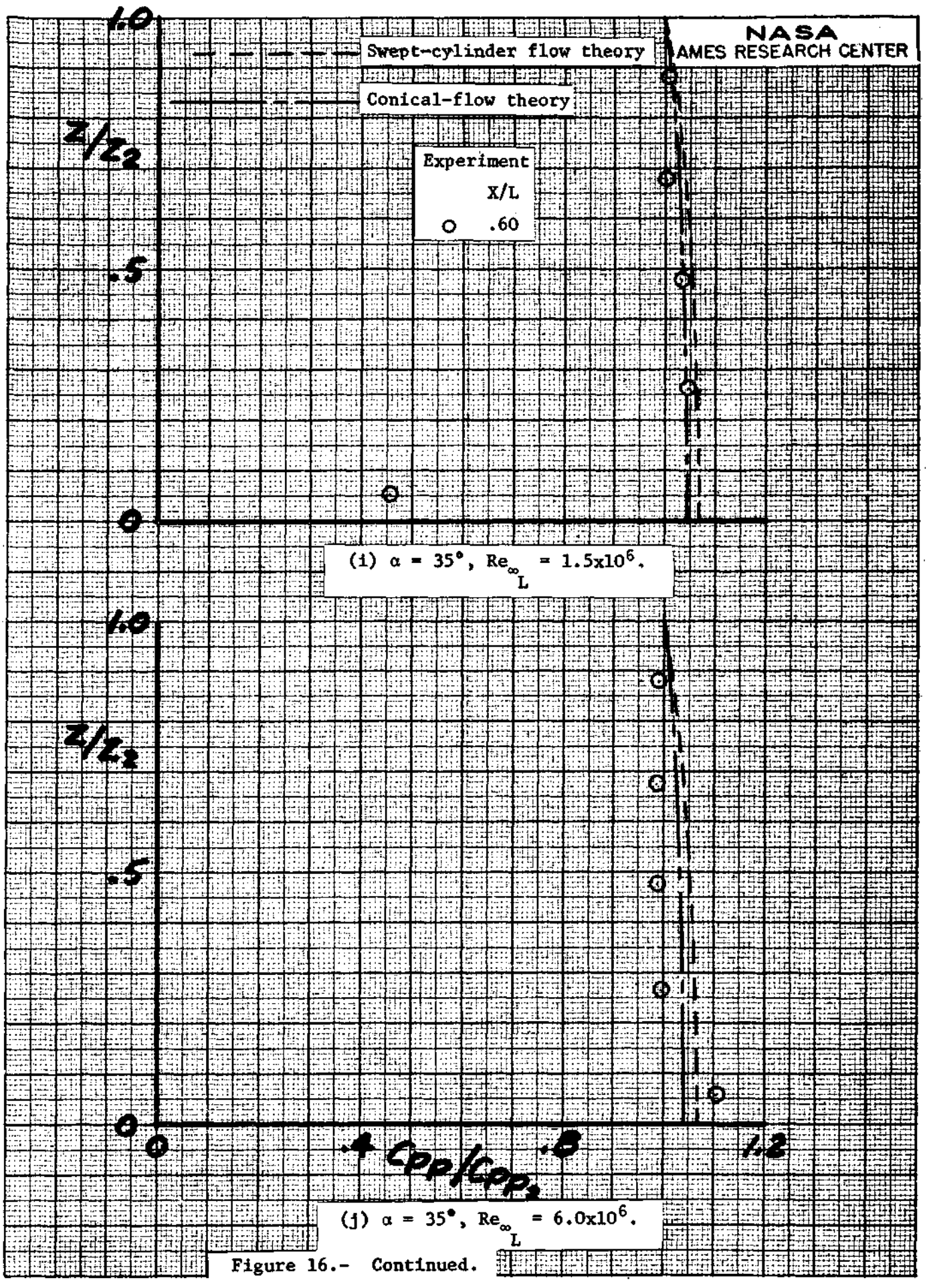

Figure 16.- Continued.

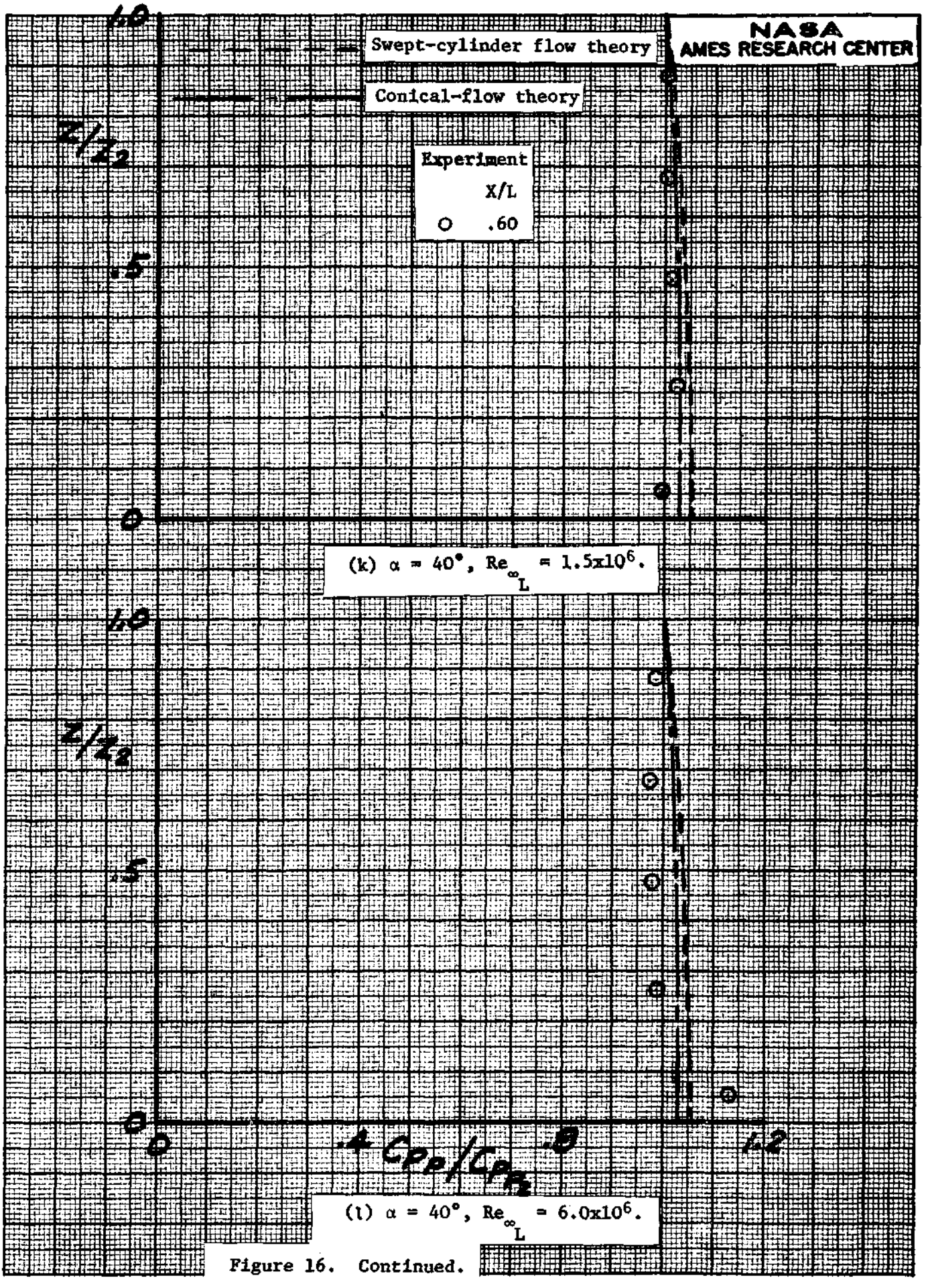

Figure 16. Continued.

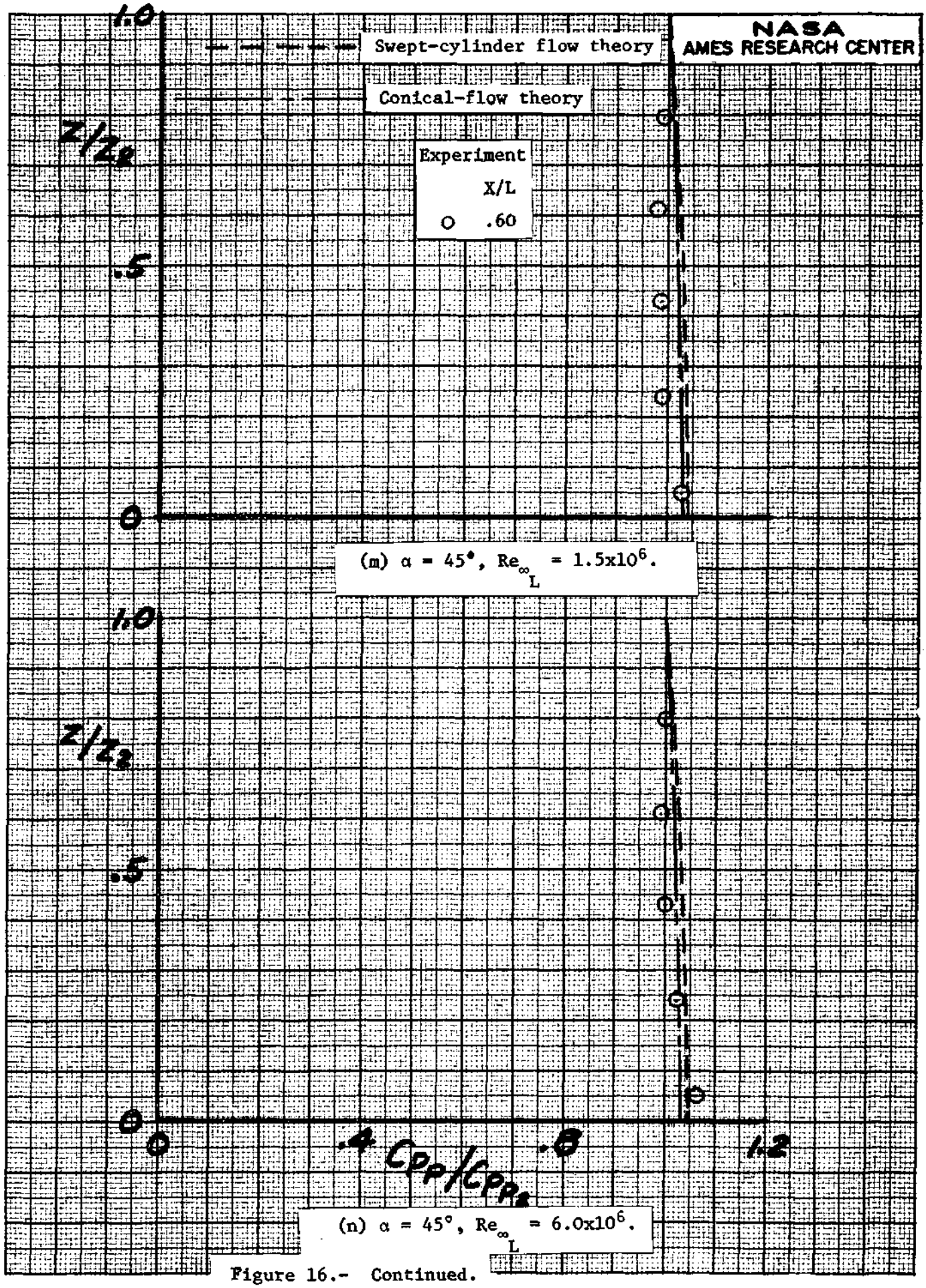

Figure 16.- Continued.

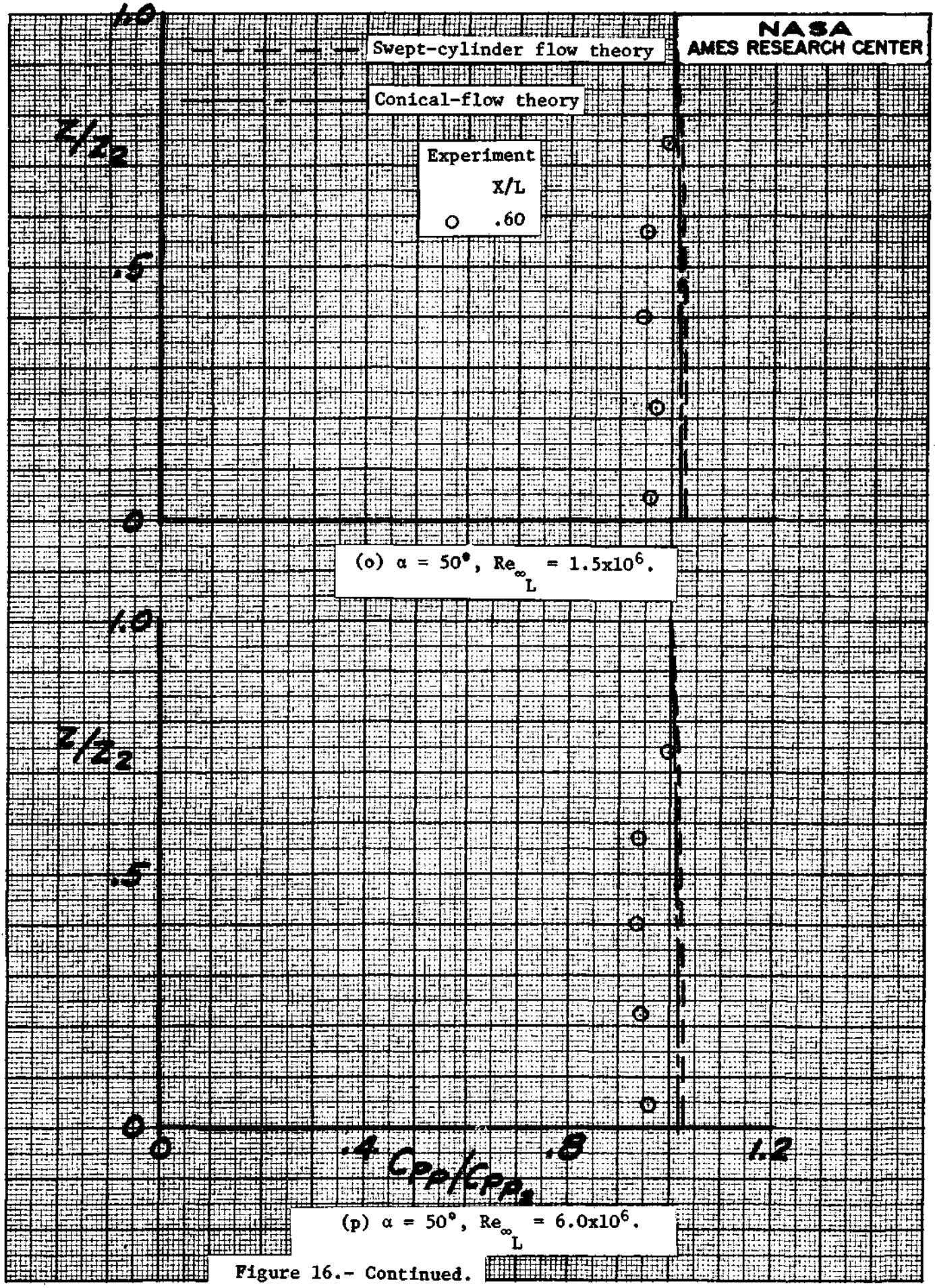

Figure 16.- Continued.

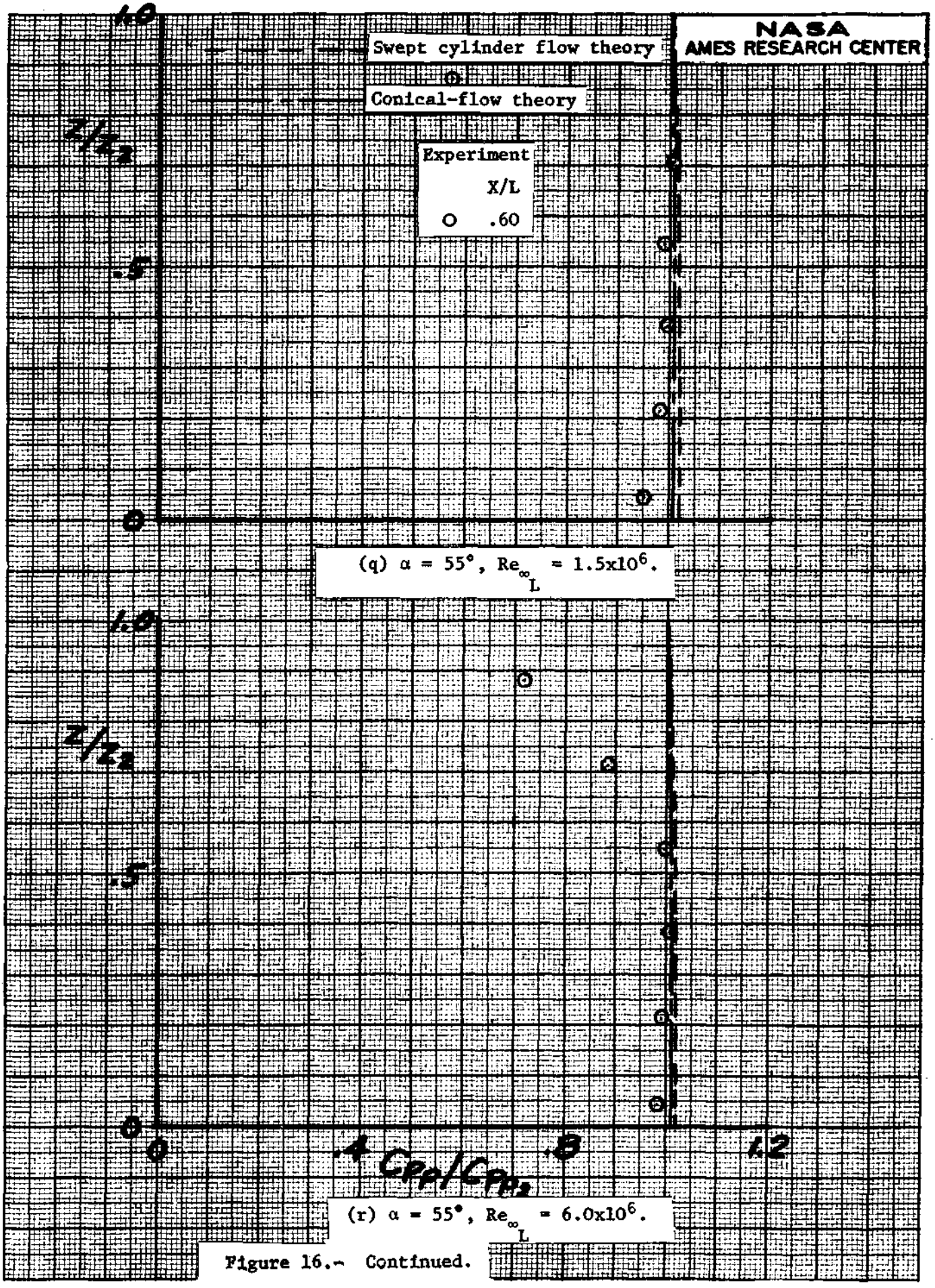

Figure 16.- Continued.

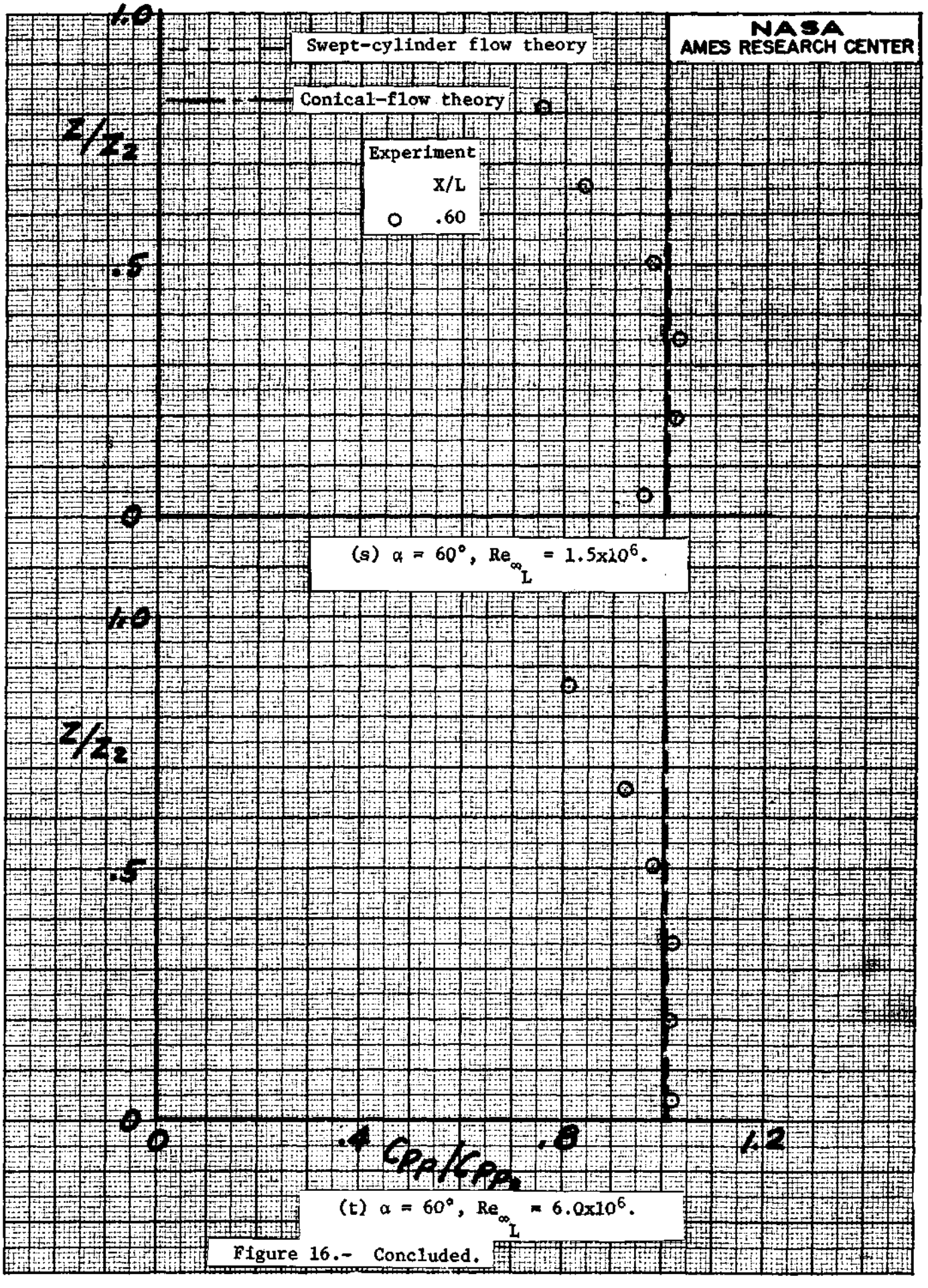

Figure 16.- Concluded.

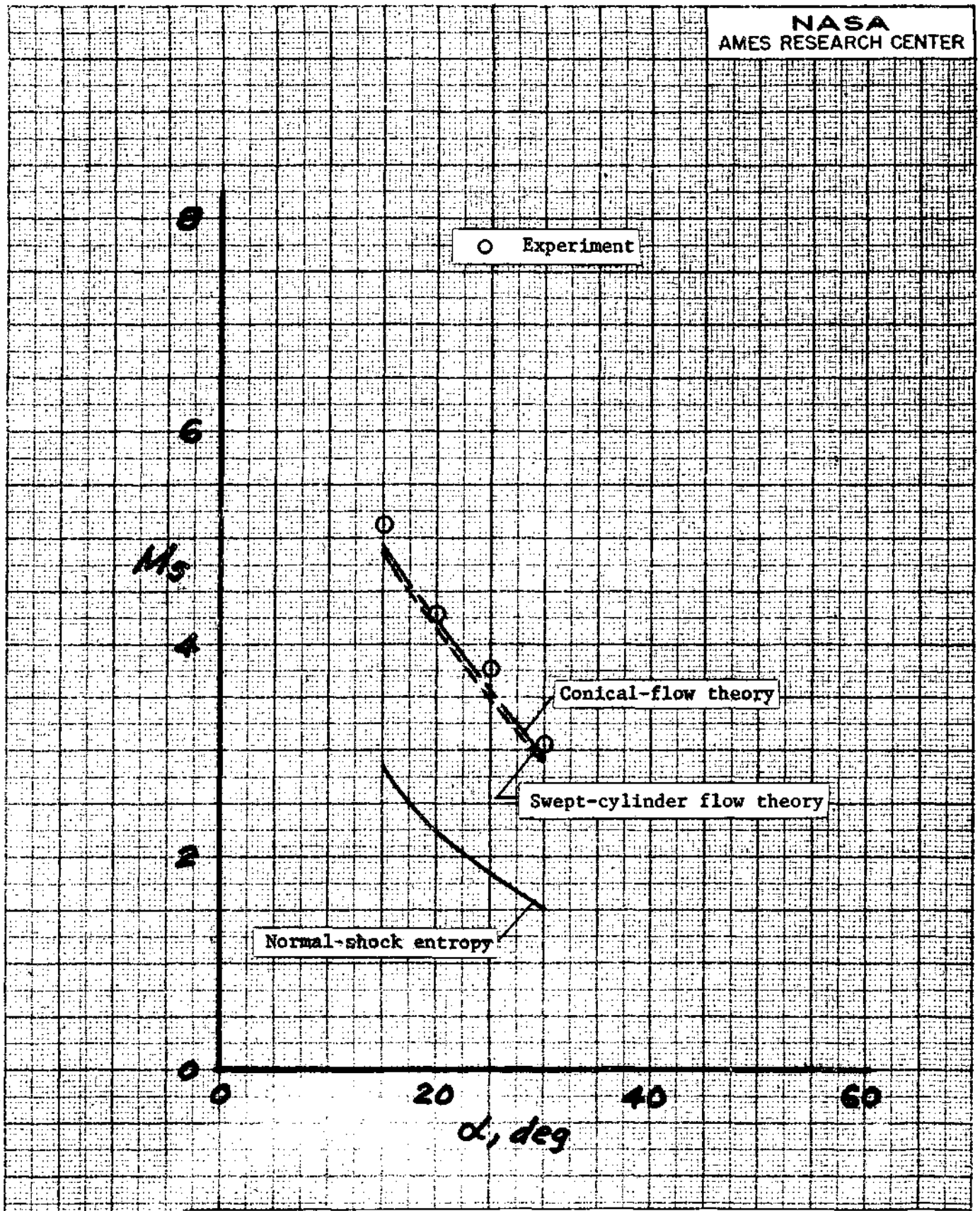

(a) X/L = 0.35.

Figure 17.- Local Mach number at the surface on the windward centerline. $M_\infty = 7.4$.

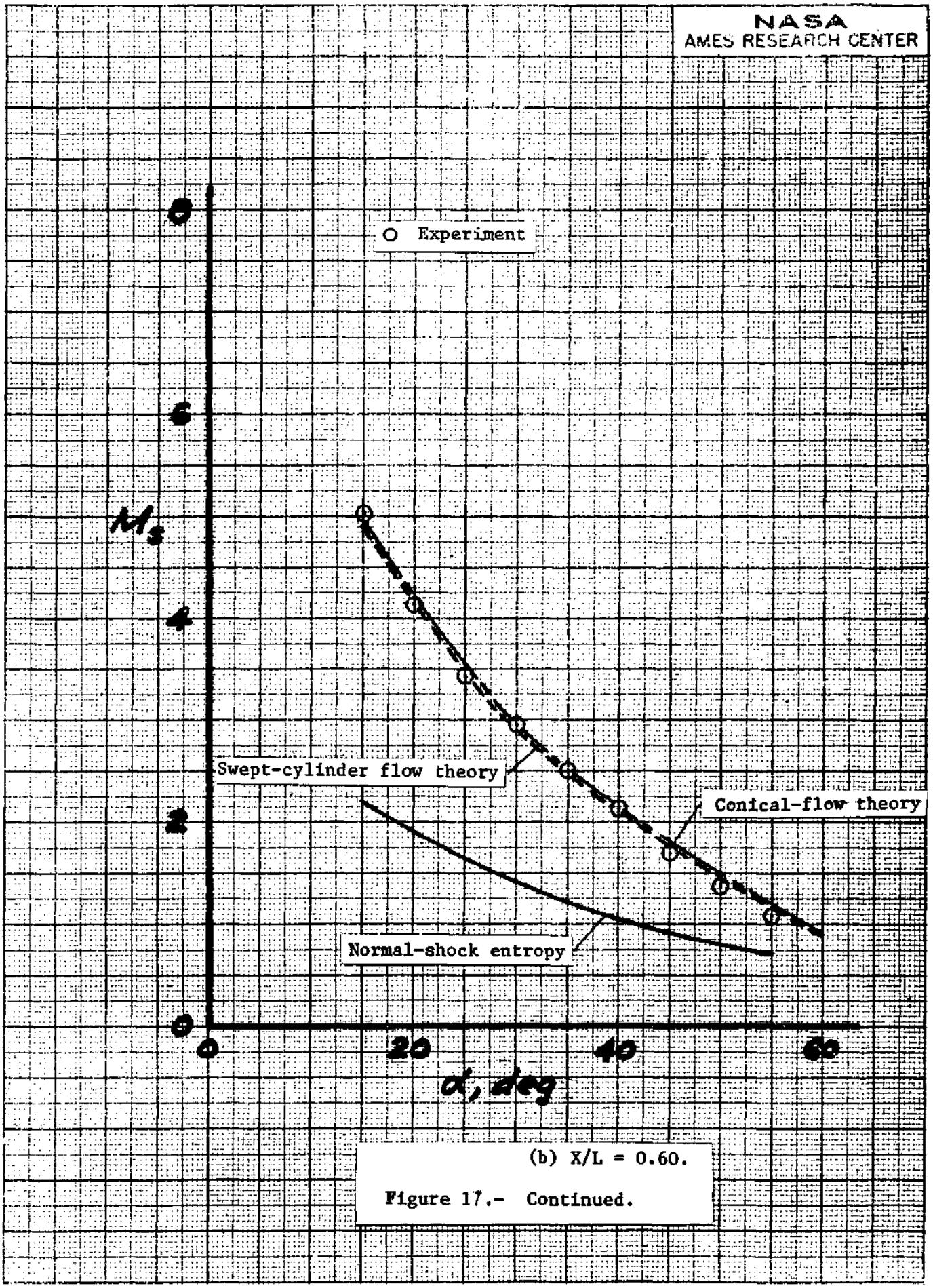

(b) X/L = 0.60.

Figure 17.- Continued.

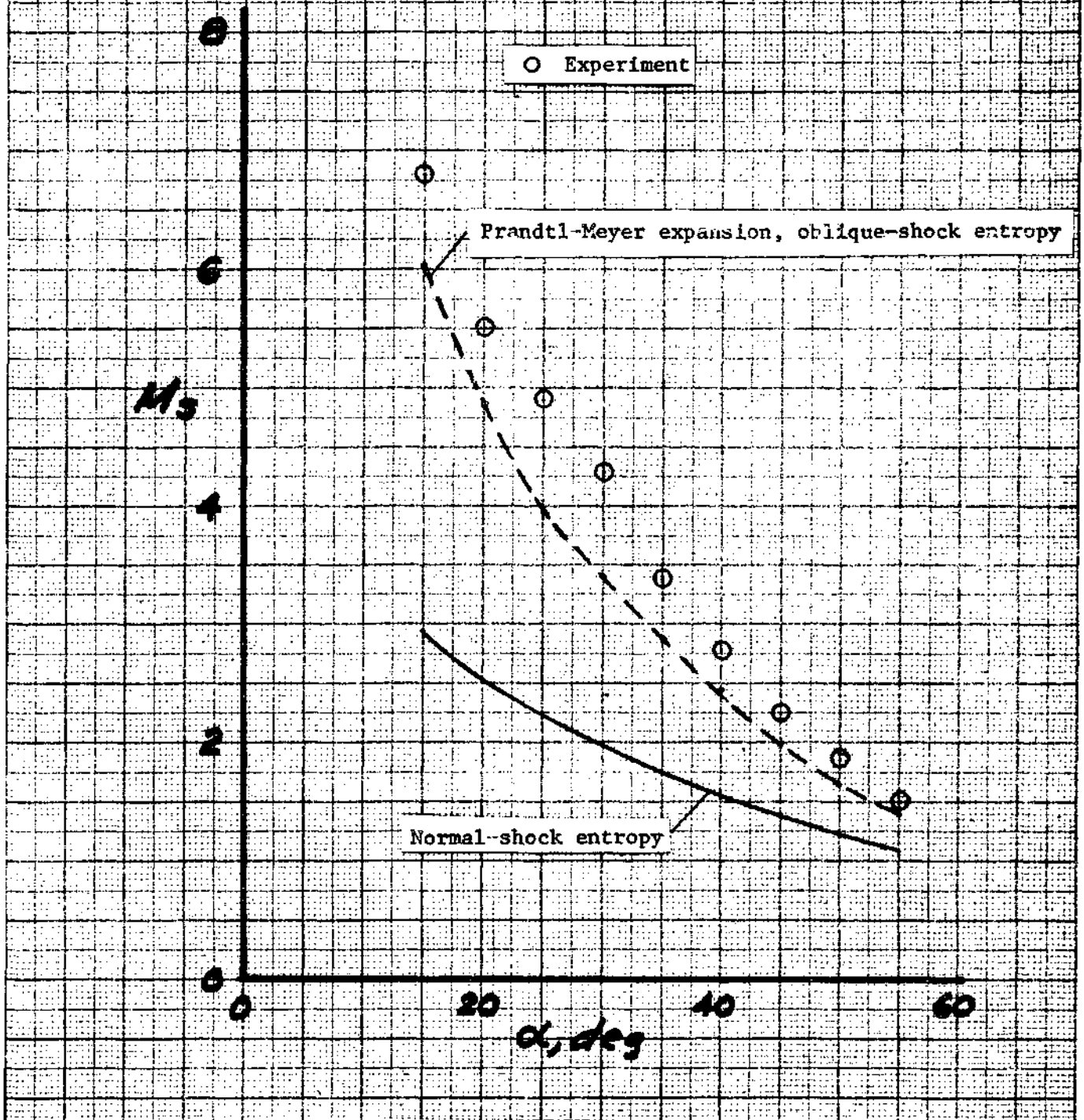

(c) X/L - 0.98.

Figure 17.- Concluded.

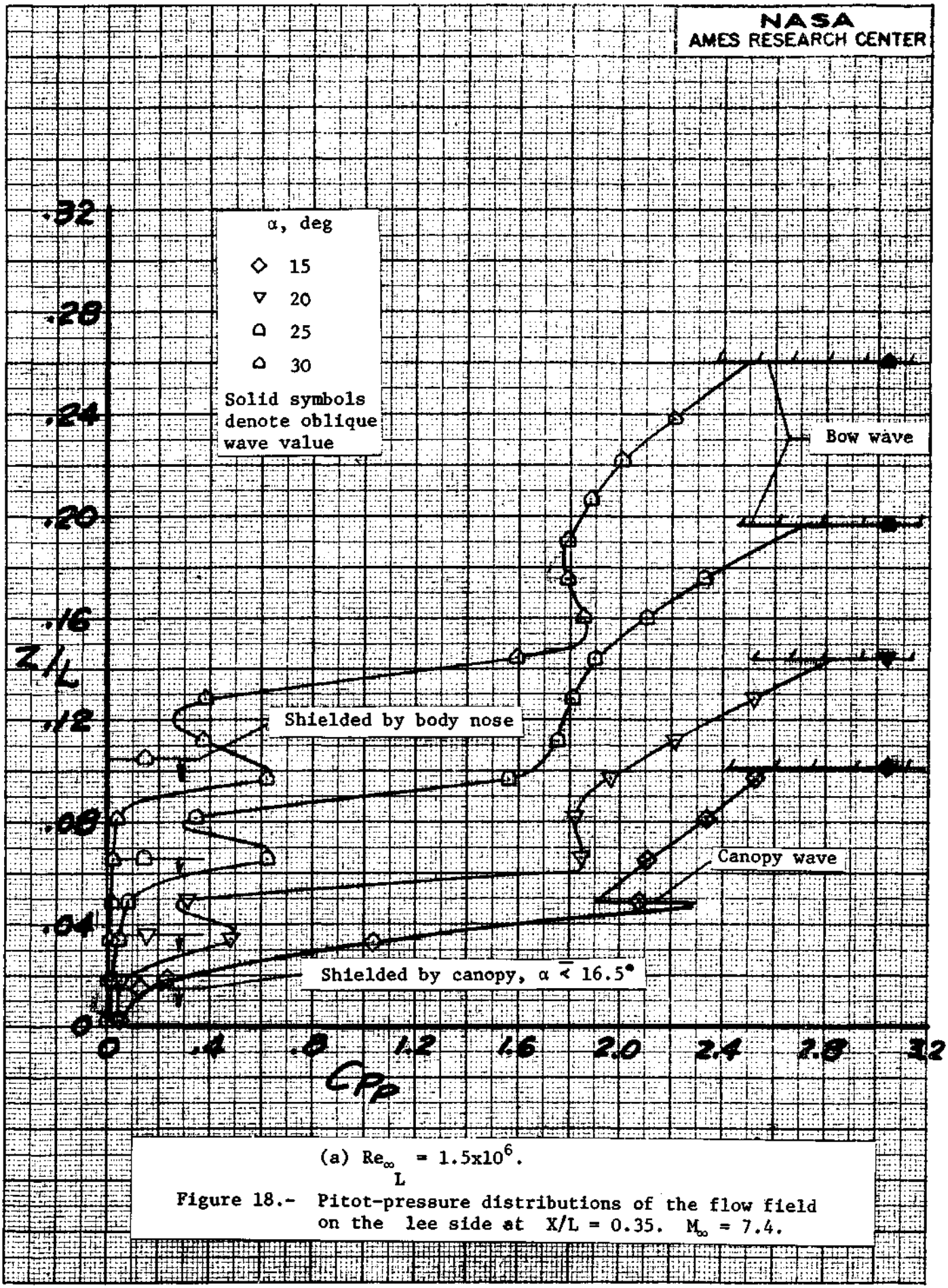

(a) $Re_{\infty_L} = 1.5 \times 10^6$.

Figure 18.- Pitot-pressure distributions of the flow field on the lee side at X/L = 0.35. $M_\infty = 7.4$.

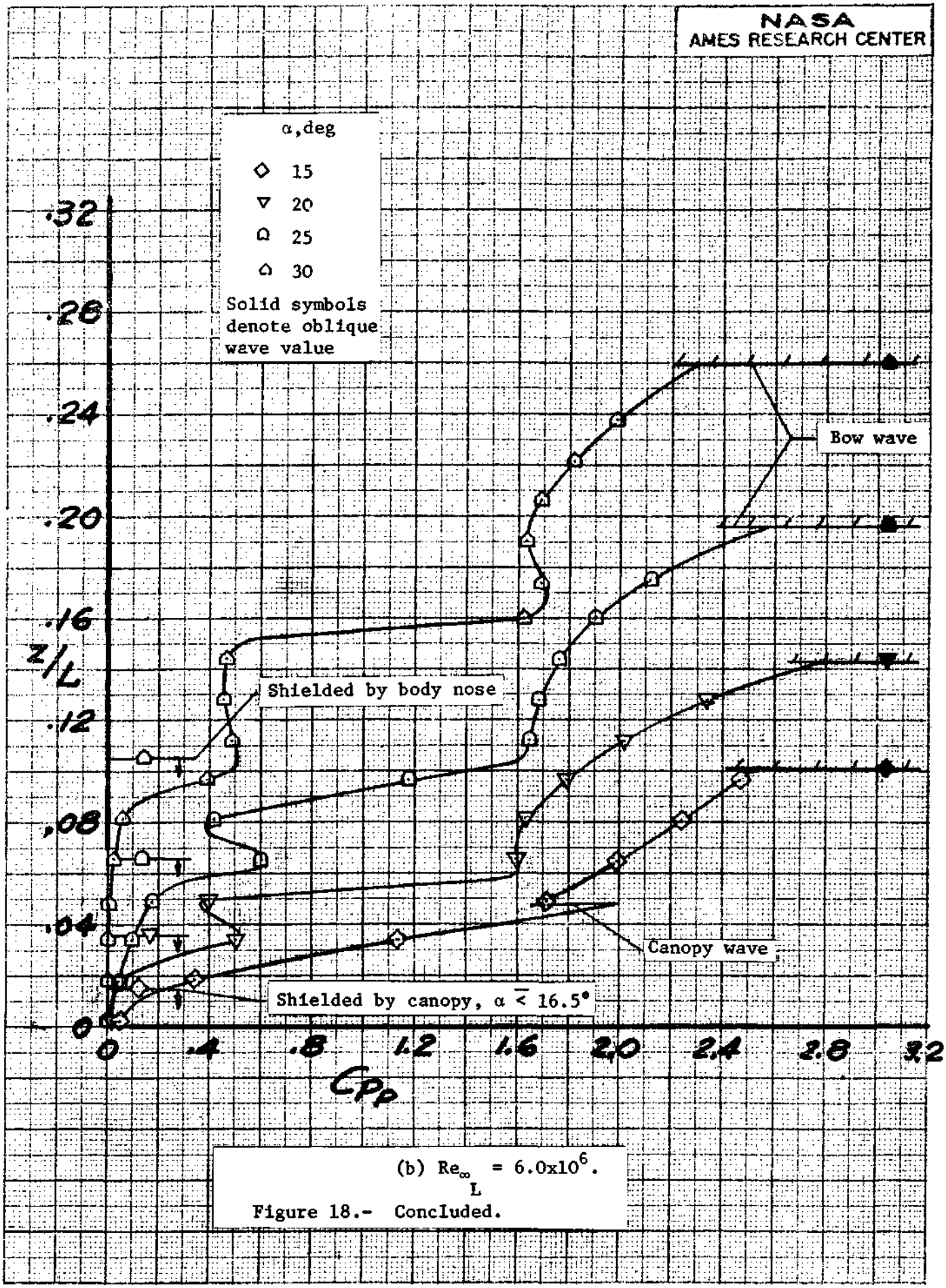

(b) $Re_{\infty_L} = 6.0 \times 10^6$.

Figure 18.- Concluded.

C.2

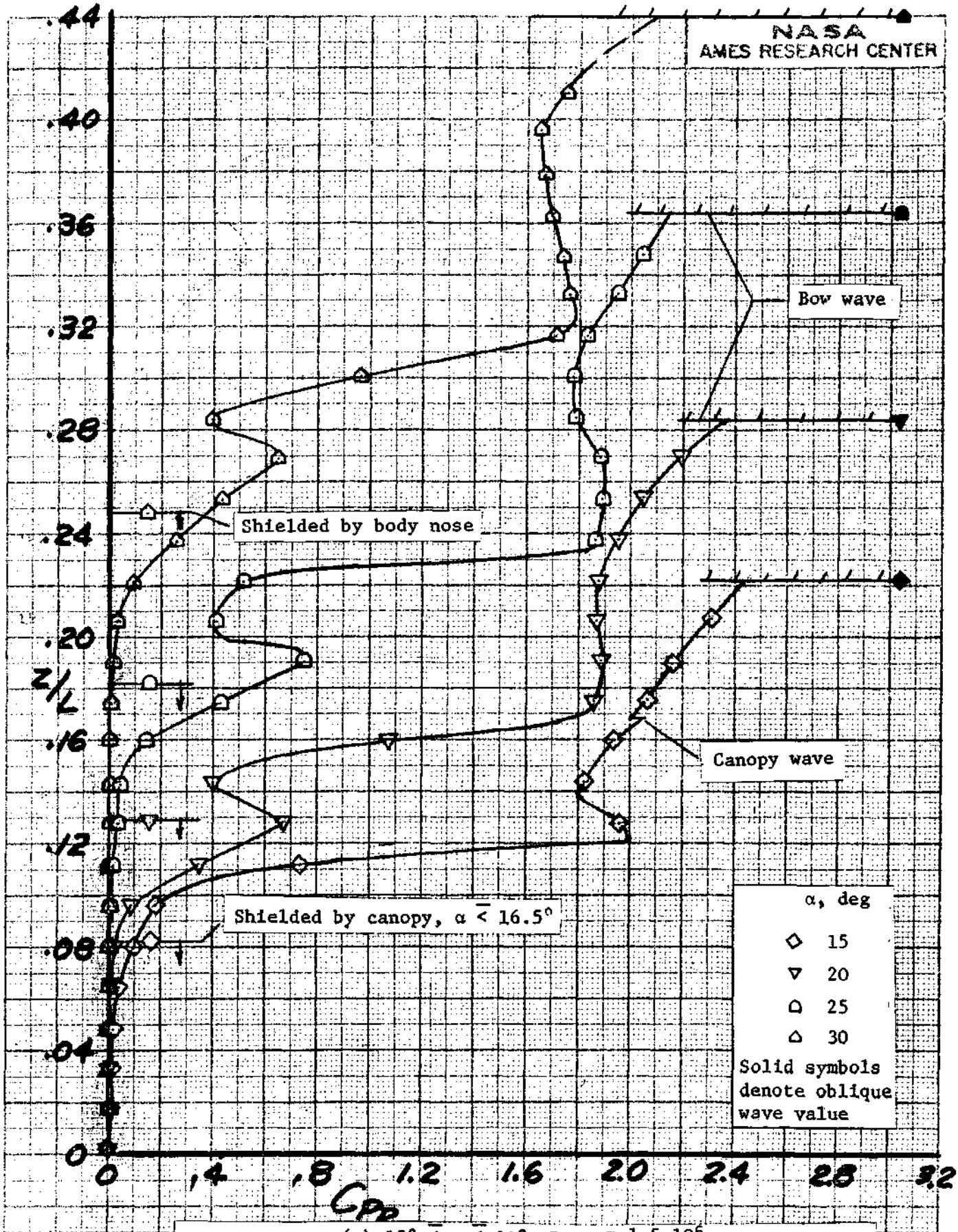

(a) $15° \leq \alpha \leq 30°$, $Re_{\infty_L} = 1.5 \times 10^6$.

Figure 19.- Pitot-pressure distributions of the flow field on the lee side at X/L = 0.60. $M_\infty = 7.4$

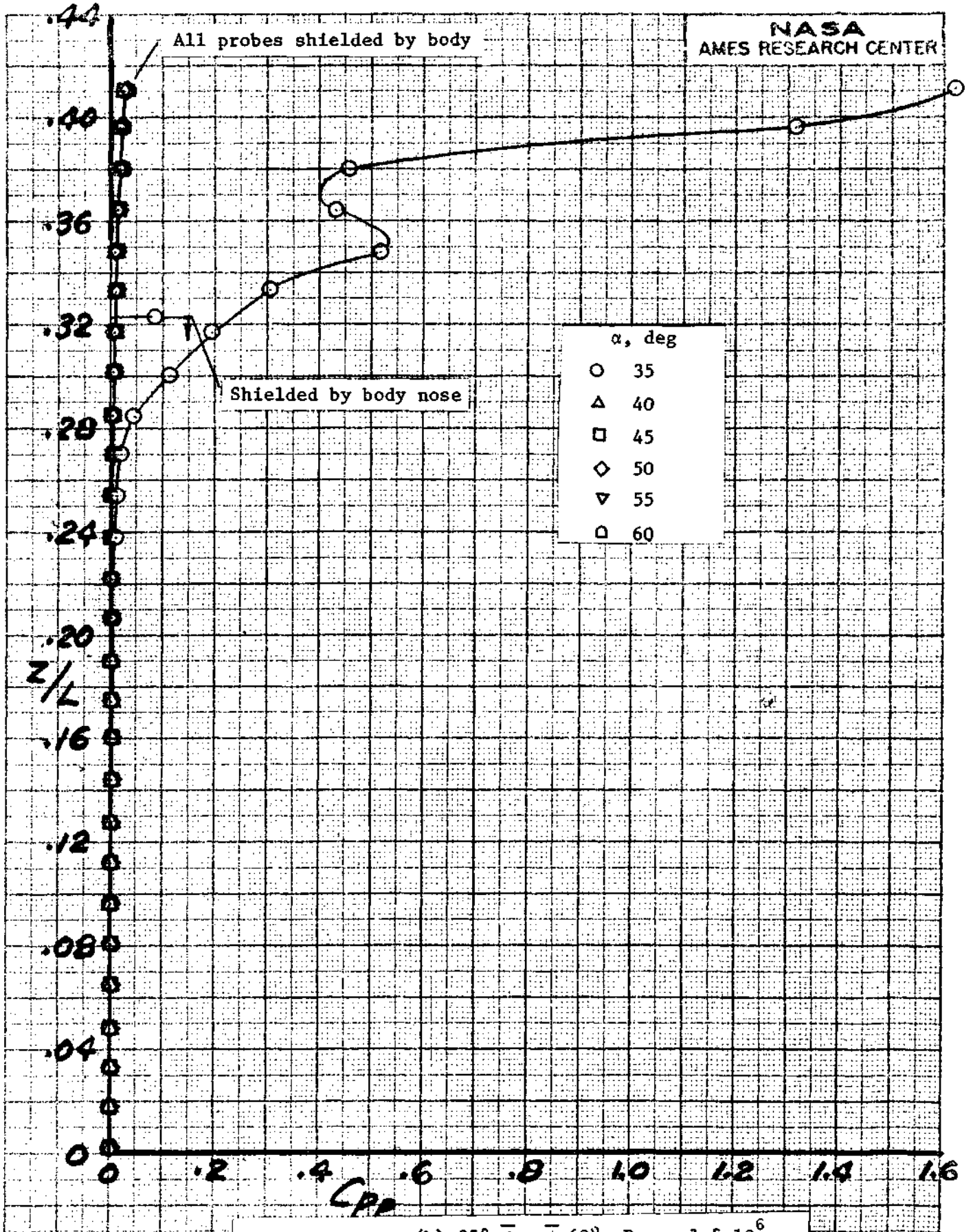

(b) $35° \leq \alpha \leq 60°$, $Re_{\infty_L} = 1.5 \times 10^6$.

Figure 19.- Concluded.

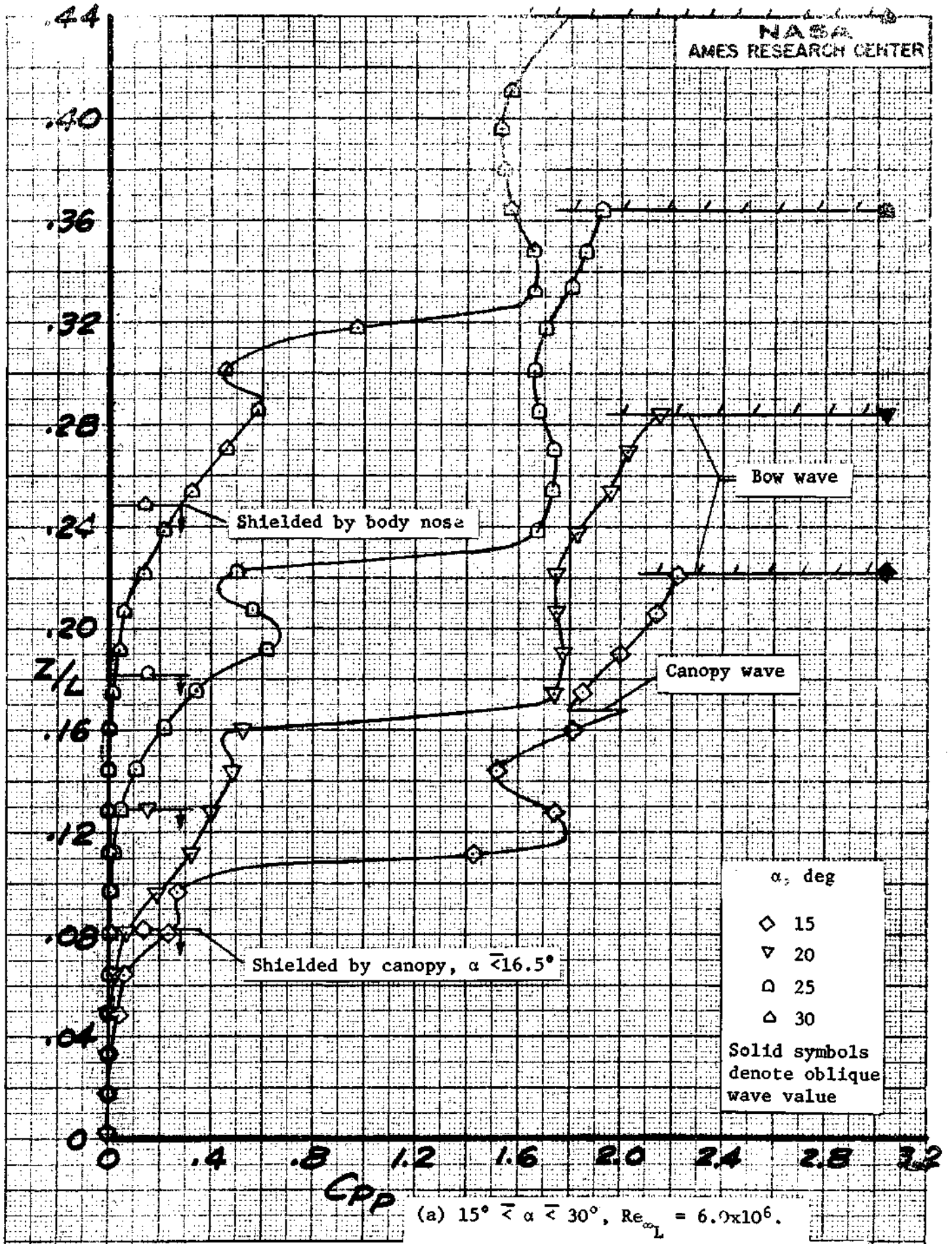

(a) $15° \leq \alpha \leq 30°$, $Re_{\infty_L} = 6.0 \times 10^6$.

Figure 20.- Pitot-pressure distributions of the flow field on the lee side at X/L = 0.60. $M_\infty = 7.4$.

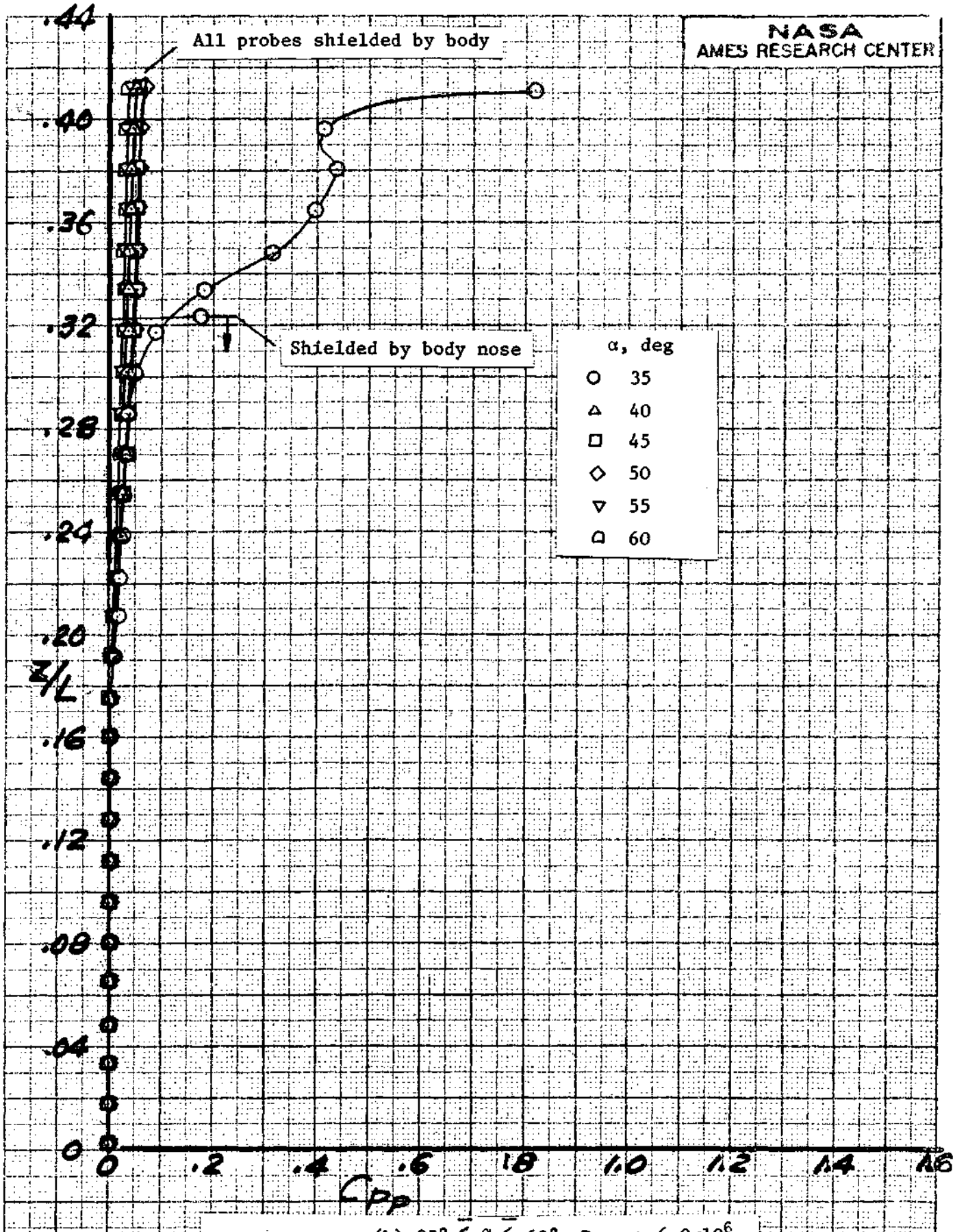

(b) $35° \leq \alpha \leq 60°$, $Re_{\infty_L} = 6.0 \times 10^6$.

Figure 20.- Concluded.

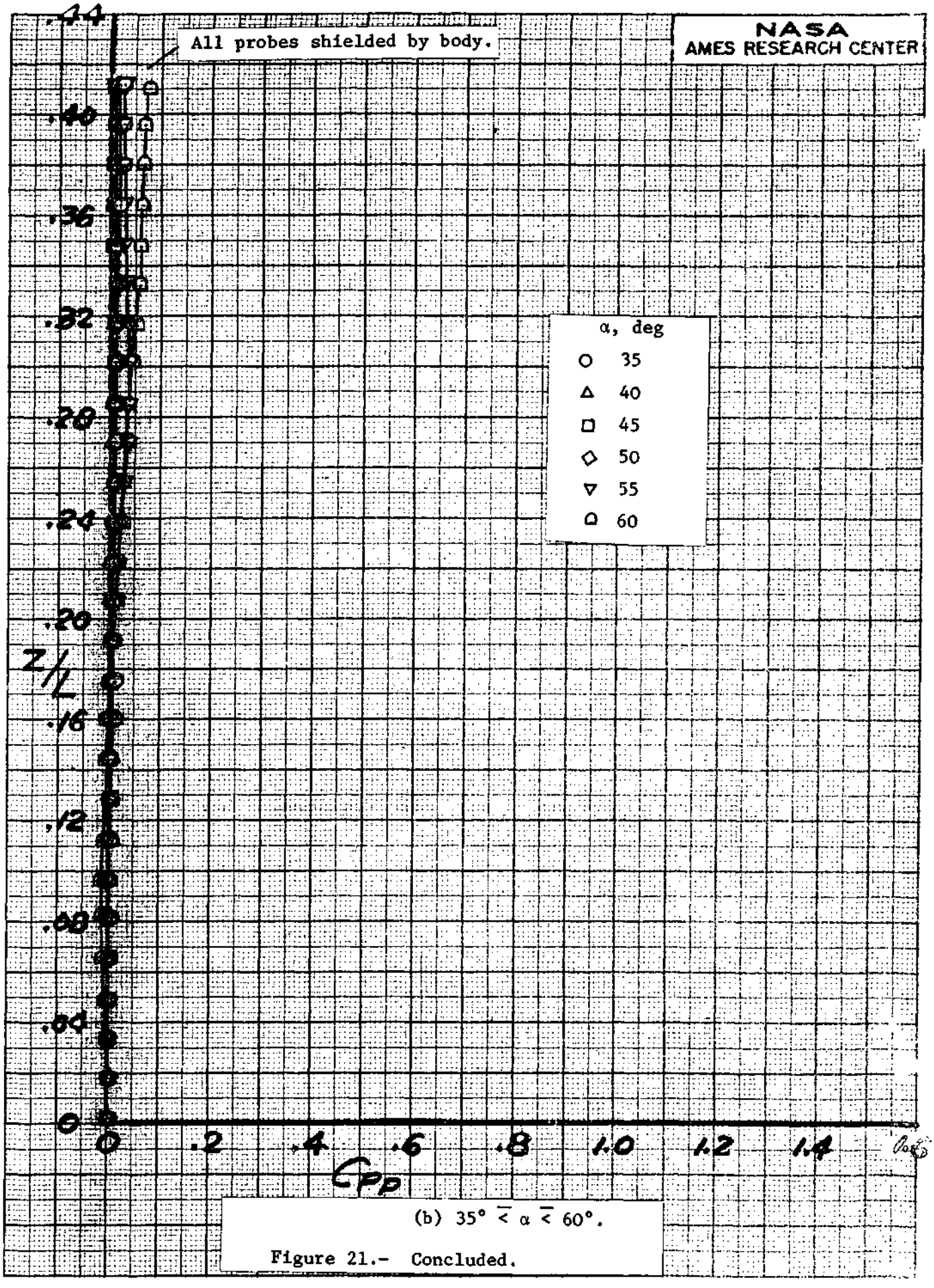

(b) $35° \leq \alpha \leq 60°$.

Figure 21.- Concluded.

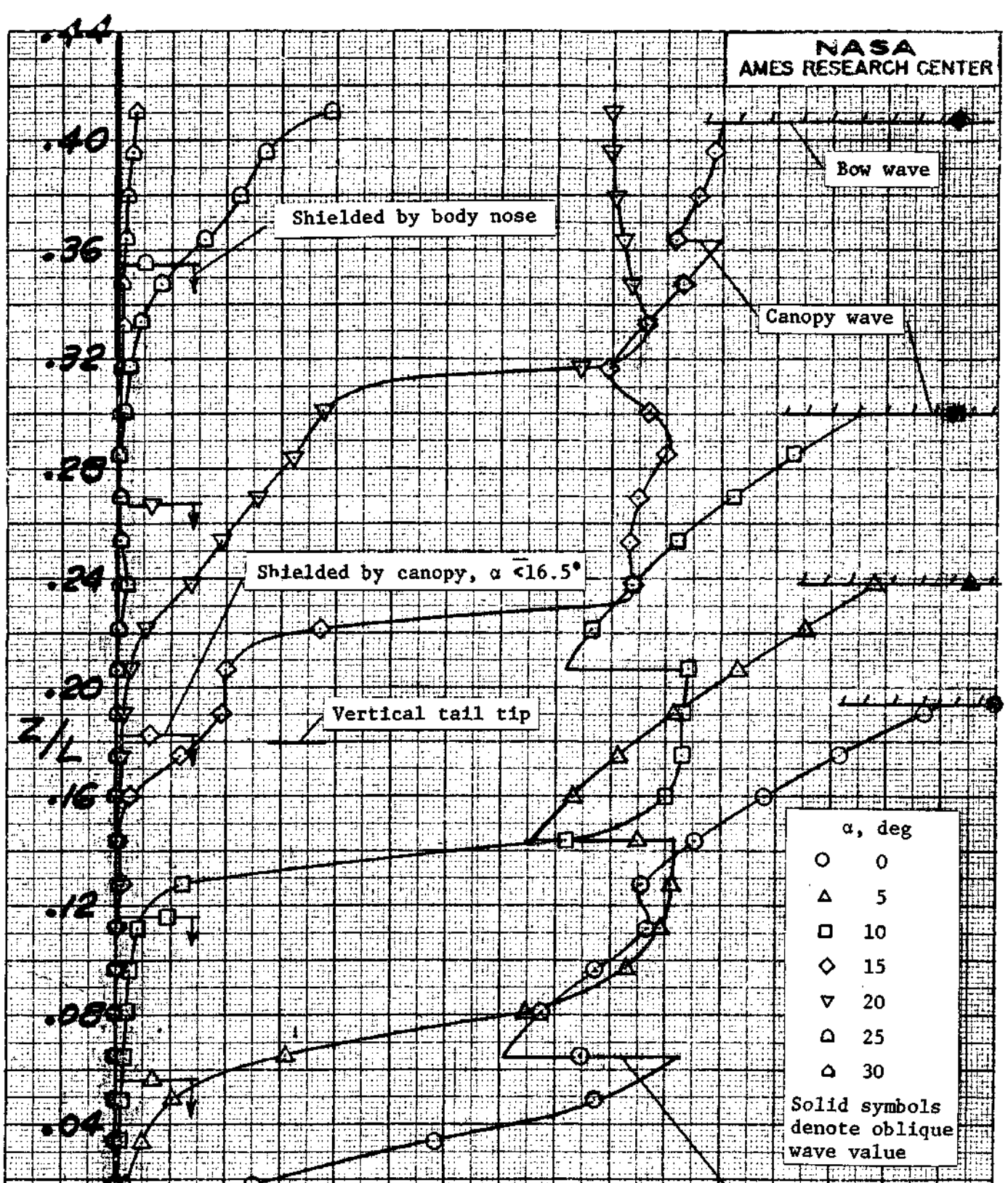

Figure 21.- Pitot-pressure distributions of the flow field on the lee side at X/L = 0.98. M_∞ = 7.4, Re_{∞_L} = 1.5x10^6.

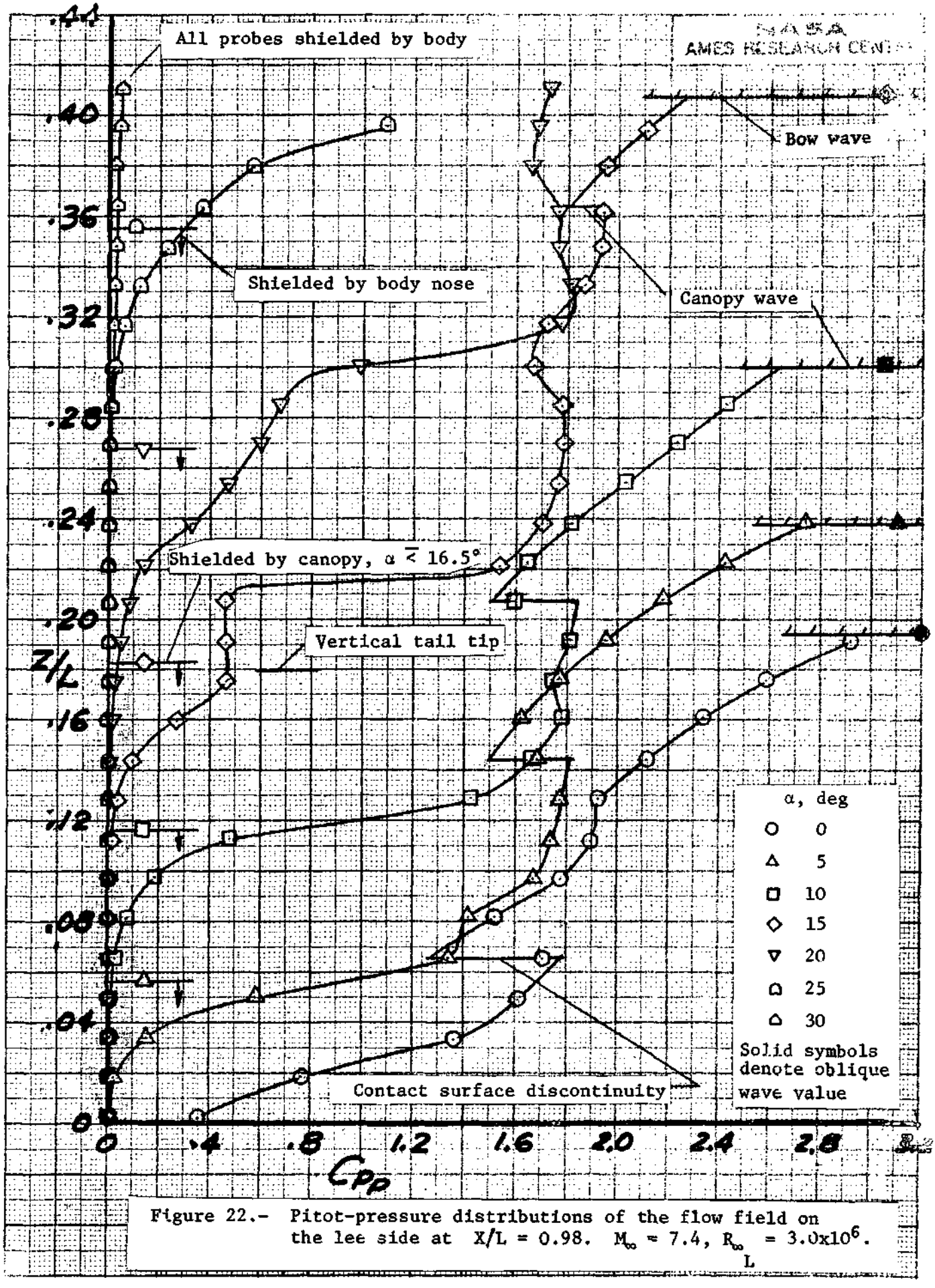

Figure 22.- Pitot-pressure distributions of the flow field on the lee side at X/L = 0.98. $M_\infty = 7.4$, $R_{\infty_L} = 3.0 \times 10^6$.

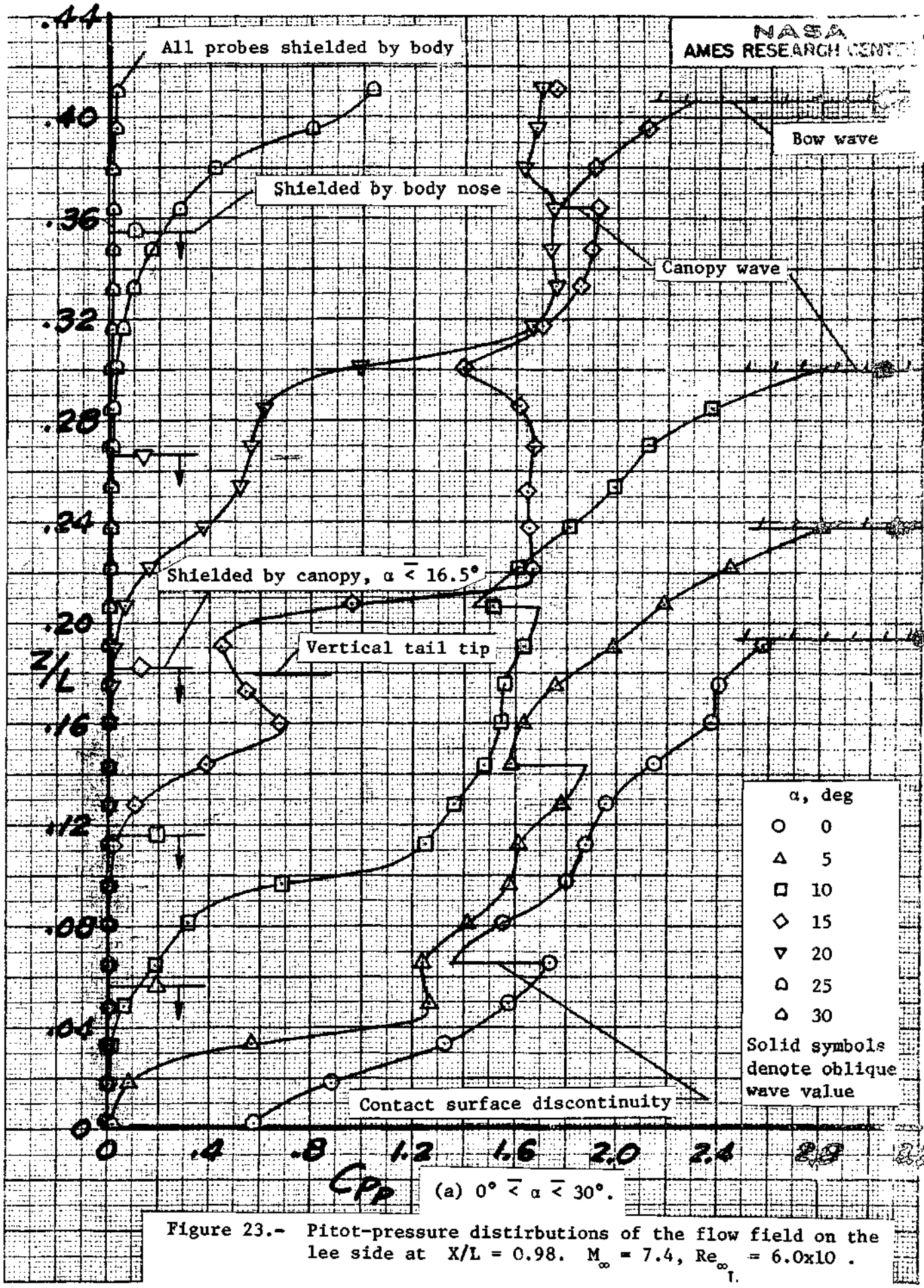

(a) $0° \leq \alpha \leq 30°$.

Figure 23.- Pitot-pressure distirbutions of the flow field on the lee side at X/L = 0.98. M_∞ = 7.4, Re_{∞_T} = 6.0x10 .

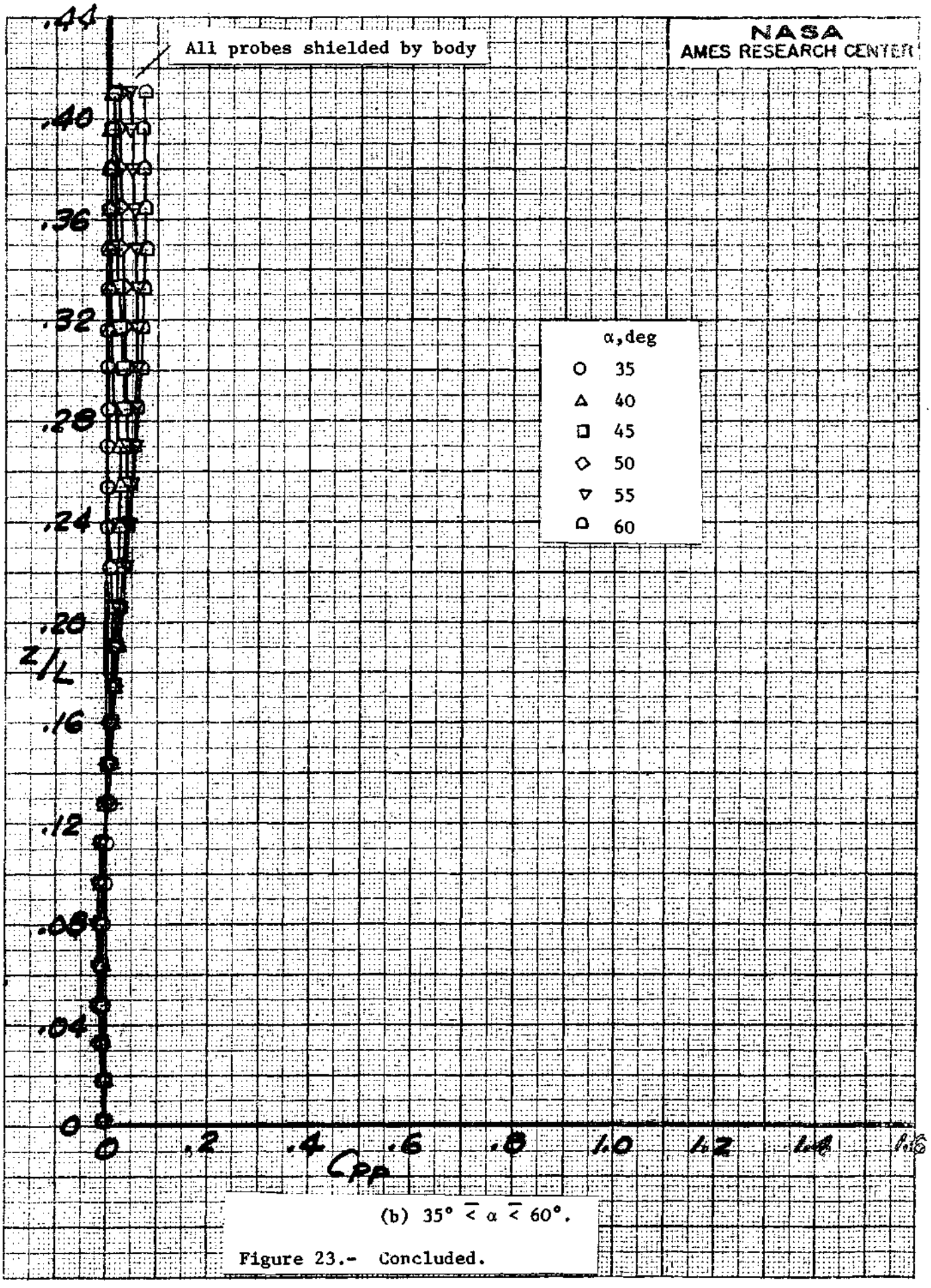

(b) $35° \leq \alpha \leq 60°$.

Figure 23.- Concluded.

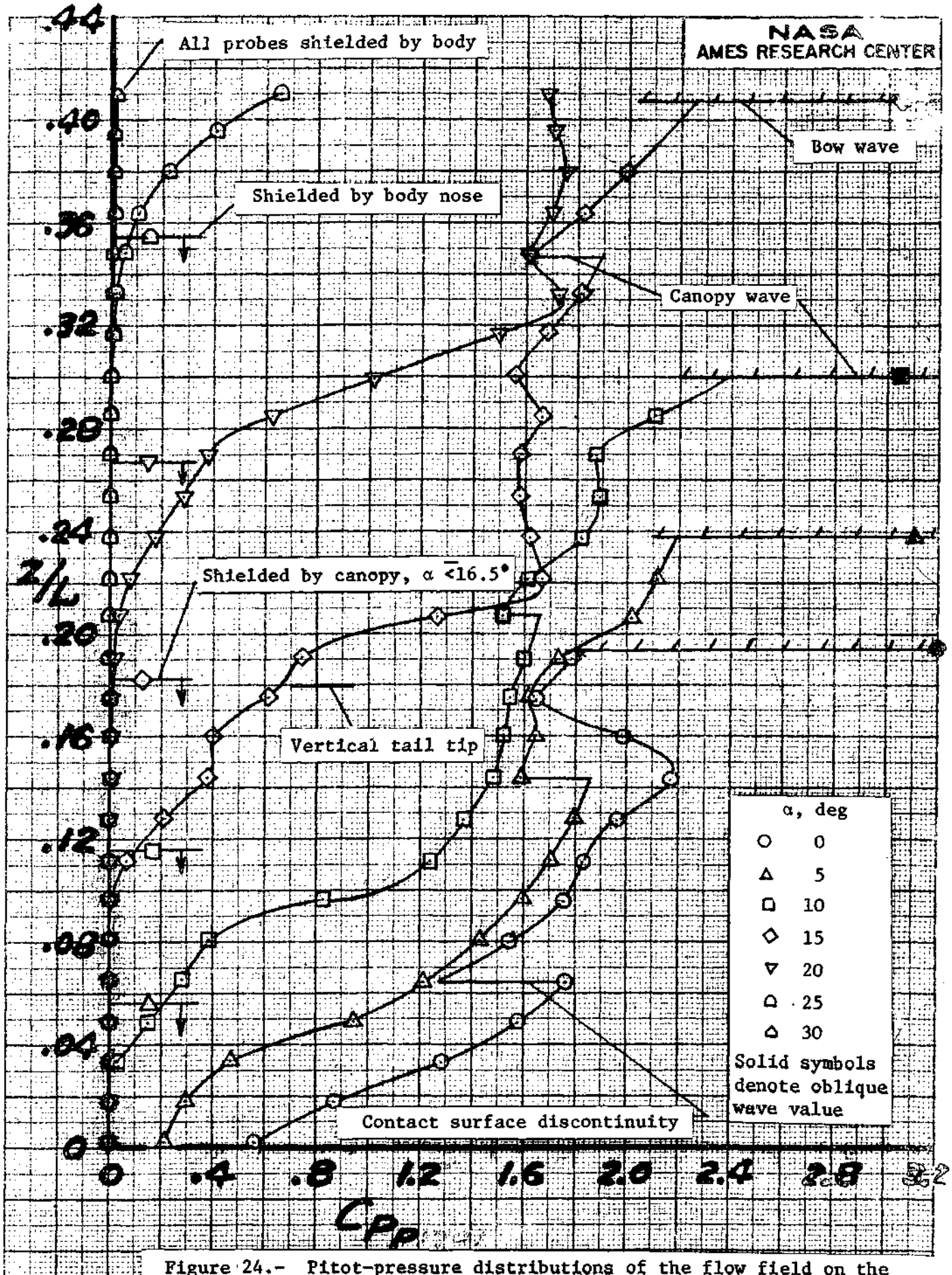

Figure 24.- Pitot-pressure distributions of the flow field on the lee side at $X/L = 0.98$. $M_\infty = 7.4$, $Re_{\infty_L} = 9.0 \times 10^6$.

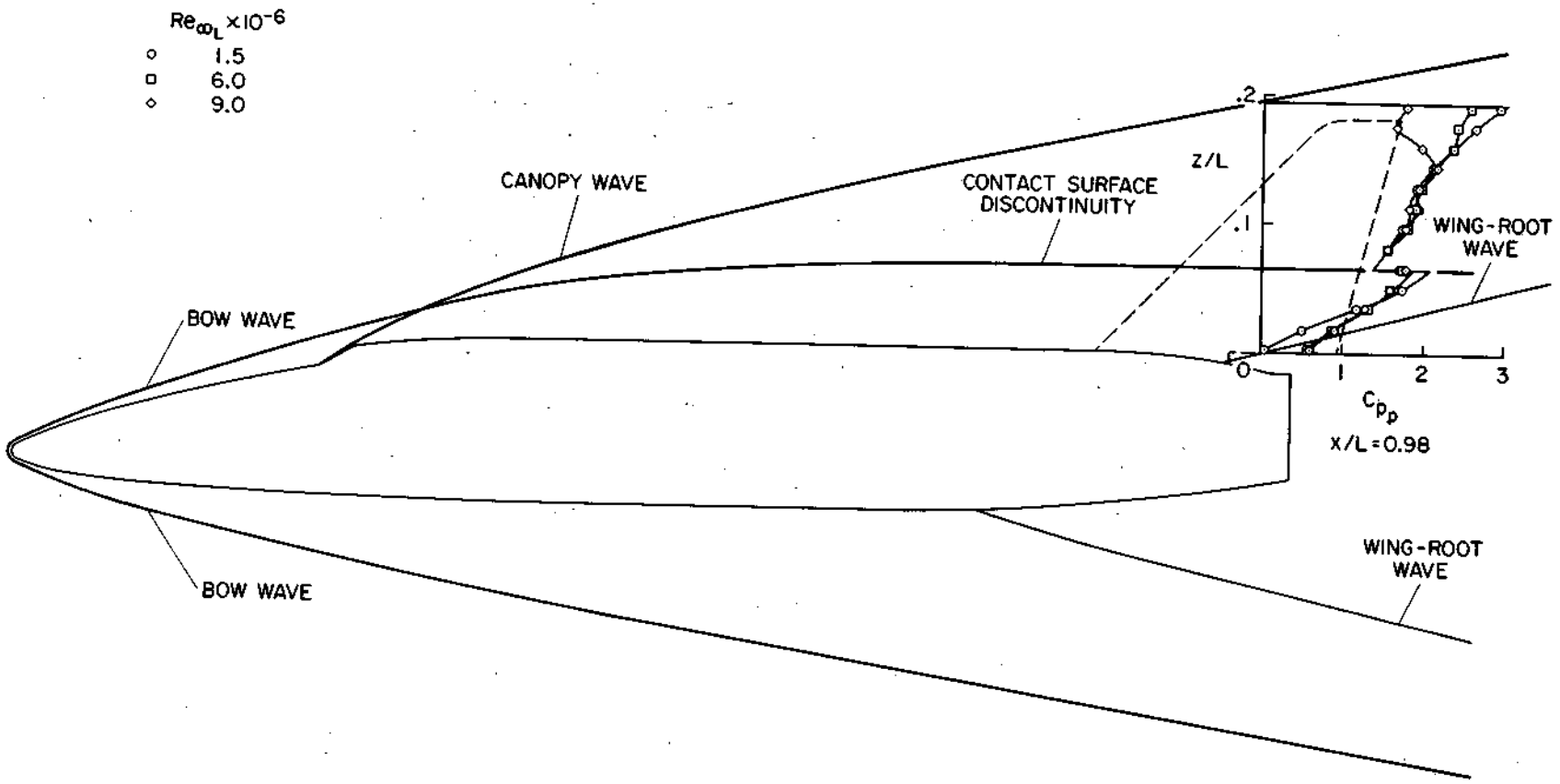

(a) $\alpha = 0°$.

Figure 25.- Composite of the shock-wave pattern and pitot-pressure distribution of the lee side flow field. $M_\infty = 7.4$.

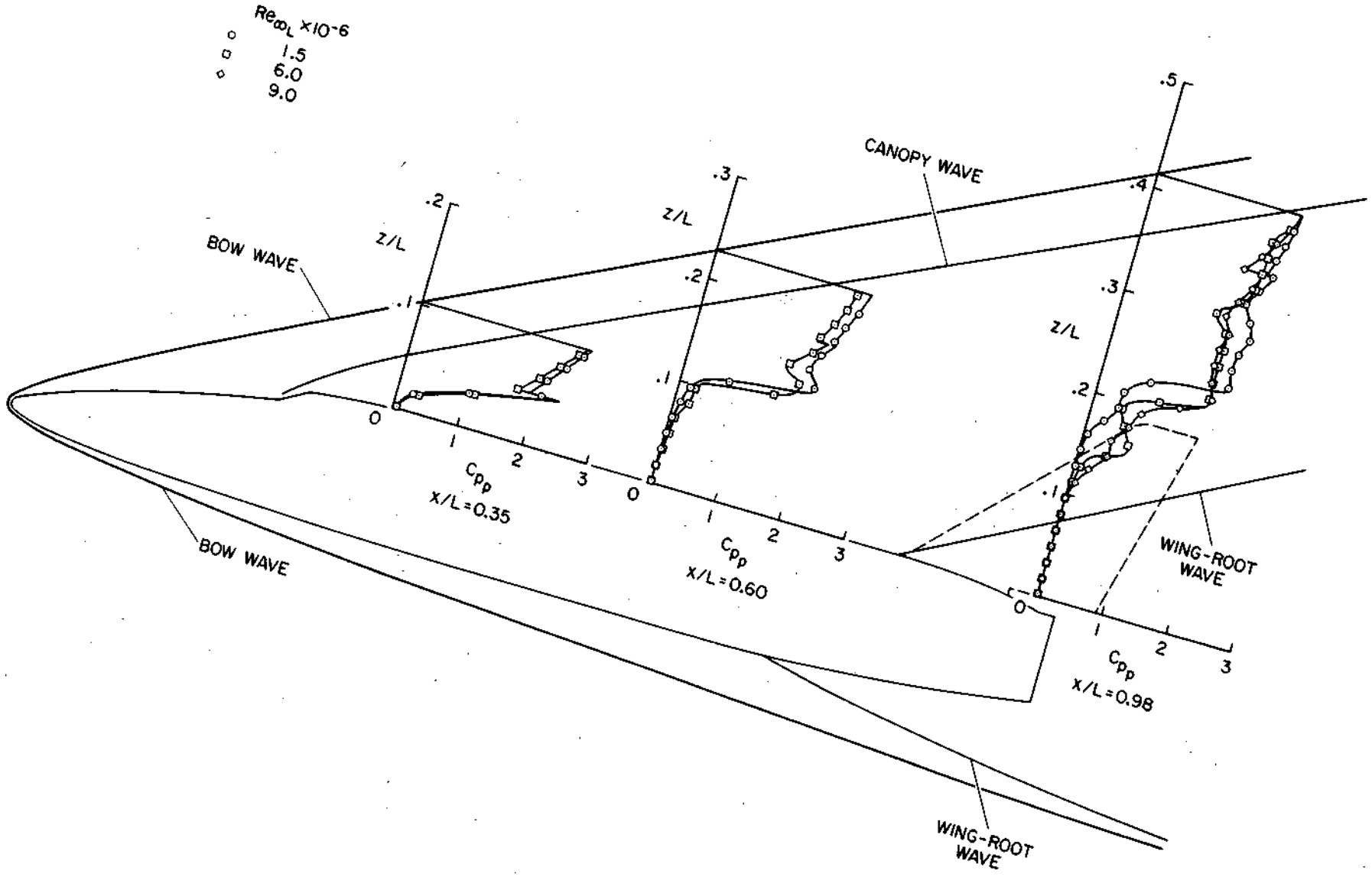

(b) $\alpha = 15°$.

Figure 25.- Continued.

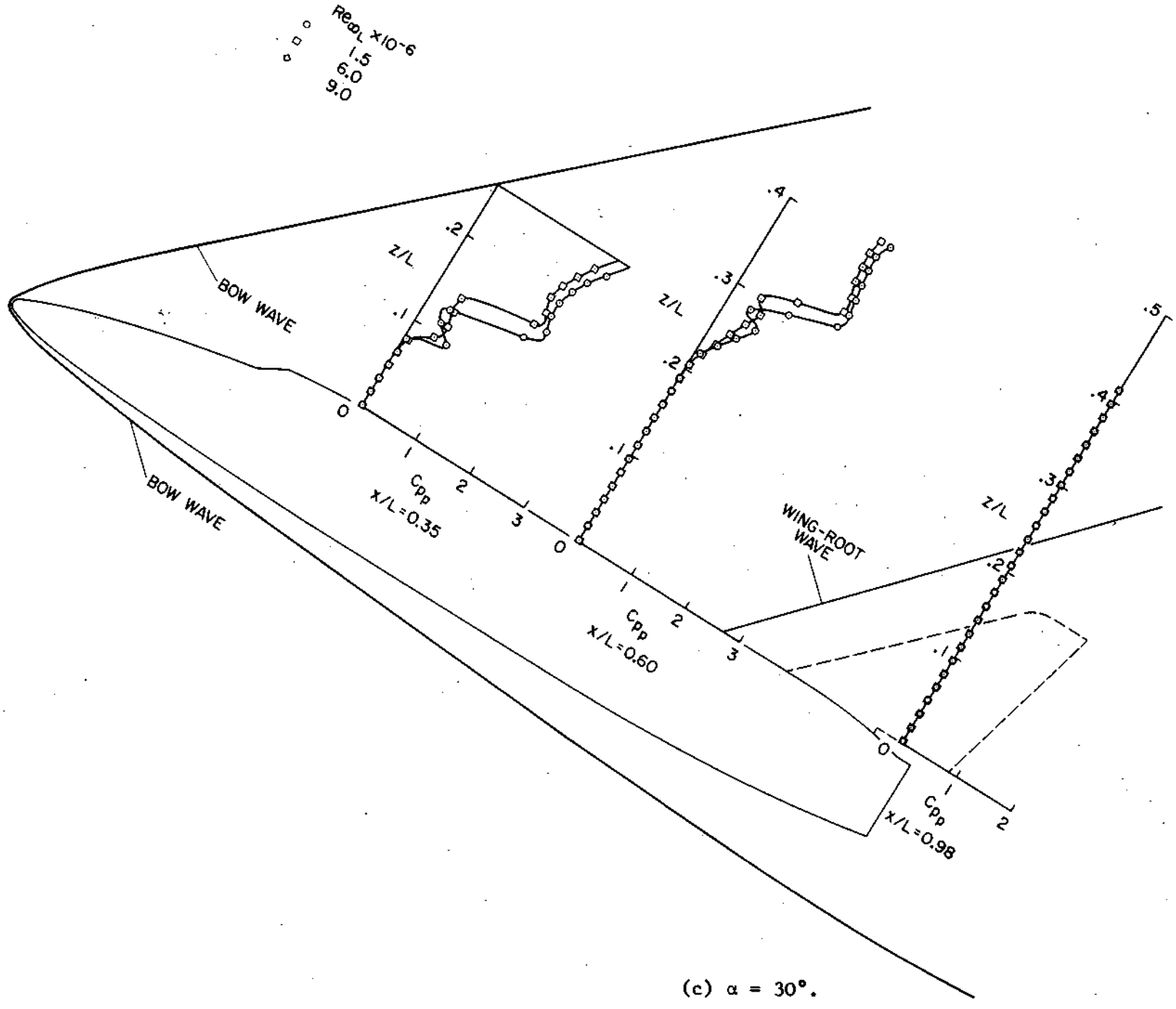

(c) $\alpha = 30°$.

Figure 25.- Continued.

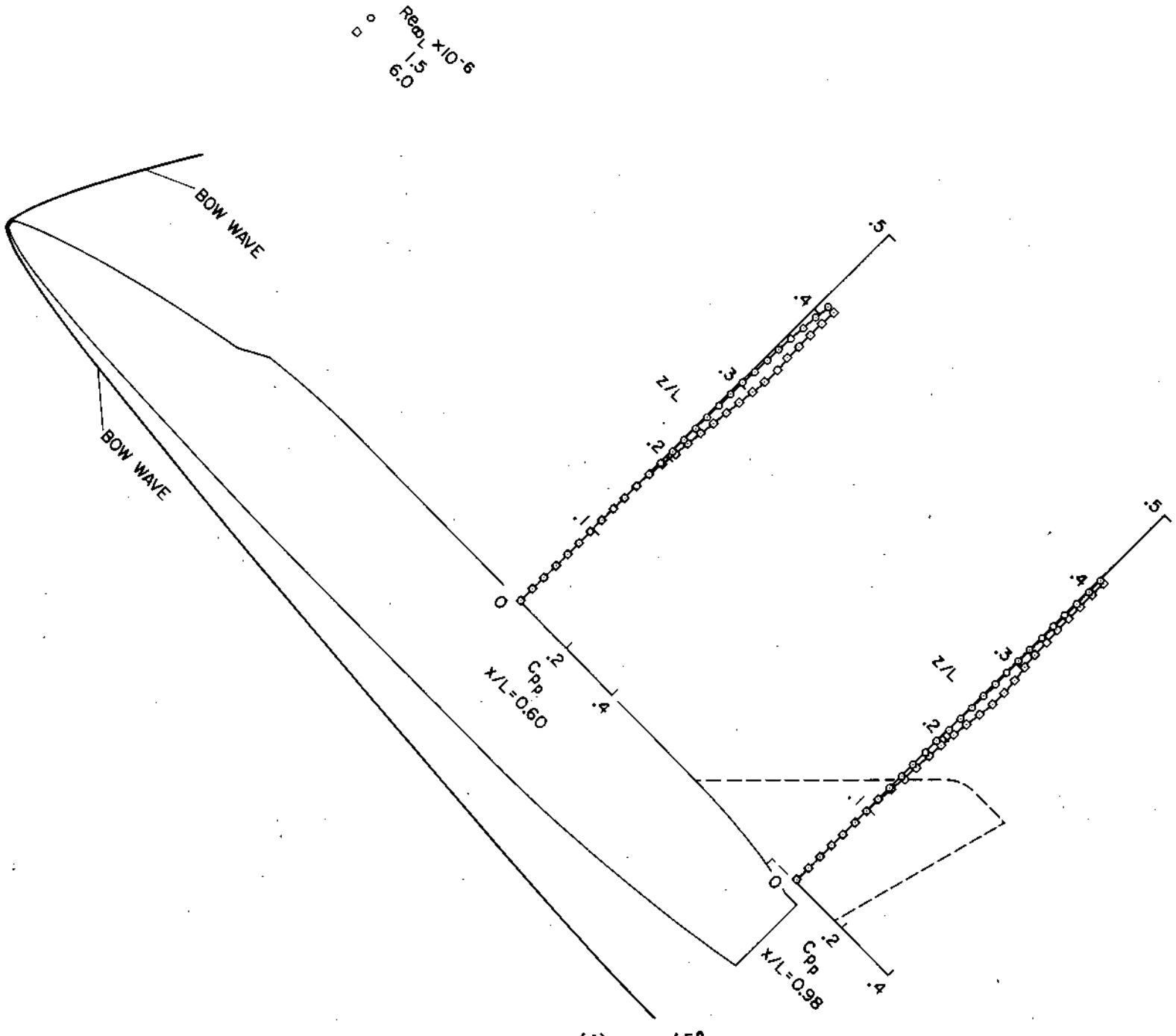

(d) $\alpha = 45°$.

Figure 25.- Continued.

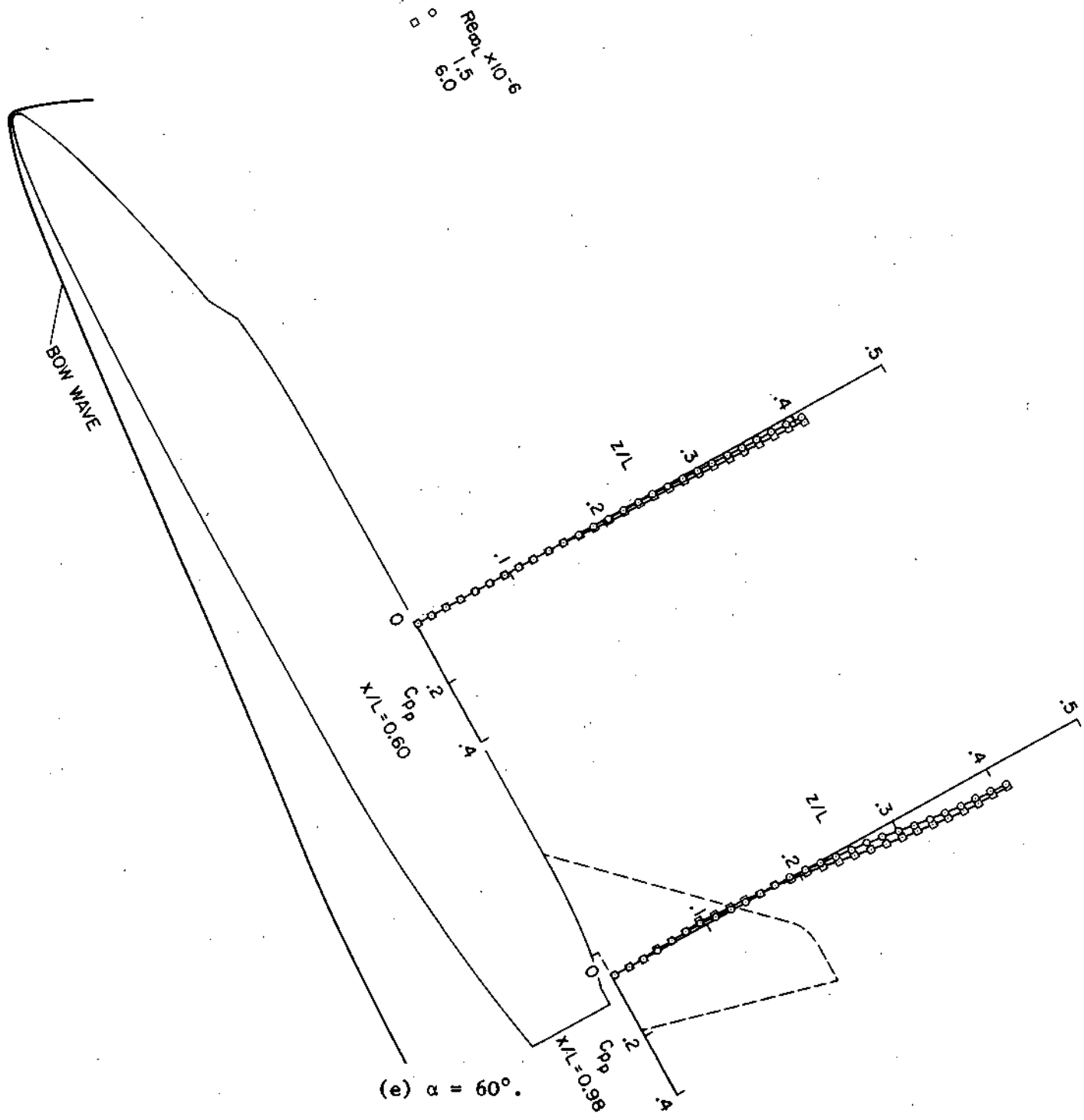

(e) $\alpha = 60°$.

Figure 25.- Concluded.